Technische Universität München
TUM School of Natural Sciences

Simplifying the Analysis of Ultrafast Dynamics by Polarization Control

Yi Xu

Vollständiger Abdruck der von der TUM School of Natural Sciences der Technischen Universität München zur Erlangung einer

Doktorin der Naturwissenschaften (Dr. rer. nat.)

genehmigten Dissertation.

Vorsitz: Prof. Dr. Christopher Stein

Prüfende der Dissertation:

1. Prof. Dr. Jürgen Hauer
2. Dr. Aras Kartouzian

Die Dissertation wurde am 06.06.2024 bei der Technischen Universität München eingereicht und durch die TUM School of Natural Sciences am 24.06.2024 angenommen

Collected Works

The following scientific work was conducted from February 2020 until May 2024 at the Technical University of Munich.

Xu, Y., Martin, T. P., Jänchen, M., Foja, R., Storch, G., Thyrhaug, E., de Vivie-Riedle, R., and Hauer, J., Determining Excited-State Absorption Properties of a Quinoid Flavin by Polarization-Resolved Transient Spectroscopy[J]. *J. Phys. Chem. A*, **2024**, 128, 19, 3830–3839

Xu, Y.; Mewes, L.; Thyrhaug, E.; Sláma, V.; Šanda, F.; Langhals, H.; Hauer, J., Isolating pure donor and acceptor signals by polarization-controlled transient absorption spectroscopy[J]. *J. Phys. Chem. Lett*. 2023, 14, 5390-5396.

Xu, Y.; Mewes, L.; Thyrhaug, E.; Langhals, H.; Hauer, J. In *Decomposing Transient Absorption Signals into Donor and Acceptor Contributions by Polarization Control*, International Conference on Ultrafast Phenomena, Optica Publishing Group: 2022; p Tu4A. 5.

Contributions to conferences and workshops

Poster (first-author): Understanding the catalytic activity of reduced flavin, *the first Conference on Light-induced Transformations (LIT),* Germany, 2023

Talk: Understanding the catalytic activity of reduced flavin, *5th Seminar Day of DFG-funded Collaborative Research Centre (CRC) 325,* Leising/Beilngries (Oberbayern), 2023

Talk: Simplifying the Analysis of Transient Absorption Data by Polarization Control, *DPG Spring Meeting,* Hannover, 2023

Poster (first-author): Decomposing transient absorption signals into donor and acceptor contributions by polarization control, *International Conference on Ultrafast Phenomena 2022,* Montreal, 2022

Talk: Decomposing transient absorption signals into donor and acceptor contributions by polarization control, *2nd Seminar Day of DFG-funded Collaborative Research Centre (CRC) 325,* Regensburg, 2022

Poster (first-author): Decomposing transient absorption signals into donor and acceptor contributions by polarization control, *Program of the 1st Annual Retreat DFG-funded Collaborative Research Centre (CRC) 325,* Raitenhaslach/Burghausen, 2022

Preface

This publication-based thesis focuses on the following scientific works:

- Xu, Y.; Mewes, L.; Thyrhaug, E.; Sláma, V.; Šanda, F. e.; Langhals, H.; Hauer, J., Isolating pure donor and acceptor signals by polarization-controlled transient absorption spectroscopy[J]. *J. Phys. Chem. Lett.* **2023**, *14*, 5390-5396.

- Xu, Y., Martin, T. P., Jänchen, M., Foja, R., Storch, G., Thyrhaug, E., de Vivie-Riedle, R., and Hauer, J., Determining Excited-State Absorption Properties of a Quinoid Flavin by Polarization-Resolved Transient Spectroscopy[J]. *J. Phys. Chem. A*, **2024**, 128, 19, 3830–3839

Acknowledgment

I want to express my immense gratitude to everyone who supported me during the completion of my thesis. Firstly, I would like to thank my supervisor, Prof. Dr. Jürgen Hauer, for offering me the opportunity to be part of the Dynamic Spectroscopy family. Throughout my Ph.D. journey, his expertise, patience, and encouragement shaped my research path and elevated the standard of my work.

I would also like to thank Dr. Erling Thyrhaug for his invaluable guidance, unwavering support, and insightful feedback, which significantly contributed to the completion of this thesis. Dr. Lars Mewes' assistance in setting up experiments, data analysis, and paper writing has profoundly impacted my understanding of optics and transformed me into a proficient researcher.

I want to thank Dr. Aras Kartouzian for generously devoting his time to serve as the second supervisor of my thesis.

Furthermore, I would like to express my gratitude to all the collaborators involved, including Prof. Eberhard Riedle, Dr. Ferdinand Bergmeier, Prof. Regina de Vivie-Riedle, Prof. František Šanda, Dr. Martin Peschel, Dr. Vladislav Sláma, Prof. Heinz Langhals, Dr. Golo Storch, and Richard Foja, for their contributions and support in various aspects of my study.

Special thanks go to my fellow Ph.D. students and colleagues, Ajeet, Yang, Erika, Max, Hongxing, Miriam, Alina, and Kiran, and former colleagues Pavel, Constantin, Václav, and Pushpendra, whose assistance in the laboratory and positive work environment have been invaluable. Thank you for letting me enjoy the relaxing surroundings in our group.

I would also like to extend my gratitude to Sabine K., Sabine F., Peter, Anette, and Mathias for their ongoing support and assistance. My gratitude also extends to the funding sources, IMPRS-APS, CRC325, and e-conversion, for their financial support.

Also, I’d like to thank my former supervisor, Prof. Rui-Min Han at Renmin University of China, who gave me basic scientific training and brought me more confidence and an optimistic attitude towards life.

Lastly, I would like to express my deepest appreciation to my family and friends for their unwavering support and encouragement throughout this journey. Thanks to my mother, who has been a single parent for over twenty years, and my grandma who unconditionally nurtured me. Thanks to my uncles, aunts, cousins, and my father, who passed away 16 years ago and would have been proud to see his daughter earn a Ph.D.

Abstract

Understanding the intrinsic photophysical properties of molecular photocatalysts is crucial for advancing their efficiency. Important parameters are, amongst others, the lifetimes of excited states and the energy transfer pathways between intermediate states. Transient absorption spectroscopy (TAS) is a powerful technique to study the dynamics of photo-excited states in various systems. However, the optical spectra of molecules are often highly congested, inhibiting the definite assignment of features to excited state dynamics. This thesis shows how transient spectra can be disentangled by applying a polarization-based strategy. This approach greatly reduces spectral congestion in complex systems and provides information on the directions of transition dipole moments (TDMs). Furthermore, we project the TAS-data into orthogonal polarization-associated spectra (PAS). This allows for detailed electronic structure analysis and delivers pure donor and acceptor spectra in an orthogonal dyadic system. In this dyad, the TDMs for D and A are orthogonal by design yet show Förster-type excitation energy transfer. The analysis based on PAS contributes to the resolution of this problem by supporting the existence of significant geometric/dipole fluctuations in this ortho-dyad.

We also employed the PAS method to determine pure excited state absorption (ESA) signals in a quinoid oxidized flavin sample. By comparing to more conventional methods of extracting pure ESA signals, we highlight the advantages of our approach, allowing the determination of the relative angle between the TDMs of two neighboring ESA transitions. We highlight the influence of vibronic coupling, which would have remained hidden in conventional TAS.

Kurzfassung

Um die Effizienz molekularer Photokatalysatoren zu verbessern, ist es wesentlich, deren intrinsische photophysikalischen Eigenschaften zu verstehen. Wichtige Parameter sind dabei u.A. die Lebensdauern angeregter Zustände und die Mechanismen des Energietransfers zwischen Intermediaten. Transiente Absorptionsspektroskopie (TAS) ist besonders gut dafür geeignet, die Dynamiken photo-angeregter Zustände verschiedener Systeme zu untersuchen. Jedoch weisen die optischen Spektren von Molekülen oft überlappende Beiträge auf, die nicht immer eindeutig einem bestimmten Prozess im angeregten Zustand zugeordnet werden können. Diese Arbeit zeigt, wie die Interpretation transienter Spektren mithilfe einer polarisationsbasierten Methode vereinfacht werden kann. Besonders in komplexen Systemen reduziert dieser Ansatz die spektrale Überlagerung deutlich und bietet zusätzlich noch Informationen über die Richtungen der Übergangsdipolmomente (TDMs). Zudem projizieren wir die TAS-Daten auf orthogonale polarisationsassoziierte Spektren (PAS). Dieses Vorgehen erlaubt eine detaillierte Analyse der elektronischen Struktur eines orthogonalen dyadischen Systems und liefert reine Donor (D)- und Akzeptorspektren (A). Hier sind die TDMs zwischen D und A zwar orthogonal ausgerichtet, zeigen allerdings trotzdem eine Übertragung von Anregungsenergie nach dem Förster-Modell. Die Analyse basierend auf den PAS trägt zur Klärung dieses Sachverhalts bei, da es die Existenz signifikanter geometrischer/Dipolfluktuationen in diesem System unterstützt.

Zusätzlich wenden wir die PAS Methode an, um die reinen Signale der Absorption des angeregten Zustands (ESA) in einem quinoiden oxidierten Flavin zu isolieren. Ein Vergleich mit reinen ESA-Signalen, die über konventionelle Methoden erhalten wurden, zeigt die Vorteile unserer Methode. Dazu zählt u.A. die Bestimmung des relativen Winkels zwischen TDMs benachbarter ESA Übergänge. Außerdem betonen wir den Einfluss von vibronischer Kopplung, welche in konventioneller TAS unentdeckt geblieben wäre.

Abbreviations

TDM(s)	transition dipole moment(s)
IC	internal conversion
ISC	intersystem crossing
EET	excitation energy transfer
TA(S)	transient absorption (spectroscopy)
MA	magic angle
TAA	transient absorption anisotropy
D-A	donor-acceptor
LD	linear dichroism
FA	fluorescence anisotropy
PAS	polarization associated spectra
OD	optical density
GSB	ground-state bleach
SE	stimulated emission
ESA	excited state absorption
SHG	second harmonic generation
BBO	beta-barium borate crystal
FS	fused silica
NOPA	non-collinear parametric amplifier
4WM	four-wave-mixing

CONTENTS

1. INTRODUCTION

Solar energy is an abundant and eco-friendly resource available worldwide. In just an hour, the amount of solar power reaching the Earth's surface is greater than global energy consumption in a year.[1-2] Photocatalysis has gained significant attention for its proven potential in various energy and environmental applications, with the aim of transforming solar energy into chemical energy.[3-6] In this process, the photocatalyst gets excited via absorbing light and becomes more reactive by, *e.g.*, the formation of triplet states and electron-hole pairs.[7-8] The photocatalyst returns to its ground state through further chemical deactivation processes, and the absorbed light energy is stored in newly formed chemical bonds. These processes are similar to natural photosynthesis,[9] where solar energy is converted into chemical energy to sustain life on Earth.

Understanding these primary events in a photochemical transformation is essential for improving existing reactions and developing advanced schemes and materials. This includes the study of photoinduced non-equilibrium dynamical processes, such as internal conversion (IC) and intersystem crossing (ISC), or excitation energy transfer (EET) between chromophores.[10-11] For inter-chromophore transfer in a molecular aggregate, the relative orientation of excited molecules is essential.[12-13] This explains the need to determine the relative orientations of excited transition dipole moments (TDMs).

Ultrafast transient absorption spectroscopy (TAS) is a mature time-resolved technique that has been widely applied to study photophysical processes occurring in the excited electronic states on their intrinsic timescale,[14] leading to an accurate description of the electronic structure and population dynamics.[15-16] Isotropic TA spectra are usually obtained by setting the pump and probe pulse at magic angle (MA, 54.7°) to cancel the photo-induced anisotropy introduced by the linearly polarized pump pulse. By going beyond magic angle TAS – *e.g.*, by employing transient absorption anisotropy (TAA) as will be defined in Chapter 3 – we can obtain information on the relative orientation of the molecular TDMs orientations. TAA is one of the most popular methods to study TDMs based on setting the polarization of pump and probe parallel and perpendicular to each other while measuring TAS. TAA reveals the relative angle between the photo-excited and detected TDMs in its time dependence, and is also a method to detect otherwise hidden excited states.[17-18]

However, TAA comes with some limitations, for example, spectral overlaps, diverging signals, and loss of information on population dynamics. In this thesis, we present polarization-associated spectra (PAS) which retain the non-diverging spectral signatures of TAS, while being associated with the direction of the underlying TDMs.[19-21] As an extension of TAA, PAS are projections of the isotropic TA-spectrum into two orthogonal contributions, which can be either parallel or orthogonal to the initially excited TDM. When dealing with molecules with lower symmetry, the coordinate system can be rotated to isolate spectral signatures from TDMs that are neither parallel nor perpendicular to the initially excited TDM. It is this rotation of basis-set functions for PAS-analysis that represents a key novelty within this thesis.

We apply PAS to two different photoactive materials shown in Figure 1.1.

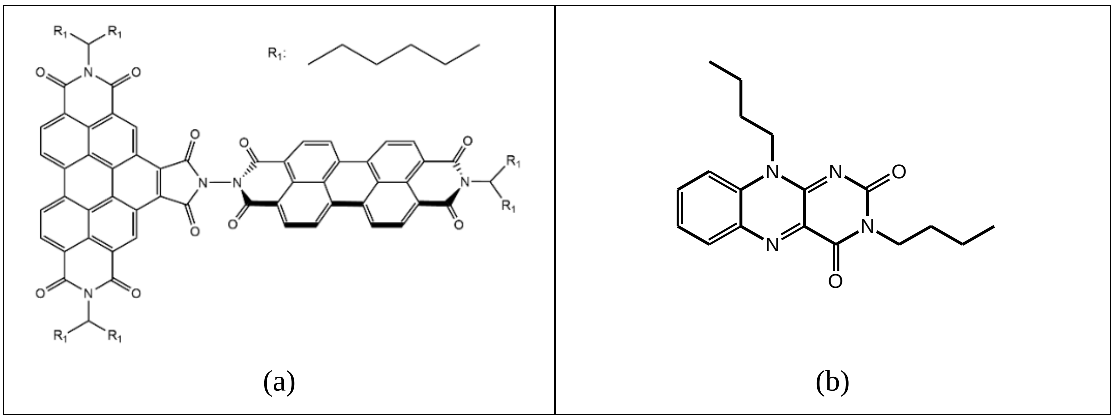

(a) (b)

Figure 1.1 The molecular structure of (a) Perylene-benzoperylene bisimide (D-A) and (b) 3,10-dibutylbenzo[g]pteridine-2,4(3H,10H)-dione) (quinoid flavin/ox-flavin).

i. Perylene-benzoperylene bisimide

Perylene bisimides (PBIs) and their derivatives are promising photocatalytic compounds that are extensively used for solar energy harvesting due to their chemical versatility and convenient spectroscopic properties, such as the high fluorescence quantum yield and photostability.[5, 22-28] Besides photocatalysis, they are also used as functional materials[22, 29-34], optical and electrical sensors.[35-39]

We apply the PAS methodology to the orthogonal intramolecular donor-acceptor (D-A) dyad perylene-benzoperylene bisimide (PBB) (Figure 1.1 (a)). This D-A molecule features an orthogonal arrangement of the donor (D) and acceptor (A) moieties which show efficient energy transfer time within 1 ps in experiment. Such an ultrafast transfer is clearly inconsistent with the simple Förster resonance energy transfer picture, suggesting inefficient transfer between D and A due to the orthogonality of their TDMs. By applying polarization-controlled TA spectroscopy, the decomposition of the TA data into PAS lets us ascribe spectral species and decay times to either donor- or acceptor moieties in the weakly coupled D-A system. This provides a strategy to greatly reduce spectral congestion in complex systems and thus allows detailed studies of electronic structure and electronic energy transfer.

This work has been published in:

Xu, Y.; Mewes, L.; Thyrhaug, E.; Sláma, V.; Šanda, F. e.; Langhals, H.; Hauer, J., Isolating pure donor and acceptor signals by polarization-controlled transient absorption spectroscopy. *J. Phys. Chem. Lett.* **2023,** *14*, 5390-5396.

ii. Quinoid oxidized flavin

Flavins are important naturally occurring chromophores in living organisms that play essential roles in metabolic and enzymatic processes.[40-42] Importantly, they exhibit multiple redox and protonation states.[43] In the organic laboratory, molecular flavins serve as versatile and easily modifiable catalysts, in which quinoid flavins as excited state oxidants.[6, 44] The corresponding photocatalytic cycle starts with the excitation of the quinoid flavin in its ground state to the singlet excited state ($^1\pi,\pi^*$), followed by an ISC to the photocatalytically active triplet state ($^3\pi,\pi^*$) within several nanoseconds.[44-46] The triplet yield can be further enhanced via re-excitation of the initially excited singlet state.[47-49] The desire to drive such excited state transitions efficiently underlines the importance of knowing the excited state TDM directions. However, despite a large body of work on transient spectroscopy on flavins,[50-52] little is known about the TDM orientation of excited state absorption transitions.

We employ PAS method to disentangle the TA signal of a quinoid flavin in solution, isolating distinct ESA-transitions. Furthermore, we determine the relative angle between the TDMs of two neighboring ESA features. By comparing to more conventional methods of extracting pure ESA signals, we highlight the advantages of our approach.

This work has been published in:

Xu, Y., Martin, T. P., Jänchen, M., Foja, R., Storch, G., Thyrhaug, E., de Vivie-Riedle, R., and Hauer, J., Determining Excited-State Absorption Properties of a Quinoid Flavin by Polarization-Resolved Transient Spectroscopy[J]. *J. Phys. Chem. A*, **2024**, 128, 19, 3830–3839

The above articles are summarized in more detail in Chapters 4.1-4.2, and reprints of the published manuscripts and supporting information are provided in Appendix B and C

In Chapter 2 we will briefly introduce the principles behind TAS and the experimental design of the employed experiment. Construction and testing of this setup were major parts of this thesis. Then the principle of polarization-controlled spectroscopy and an example of applying PAS will be introduced in Chapter 3.

2. TRANSIENT SPECTROSCOPY

Nowadays, optical spectroscopic techniques are widely applied for unraveling the properties and dynamics of atoms, molecules, oligomers, and aggregates. Steady-state (or linear) absorption spectroscopy based on Lambert–Beer's law[53] reflects the electronic structure, concentrations, conformations, surroundings, transition dipole moments (TDMs) magnitudes, and transition energies of molecules. However, steady-state spectroscopy cannot resolve the photo-induced ultrafast processes. In general, ultrafast processes refer to phenomena occurring on extremely short timescales, typically at the femtosecond (10^{-15} s) or picosecond (10^{-12} s) level, for example, IC, ISC, and EET.[10-11] Transient absorption spectroscopy (TAS), uses femtosecond ultrafast laser pulses as the pump to trigger the ultrafast process, offering the opportunity to measure these photoinduced processes on their intrinsic timescale, with temporal resolutions reaching down to tens of femtoseconds.[14, 54]

In this chapter, we will introduce the concept, experimental design, and data analysis of TAS in Chapter 2.1, Chapter 2.2, and Chapter 2.3, respectively.

2.1. THE CONCEPT OF TRANSIENT ABSORPTION

TAS experiments measure the change in a sample's absorption, or optical density (ΔOD), introduced by the pump pulse. As illustrated in Figure 2.1 (a), The probability of a molecule's interaction with polarized light is dependent on $cos^2\theta$, where θ represents the angle between absorption TDM and the light's polarization.[55] When θ is equal to 90°, the ΔOD will approach zero.

The pump pulse creates the nonequilibrium system state interrogated by the probe pulse. The desired ultrafast dynamics are recorded by repeating this measurement at different pump-probe delays, as illustrated in Figure 2.1(b). The recorded TA spectra contain various signal contributions. Due to the partial depopulation of the ground state after the sample has been excited, the probe experiences increased transmission, a negative signal appears at the wavelength positions of the linear absorption band, which is referred as the ground state bleach

(GSB). Stimulated emission (SE) gives out more photons in the probe beam pathway, also leading to a negative signal in the overall TA spectrum. The transition from an excited state to a higher-lying excited state presents a positive signal in the TA spectra, which is a linear absorption of the excited state called excited state absorption (ESA).

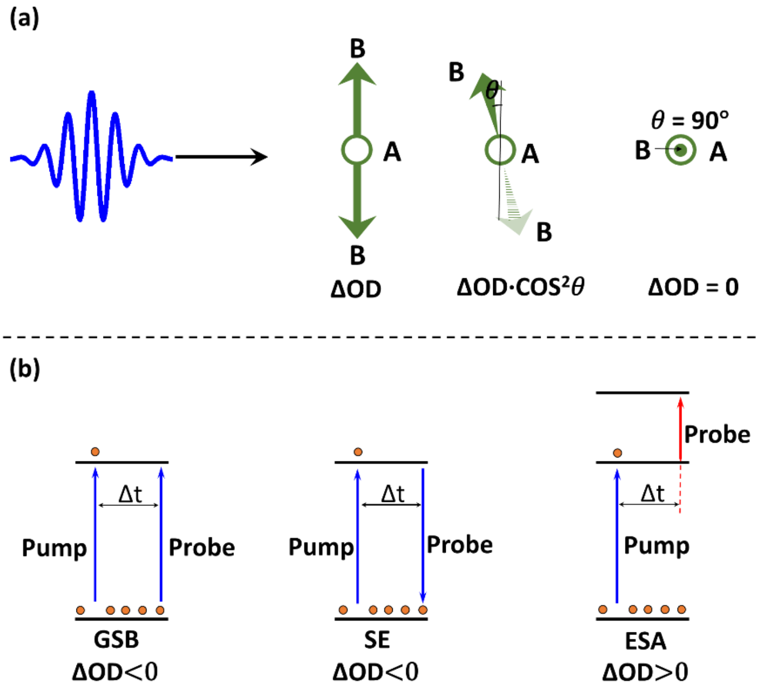

Figure 2.1 (a) The intensity of ΔOD introduced by the pump pulse depends on the angle (θ) between the pump polarization and the orientation of molecules' TDM. (b) shows the three contributions to a TA-signal: GSB – ground state bleach. SE – stimulated emission, and ESA – excited state absorption.

2.2. BROADBAND TRANSIENT ABSORPTION SPECTROSCOPY WITH TUNABLE PUMP PULSES

To obtain the ΔOD, we can do two measurements of the probe transmitted through the sample, one with and one without the pump pulse ($S_{\mathrm{P-on}}$ and $S_{\mathrm{P-off}}$), respectively, see Figure 2.2, the $S_{\mathrm{P-P}}$ measurement corresponds to the difference

$$S_{\mathrm{P-P}} = S_{\mathrm{P-on}} - S_{\mathrm{P-off}} \qquad \textit{eq. } 2\text{-}1$$

The $S_{\mathrm{P-on}}$ and $S_{\mathrm{P-off}}$ scenarios are differentiated by blocking every second pump pulse.

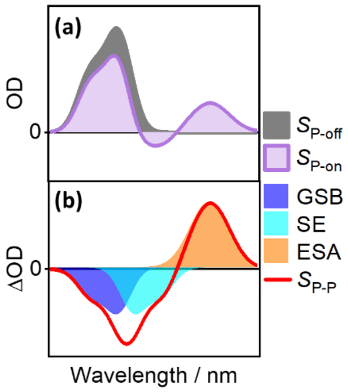

Figure 2.2 The transmission spectra for pump-on and pump-off are compared in (a). (b) shows the TA signals consisting of GSB, SE, and ESA.

According to the Beer-Lambert law[53] and *eq.* 2-1, $S_{\mathrm{P-P}}$ can be expressed as follows:[56-57]

$$S_{\mathrm{P-P}}(\lambda, \Delta t) = -\log\left(\frac{I_{\mathrm{P-on}}}{I_0}\right) + \log\left(\frac{I_{\mathrm{P-off}}}{I_0}\right) = -\log\left(\frac{I_{\mathrm{P-on}}}{I_{\mathrm{P-off}}}\right) \qquad \textit{eq. } 2\text{-}2$$

Figure 2.3 illustrates the basic experimental realization of TAS. The pump laser is usually tunable to a specific center wavelength and bandwidth, via a non-collinear parametric amplifier (NOPA).[58-60] The polarization of the pump pulse is controlled by a half-waveplate ($\frac{1}{2}\lambda$ plate). The probe pulse is usually a broadband supercontinuum, generated by focusing the laser on a bulk material such as sapphire or CaF_2. The pump and probe pulses are spatially overlapped in the sample and the time delay between the pump and the probe pulse is experimentally controlled by changing the beam path with a linear motor stage. The pump pulse is alternately blocked and passed through using a fast-rotating chopper wheel to create pump-on or pump-off situations. The detector, such as CCD, records the probe spectra on a shot-to-shot basis, i.e. at the laser's certain repetition rate, which was 5 kHz for the experiments described in this thesis.

The measurements related to this thesis are performed on a home-built TA setup. We split a train of 800 nm, 36 fs FWHM fundamental laser pulses at a 5 kHz repetition rate from a Coherent Legend amplified laser into pump and probe arms and conducted tunable pump and broadband white light probe TAS measurements on D-A system and flavin. Details about the pump and probe pulse generation will be introduced in Chapter 2.2.1 and Chapter 2.2.2

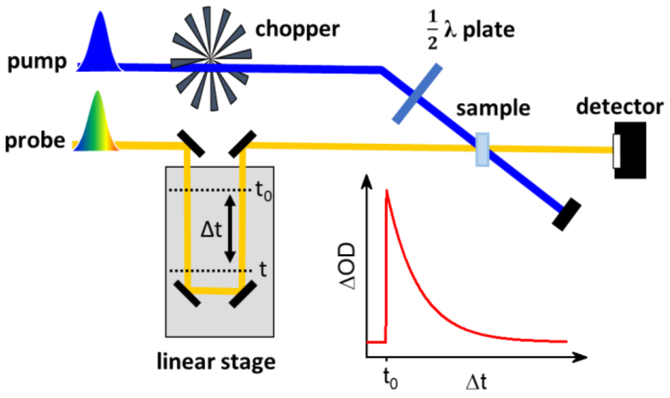

Figure 2.3 The transmission spectra for pump-on and pump-off are compared in (a). (b) shows the TA signals consisting of GSB, SE, and ESA. (c) Schematics of a TAS experiment. The pump and probe beams are spatially overlapped at the sample position. The pump pulses are intermittently blocked using a fast-rotating chopper wheel to create pump-on or pump-off situations. The probe pulse's time delay can be adjusted using a linear motorized stage. The inset shows the time trace of the pump-probe signal at a fixed detection wavelength.

2.2.1. Tunable Pump Pulse

In a pump-probe experiment, the wavelength of the pump pulse must match a specific molecular absorption band. In this thesis, we used 400 nm and 325 nm pump pulses, generated by different methods.

- **SHG of fundamental pulse as pump: 400 nm**

To excite the donor moiety of the perylene D-A system and the S_1 band of quinoid flavin, a 400 nm pump pulse is used, see Figure 2.4 (a). 400 nm excitation is obtained via second harmonic generation (SHG) of the 800 nm fundamental pulse in a 200 µm angle type I beta-barium borate crystal (BBO) with a 29.2° cutting angle. Before the BBO, the beam diameter was reduced from 9 mm to 3 mm by a Galilean telescope consisting of a plano-convex lens with 300 mm focal length and a plano-concave lens with 100 mm focal length. A 4° fused silica (FS) wedge was employed to reflect ~ 4% of the SHG. As the SHG is polarized vertically with respect to the laser table while the fundamental is polarized horizontally, reflection at Brewster angle will be dominated by the SHG-light.[61] We pick the reflection from the front surface and use another dielectric mirror to separate the remaining 800 nm fundamental from the pump beam.

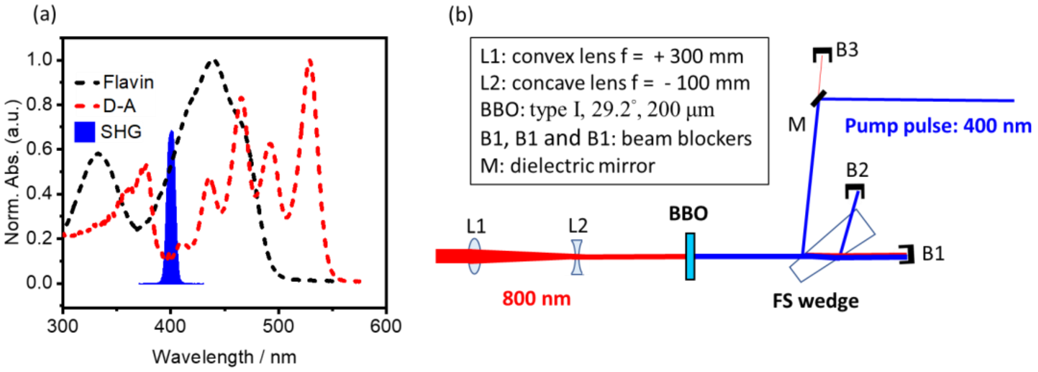

Figure 2.4 (a) The UV-Vis spectra of the D-A system (grey dashed) and the quinoid flavin (grey dotted), and the spectrum of the desired pump pulse (blue filled). (b) 400 nm pump pulse generated by frequency doubling of 800 nm fundamental beam.

- **SHG of NOPA output as pump: 325 nm**

To excite the higher lying S_3 band of the flavin, we need a pump pulse with 325 nm central wavelength, see Figure 2.5 (a). As the tuning range of the NOPA in our lab is 490 nm -700 nm, the 325 nm pump cannot be generated directly. Hence, frequency doubling of the suitable NOPA output (650 nm) is necessary.

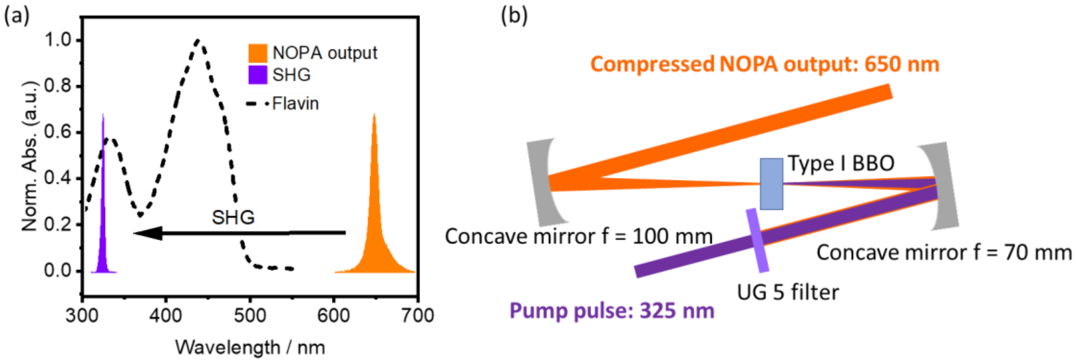

Figure 2.5 (a) The UV-Vis spectrum of the flavin (black dashed), and the spectrum of the employed pump pulse (purple filled). (b) 325 nm pump pulse generated by frequency doubling of the NOPA output centered at 650 nm.

The sketch of our two-stage NOPA is depicted in Figure 2.6 (a) and based on the design by Riedle and co-workers.[58] The incoming beam reduced by a Galilean telescope is split into two arms with a beam splitter. The 5% reflection is focused on a 3 mm thick sapphire crystal to generate seed white light. The 95% transmittance is frequency doubled by a 200 μm, Type I BBO crystal with a 29.2° cutting angle. The SHG was split by a 1:3 beam splitter. The weaker reflection is used as the pump for the pre-amplification (1st) stage, see Figure 2.6 (b), and the stronger transmittance for the main-amplification (2nd) stage, see Figure 2.6 (c). The NOPA was designed to generate a narrow-band output pulse. To achieve the narrow bandwidth, both the white light and the pump pulse are chirped, by a 17.88 mm BK7 chirper block and a pair of 5 mm fused silica substrates put at Brewster angle, respectively. The NOPA output pulse is centered at 650 nm and with 12 nm bandwidth, and compressed with a prism compressor using two fused silica prisms. This leads to a near-Fourier limited pulse duration of ~52 fs, as determined by Second Harmonic Generation Frequency Resolved Optical Gating (SHG-FROG).[62]

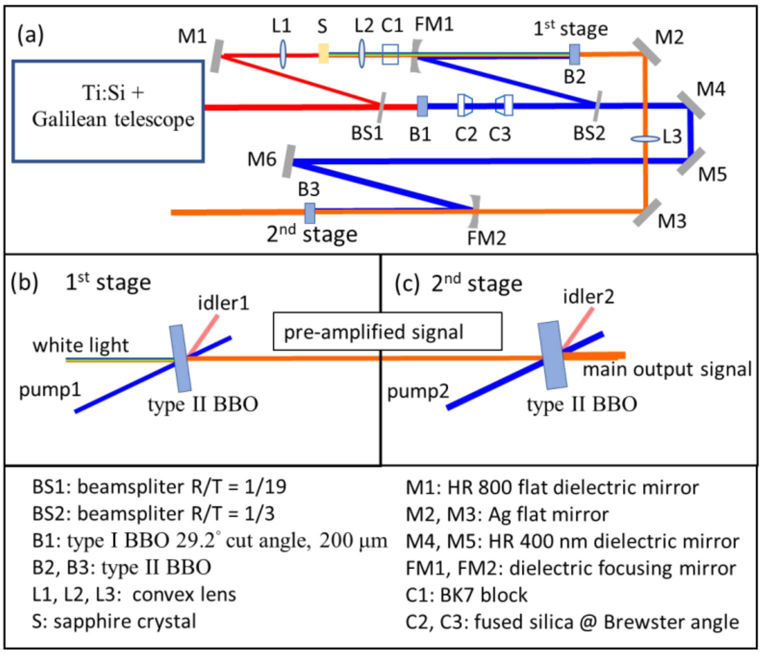

Figure 2.6 (a) The top view of the two-stage NOPA. (b) The side view of the pre-amplification (1st) stage and (c) the main output amplification (2nd) stage

The compressed NOPA output beam is focused into the BBO crystal (type I, 40° cut angle, 200 μm) by using a 100 mm focusing spherical mirror and recollimated by a 70 mm spherical focusing mirror. The residual 650 nm fundamental light is filtered out by using a 1 mm thick UG5 filter, see Figure 2.5 (b).

2.2.2. BROADBAND PROBE

As illustrated in Figure 2.7 (a), ultrabroadband white light for detection is generated by focusing 4 μJ of 800 nm light into a 5 mm thick CaF_2 crystal. To avoid damage, the crystal is continuously moved in a plane orthogonal to the beam direction. The focal length of 100 mm was chosen to maximize the spectral bandwidth of the white light, see Figure 2.7 (b). By careful optimization, we obtain a spectrum extending down to 370 nm. The white light pulse is collimated using a 100 mm focal length spherical mirror and the intensity of the 800 nm driving pulse is decreased using a heat-absorbing filter.

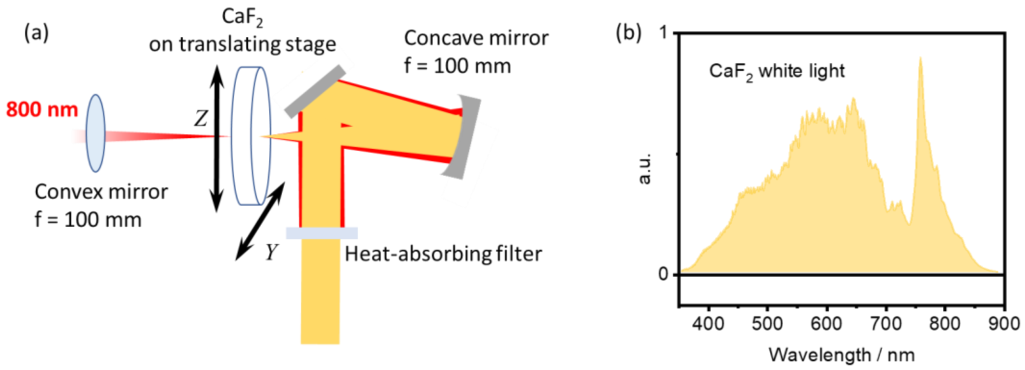

Figure 2.7 (a) schematic illustration of the white light stage, in which the CaF_2 is put on a Y-Z translating stage. (b) shows the spectrum of the white light after the heat-absorbing filter.

For detection in the TAS setup, the white light is split into a probe part and a reference part. The probe spatially overlaps with the pump pulse at the sample position and is recollimated after the sample by using an achromatic lens. The probe and reference pulses are detected using a home-built prism spectrometer in combination with a pair of high-speed CMOS linear array cameras (Glaz LineScan-I-Gen2, Synertronic Designs).

2.3. TRANSIENT ABSORPTION DATASET ANALYSIS - GLOBAL AND TARGET ANALYSIS

The measured TAS data are plotted in their time- and wavelength-dependence, $S_{\mathrm{P-P}}(\lambda, \Delta t)$. This multidimensional dataset needs to be analyzed to retrieve the desired information such as excited state lifetimes. A typical model to fit the TA data is given by a discrete sum of exponential functions with different coefficients.[63-65]

$$S(\lambda, \Delta t) = \sum_i A_i(\lambda) e^{-t/\tau_i} \qquad eq.\ 2\text{-}3$$

Here, A_i is the pre-exponential amplitude of species i and τ_i is the corresponding time constant. Instead of analyzing the data at every single wavelength, we prefer a global analysis of multiple kinetic traces recorded in dependence of wavelength or other experimental variables.[66-67] The most common global analysis procedure is global lifetime analysis (GLA). By plotting the pre-exponential amplitudes for each lifetime component against the wavelength, we obtain a compact representation of the system's dynamics, referred to as decay-associated spectra (DAS).[64]

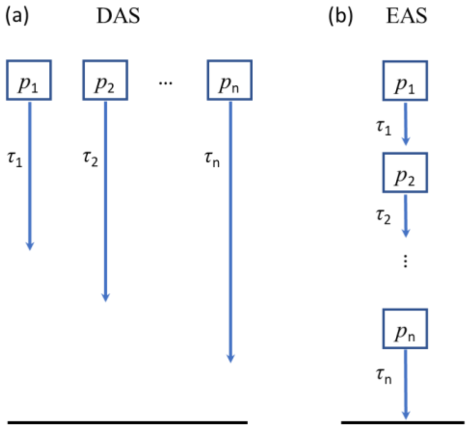

Figure 2.8 Schemes depicting possible decay types of the compartmental models with n components: (a) decay-associated spectra (DAS) and (b) evolution-associated spectra (EAS).

DAS represents a parallel decay scheme, as depicted in Figure 2.8 (a). This scheme is interpreted as the loss or gain of spectra with a certain lifetime, representing the decay and rise of these states. For the DAS, negative (positive) amplitudes indicate decay (rise) of GSB/SE signal, in contrast, positive (negative) amplitudes represent decay (rise) of excited-state absorption (ESA). For sequential processes, *e.g.*, EET and vibrational cooling, evolution-associated spectra (EAS) offer more insight than DAS. The EAS model represents the spectral evolution by assuming the system can be described by a series of sequentially excited compartments, see Figure 2.8 (b).

The fastest resolvable system response in the experiment is sometimes limited by the instrument response function (IRF), which is the convolution (⨂) of the shape of the exciting pulse and the detector (probe pulse) response.

$$S(\lambda,\Delta t) = \sum_i A_i(\lambda) e^{-\frac{t}{\tau_i}} \otimes IRF(t) \qquad \textit{eq. } 2\text{-}4$$

The IRF can be measured experimentally, *e.g.*, by using a known reference sample or pure solvent, or be calculated by including a parameterized description of the instrument response in the model function.[66] The IRF is often assumed to be a Gaussian function with two parameters for the location and the full width at half maximum (FWHM). Sometimes the IRF also includes a coherent artifact (CA) in the ultrafast experiments, which can lead to distortions in the recorded signal at temporal overlap between pump and probe.[66, 68-69] Accordingly, the CA originates from non-linear interactions between the pump and the probe pulses, *e.g.*, cross-phase modulation, double quantum coherence, or stimulated Raman amplification (SRA).[68, 70] The CA can be approximated by a function composed of a Gaussian and/or its first and second derivatives.[67]

SHORT SUMMARY

In this chapter, we briefly introduced the principle, experimental design, and data process of transient absorption spectroscopy. In the next chapter, we will introduce the principle of polarization-associated spectra based on polarization control.

3. POLARIZATION-CONTROLLED SPECTROSCOPY

The polarization of light is defined by its electric field's direction. For linearly polarized light, the electric field oscillates in a plane perpendicular to its wave vector. As mentioned in Chapter 2.1, when a sample is illuminated by polarized light, molecules have the highest probability of interacting with the light whose $\boldsymbol{E}$-field is aligned parallel to the molecular TDM due its vectorial nature; this is called photoselection. A general model for photoselection was given by Jablonski in 1935 to treat the theory of the polarization of emission of dye solutions.[71] The probability of absorption is proportional to the $cos^2\theta$, where θ is the angle between absorption TDM and the polarization of light.[55]

TAS measurements typically involve linearly polarized pump and probe pulses. This implies that photo-induced anisotropy occurs when an isotropic sample is excited by the linearly polarized pump pulse – the population of excited molecules becomes partially oriented. The use of polarized light in spectroscopy adds an extra dimension to the measurement, providing details about the anisotropic properties and structural characteristics of materials, as well as on the dynamics of rotation of a molecule out of the initially excited orientation (rotational diffusion).[72-73]

In this chapter, we introduce polarization-controlled spectroscopy. Polarization-controlled steady-state spectroscopy will be introduced in Chapter 3.1. After that, we discuss TA anisotropy in Chapter 3.2 and polarization-controlled TAS in Chapter 3.3.

3.1. LINEAR DICHROISM AND FLUORESCENCE ANISOTROPY

Steady-state spectroscopic methods with polarized light, such as linear dichroism (LD) and fluorescence anisotropy (FA), allow researchers to control and exploit the orientation-dependent responses of the sample to light.[74-75]

LD is a spectroscopic technique that measures the differential absorption of polarized light by a sample. It is particularly useful for studying the structures of biomacromolecules such as DNA, fibrous proteins, membrane proteins, and peptides, which are not easily characterized by other techniques such as NMR and X-ray.[76-77] The technique can be applied to the sample with a laboratory-defined orientation axis, they can be either intrinsically oriented, *e.g.*, crystal, or be oriented during an experiment by external forces, *e.g.*, the stretched film.[76, 78] The LD spectrum is obtained as follows:

$$\mathrm{LD} = A_{\parallel} - A_{\perp} \qquad \textit{eq.}\ 3\text{-}1$$

Here, $A_{\parallel}$ ($A_{\perp}$) is the absorbance when light is polarized parallel (orthogonal) with the orientation axis. A schematic depiction of an LD measurement is shown in Figure 3.1. The desired state of linearly polarized light is usually selected by using polarizers.[74] The sample is placed between the polarizer and detector, and the angle between the polarizer and the sample is adjustable. The absorbance is then measured by a detector as a function of the polarizer angle.

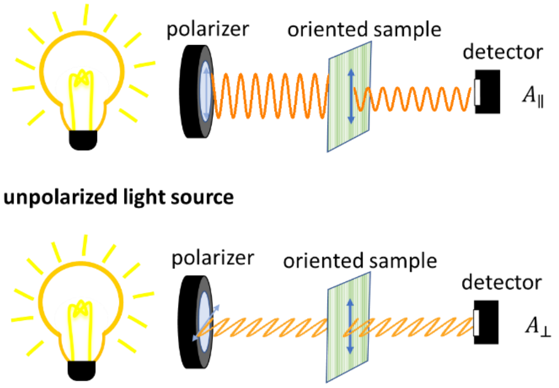

Figure 3.1 Schematic depiction of the linear dichroism spectroscopy measurement. Unpolarized light is polarized as it passes through a polarizer. The stretched sample's TDMs are oriented vertically. Absorption measurements are taken when the light's polarization is parallel (top panel) or orthogonal (bottom panel) to the sample's orientation.

In isotropic samples, *e.g.*, the liquid solution, LD spectroscopy cannot be applied as the molecules are usually randomly oriented. In this scenario, fluorescence-based methods such as FA are more useful.[75, 79] In FA, linearly polarized excitation is used to generate photo-induced anisotropy of the sample. The emitted fluorescence may show anisotropy as defined below, which can be analyzed.

In the FA experiment, we need a polarizer to generate polarized excitation light and analyze the emitted fluorescence by another polarizer (analyzer). The classical L-format measurement of

FA is illustrated in Figure 3.2. When the polarization of the excitation beam is set vertically, (Figure 3.2, left panel), we can measure I_{VV} and I_{VH} by setting the polarization of the analyzer vertically and horizontally, respectively. The fluorescence anisotropy is defined by:

$$FA = \frac{I_{VV} - I_{VH}}{I_{VV} + 2I_{VH}} \qquad eq.\ 3\text{-}2$$

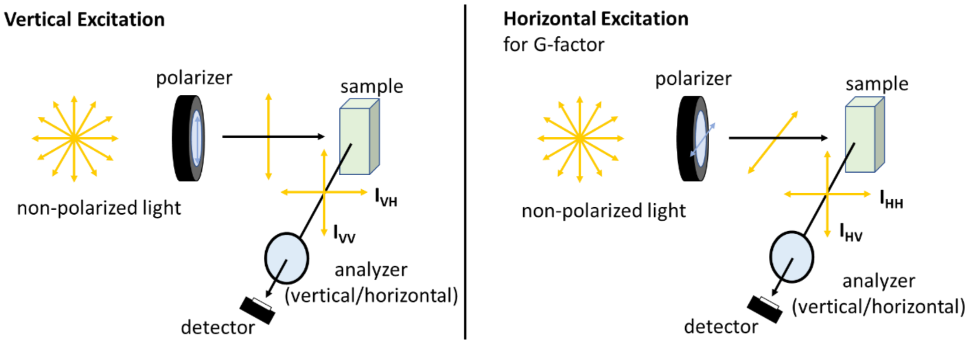

Figure 3.2 Schematic diagram for L-format measurements of fluorescence anisotropy. The left panel shows the measurement when the sample is excited by a vertically polarized beam. By using an analyzer, we can measure both the vertical and horizontal components of the emission light. The right panel depicts the same measurement but with a horizontally polarized excitation beam. The latter measurement is typically used to determine the G-factor.

In practice, the inherent polarization effects of the instrument optics should be corrected,

$$\mathrm{FA} = \frac{I_{VV} - G(\lambda_{ex})I_{VH}}{I_{VV} + 2G(\lambda_{ex})I_{VH}} \qquad eq.\ 3\text{-}3$$

The $G(\lambda_{ex})$ factor, which is the ratio of the sensitivities of the detection system vertically and horizontally, is determined as,

$$G(\lambda_{ex}) = \frac{I_{HV}(\lambda_{ex})}{I_{HH}(\lambda_{ex})} \qquad eq.\ 3\text{-}4$$

where $I_{HV}(\lambda_{ex})$ and $I_{HH}(\lambda_{ex})$ are the intensities of vertical and horizontal fluorescence measurements with horizontal excitation, respectively, see Figure 3.2, right panel.

We assume that there is no loss of polarization due to the rotation of the chromophore during the lifetime of the emission process or due to energy transfer between chromophores. For an isolated transition, we may then write for the anisotropy r:

$$r = \frac{2}{5} \cdot \frac{3 \cdot cos^2\theta - 1}{2} \qquad eq.\ 3\text{-}5$$

Here, θ is the angle between the absorbing and emitting TDMs.

3.2. TRANSIENT ABSORPTION ANISOTROPY

Linearly polarized excitation beams generate photo-induced anisotropy in the isotropic sample which can be experimentally measured by FA experiments. Analogously to FA, photo-induced TA anisotropy can also be measured because the laser pulses for both pump and probe are inherently linearly polarized. Similar to $eq.$ 3-2, TA anisotropy can be calculated as:

$$r(\lambda, t) = \frac{S_{\parallel} - S_{\perp}}{S_{\parallel} + 2S_{\perp}} \qquad eq.\ 3\text{-}6$$

$S_{\parallel}$ and $S_{\perp}$ are the TA signals measured by setting the pump and probe pulse parallel and perpendicular to each other, as depicted in Figure 3.3. From $eq.$ 3-5, we know the $r(\lambda, t)$ values are related to the angle θ between the pump pulse polarization and the detected TDM for isotropic sample.

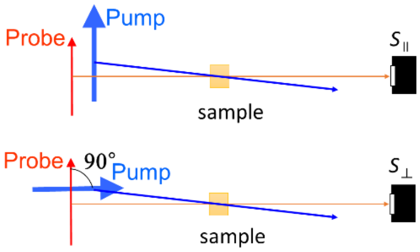

Figure 3.3 Transient absorption measurements were accomplished by setting the pump and probe pulse parallel and perpendicular to each other.

In a standard TA measurement, one would like to avoid dynamics caused by slow diffusion of the molecule out of the initially excited orientation. In other words, one has to ensure that $r = 0$, which is achieved by setting the angle between pump and probe polarization at MA. Alternatively, we can obtain the isotropic spectra by using $S_{\parallel}$ and $S_{\perp}$, as they include all signal components from the three-dimensional axes in space equally.

$$MA = \frac{S_{\parallel} + 2S_{\perp}}{3} \qquad eq.\ 3\text{-}7$$

While TA measurement in MA-orientation report on population dynamics of the excited molecule, TA anisotropies or measurements of $r(\lambda, t)$ reveal the direction change of TDMs during the ultrafast photophysical or photochemical process.[80-81] According to *eq*. 3-6, in an ideal case, *e.g.*, a single transition with no spectra overlap, the anisotropy value r will be limited within 0.4 and −0.2, corresponding with the θ from 0° to 90°. In addition, TA anisotropy measurements have been used as a tool to determine the rotational diffusion time,[82-83] which can be observed directly by exponential fitting of the anisotropy-time plot.

However, two problems of TA anisotropy spectroscopy stand out:

i. Unlike fluorescence, which is recorded by using the intensity of luminescence as an absolute value, TA signals are signed. Signals may cancel with each other when two signals with different signs overlap, *e.g.*, negative GSB and SE signals overlapping with positive ESA signals. In this case, the $r(\lambda, t)$ will diverge due to the denominator in *eq*. 3-6 is approaching zero.

ii. In contrast to conventional TA signals, $r(\lambda, t)$ does not directly reflect population dynamics but reports on changes in the TDM orientations over time. This can make the time evolution of TA anisotropy spectra difficult to disentangle and interpret.

To solve these problems, we will introduce our strategy to calculate the polarization-associated spectra (PAS) by using polarization control, which can either retain the spectral signatures of TA or associate it with the direction of the underlying TDMs. Such strategies are already well-established in polarization-controlled steady-state spectroscopies, with the method of stepwise reduction by Thulstrup, Eggers, and Michl[84-86] as a straightforward technique to extract relative TDM angles from linear dichroism data.

3.3. POLARIZATION-CONTROLLED TA

A first step in avoiding the problems discussed to TA anisotropy is to discuss the opportunities and benefits of polarization-control in TAS in general. To quantify the response of isotropic samples to polarized light, we need to consider two Cartesian frames: the laboratory and molecular Cartesian frames. We introduced the laboratory axes X, Y, and Z, and the molecular axes, x, y, and z, as depicted in Figure 3.4 (a). Here we will express the laboratory signals by using the combinations of molecular frame signals.

The probabilities of photon absorption along each molecular axis x, y, and z are defined as r_x, r_y, and r_z, with $r_x + r_y + r_z = 1$, see Figure 3.4 (a). For the excited molecules, the transition probabilities along each direction are q_x, q_y, and q_z, respective to coordinate transformed molecular axes x', y', and z', similarly, $q_x + q_y + q_z = 1$, see Figure 3.4 (b). The total probability of being excited and detected (pump and probe) can be expressed as the product of each r_i and q_j, *e.g.*, $r_x q_x$, $r_x q_y$, the complete form can be found in Appendix A.

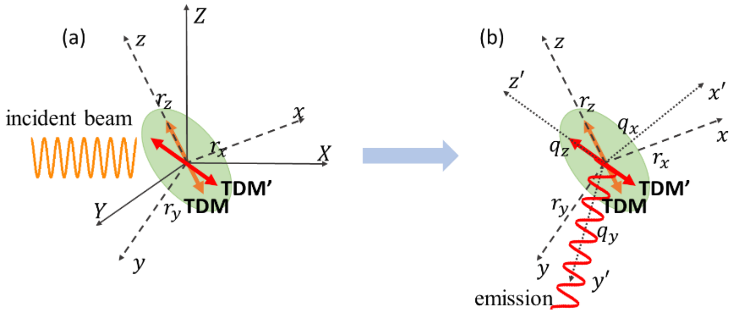

Figure 3.4 Definition of the coordinate axes (a) incident beam in laboratory axes and the TDM been excited in molecular axis, (b) coordinate transformation between the excited TDM been and the detected TDM (or emits a photon).

The experimentally measured signals along laboratory axes X, Y, and Z can be expressed with combinations of $r_i q_j$ with suitable pre-factors. These pre-factors are encoded in a rank 4 Cartesian tensor [87-89] (*eq.* A-4) after considering rotational averaging, which connects the laboratory frame and molecular frame. Details of this rank 4 tensor and pre-factor calculation can be found in Appendix A. Once we have the prefactors, the intensity of detected signals polarized along the laboratory axes should be proportional to

$$\begin{aligned} I_Z &\propto 3(r_x q_x + r_y q_y + r_z q_z) + q_x(r_y + r_z) + q_y(r_x + r_z) + q_z(r_x + r_y) \\ I_Y = I_X &\propto (r_x q_x + r_y q_y + r_z q_z) + 2[q_x(r_y + r_z) + q_y(r_x + r_z) + q_z(r_x + r_y)] \end{aligned} \qquad eq.\ 3\text{-}8$$

Here, I_Z and I_Y, refer to the emitted light intensities or observed ΔOD, polarized along Z and Y, respectively. The proportionality constants are the same for the appropriate pair of the three intensities (or ΔODs), the determination of which is not required. The same results can be obtained by directly integrating over all the Euler angles while calculating the products of photo-excitation probabilities along all laboratory axes and molecular axes, which has been done by Albrecht.[19, 90]

3.3.1. POLARIZATION ASSOCIATED SPECTRA

In *eq.* 3-8 we have the intensity of light polarized along the laboratory axes.[90] We choose the absorption and emission to occur in the molecular *yz*-plane so that both absorption and emission along *x* are equal to zero, and the expressions in *eq.* 3-8 reduce to:

$$\begin{aligned} I_Z &= 3\left(r_y q_y + r_z q_z\right) + r_z q_y + r_y q_z \\ I_Y = I_X &= \left(r_x q_x + r_y q_y\right) + 2[r_z q_y + r_y q_z] \end{aligned} \qquad \textit{eq. } 3\text{-}9$$

The polarized "unit-vector" spectra can now be constructed by requiring that the absorption from both components sum up to one, i.e.: $r_y = 1 - r_z$ and $r_z = 1 - r_y$. This leads to:

$$\begin{aligned} I_Z &= \left(1 + 2r_y\right)q_y + (3 - 2r_z)\left(1 - q_y\right) \\ &= (3 - 2r_z)(1 - q_z) + (1 + 2r_z)q_z \\ I_Y = I_X &= \left(2 - r_y\right)q_y + \left(1 + r_y\right)\left(1 - q_y\right) \\ &= \left(1 + r_y\right)(1 - q_z) + (2 - r_z)q_z \end{aligned} \qquad \textit{eq. } 3\text{-}10$$

These expressions are inserted into the expression for the fundamental anisotropy r_0:

$$\begin{aligned} r(\lambda, t) &= = \frac{(I_Z - I_Y)}{(I_Z + 2I_Y)} = \frac{(3 - 2r_z) - (1 + r_z)}{(3 - 2r_z) + 2(1 + r_z)} \\ &= \frac{\left(1 + 2r_y\right) - \left(2 - r_y\right)}{\left(1 + 2r_y\right) + 2\left(2 - r_y\right)} \end{aligned} \qquad \text{eq. 3-11}$$

Let's assume that the emission is polarized along one of the transferred axes, which we assume to have an angle β with respect to the *z*-axis. For the definition of β, see Figure 3.5. We can then set $q_y = cos^2\beta$ and $q_z = sin^2\beta$. The spectral "unit vectors" along *y* and *z* can now be related directly to the experimentally determined anisotropy by rearranging the two terms on the right to give:

$$r_z = \frac{3cos^2\beta - \left(2 - 5 \cdot r(\lambda, t)\right)}{3 \cdot (2cos^2\beta - 1)}$$

$$r_y = \frac{3cos^2\beta - (5 \cdot r(\lambda, t) + 1)}{3 \cdot (2cos^2\beta - 1)} \qquad eq.\ 3\text{-}12$$

The signal combinations allow us to decompose the isotropic spectrum $S_{MA}(\lambda, t)$ into signals with two orthogonal contributions:[19-20]

$$\begin{aligned} S_{z-\beta} &= \left(S_{\parallel}(\lambda, t) + 2 \cdot\ S_{\perp}(\lambda, t)\right) \cdot \left(\frac{3\cos^2\beta - \left(2 - 5 \cdot r(\lambda, t)\right)}{3 \cdot (2\cos^2\beta - 1)}\right) \\ &= 3 \cdot S_{MA}(\lambda, t) \cdot \left(\frac{\cos^2\beta - (1 - \cos^2\theta)}{(2\cos^2\beta - 1)}\right) \\ S_{y-\beta} &= \left(S_{\parallel}(\lambda, t) + 2 \cdot\ S_{\perp}(\lambda, t)\right) \cdot \left(\frac{3\cos^2\beta - (5 \cdot r(\lambda, t) + 1)}{3 \cdot (2\cos^2\beta - 1)}\right) \\ &= 3 \cdot S_{MA}(\lambda, t) \cdot \left(\frac{\cos^2\beta - \cos^2\theta}{(2\cos^2\beta - 1)}\right) \end{aligned} \qquad eq.\ 3\text{-}13$$

The term $\frac{1}{3}\left(S_{\parallel}(\lambda, t) + 2 \cdot\ S_{\perp}(\lambda, t)\right)$ is the isotropic spectrum $S_{MA}(\lambda, t)$. θ is the angle of angle between pumped and probed TDMs.

After multiplication with each unit vector, we obtain polarization-associated spectra (PAS) – $S_{z-\beta}$ and $S_{y-\beta}$. This representation is in the macroscopic lab frame; suitable linear combinations of these spectra may express the signal in terms of components in the molecular frame and thus bring better insight into the relative orientation of molecular TDMs.

When $\beta = 0°$, r_z and r_y represent unit vectors along the axis and xy-plane, which are defined as the axis orientated parallel and the plane perpendicular to the polarization of the excitation pulse, respectively. Hence, $S_{z-0°}$ and $S_{y-0°}$ are the spectra that allow for decomposing the $S_{MA}(\lambda, t)$ into signal contributions parallel to the excited transition and contributions orthogonal to the excited transition, respectively. The expression when $\beta = 0°$ has been reported in the former research from Thyrhaug et. al.[20, 91] Our expression here is more general.

When dealing with molecules with low symmetry – which probably gives an ESA transition (TDM') neither parallel nor perpendicular to the GSB transition (TDM) – coordinate transform can be considered as a change of β, see Figure 3.5. The application of PAS to a hypothetical system will be shown in the next chapter.

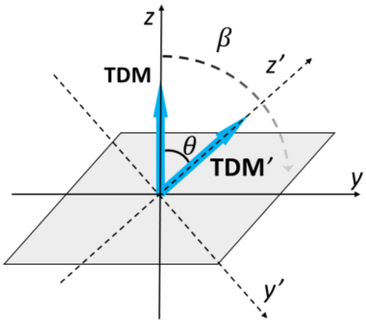

Figure 3.5 Definition of angles θ and β. The former spans between pumped and probed TDMs of the investigated molecule, while β stands for the angle between the pumped TDM and the coordinate system, in which the signal components S_z and S_y are defined.

3.3.2. A HYPOTHETICAL EXAMPLE

Here we will show an example of how to apply the PAS on TAS of a trial system which is generated by adding up Gaussian functions, as depicted in Figure 3.6(a). The TA spectrum of the trial system contains a GSB peak at 400 nm, an SE peak at 460 nm, and three ESAs peak at 320 nm (ESA1), 600 nm (ESA2), and 720 nm (ESA3), respectively. TA signals with parallel and perpendicular pump-probe configurations ($S_{\parallel}$ and $S_{\perp}$) are obtained by adjusting the intensities of the individual bands until calculated TAA reaches 0.4 for the GSB/SE and ESA3, -0.2 for ESA1, and an intermediate value for ESA2. The $S_{\parallel}$ and $S_{\perp}$ are plotted in Figure 3.6 (b), we can see the signal diverges at ~ 350 nm and ~ 550 nm, where the TA spectra cross zero, which was one of the problematic aspects of TAA as discussed in section 3.2.

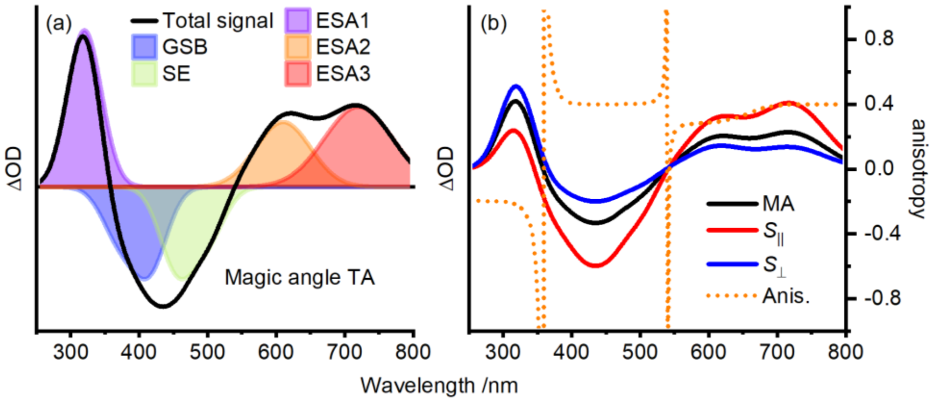

Figure 3.6(a) Trial TA spectrum at time t of a trial system, the TA spectrum (black solid) is the sum of GSB (blue filled), SE (light green filled), and three ESAs (violet, orange, and red filled). (b) Parallel ($S_{\|}$) and perpendicular ($S_{\perp}$) TA spectra compared with MA spectrum and TAA.

In Figure 3.7, we use *eq*. 3-13 and set $\beta = 0°$; the resulting spectra are plotted as $S_{z-0°}$ and $S_{y-0°}$. We can see the GSB and SE signals appear only in $S_{z-0°}$ spectrum and disappear in $S_{y-0°}$ because the TDMs of GSB and SE are parallel with the polarization of the pump pulse. Additionally, the ESA3 feature also disappears in $S_{y-0°}$, indicating the TDM of ESA3 parallels with that of GSB and SE. Due to the disappearance of GSB/SE and ESA3 in $S_{z-0°}$, $S_{y-0°}$ isolates the pure spectra of ESA1 and ESA2 from the total signal. As ESA1 disappears completely in $S_{z-0°}$ and magnifies in $S_{y-0°}$, we can deduce that ESA1 has a TDM orthogonal to the TDM of GSB/SE.

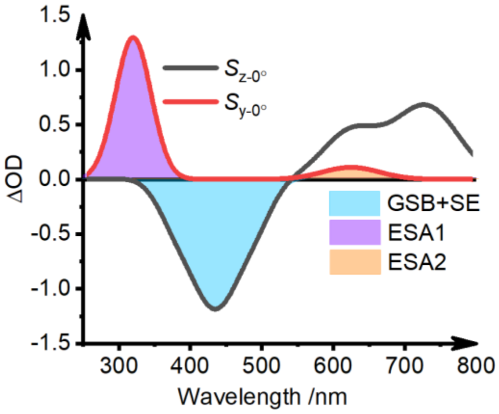

Figure 3.7 $S_{z-0°}$ (black solid) and $S_{y-0°}$ (red solid) spectra of the trial system, compared with sum of GSB and SE (light blue filled), ESA1 (violet filled), and ESA2 (orange).

However, ESA2 can be found in both S_{z-0° and S_{y-0°, indicating it is neither parallel nor orthogonal with GSB, SE. In this case, we change the coordinate angle β to find the right direction of the TDM. We monitored the $S_{z-\beta}$ signals at 600 nm, where ESA2 predominates while adjusting β from 0° to 35°. We then plot the ΔODs with respect to their corresponding angles.

We can see when $\beta \sim 26^\circ$, ΔOD for S_{y-26° approaches zero. In this case, β must be equal to θ, or in other words: we can conclude that the TDM of ESA2 has a 26° angle with GSB and SE.

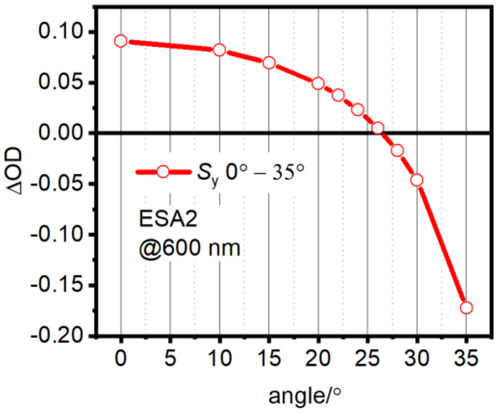

Figure 3.8 $S_{y-\beta}$ signal of the trial system at 600 nm for β values ranging from 0° to 35°.

The S_{z-26° and S_{y-26° are plotted in Figure 3.9, where S_{y-26° is plotted inversely to show ESA3 with the conventional positive sign. The sign flips to negative due to the rotation of the coordinate system by 26°.

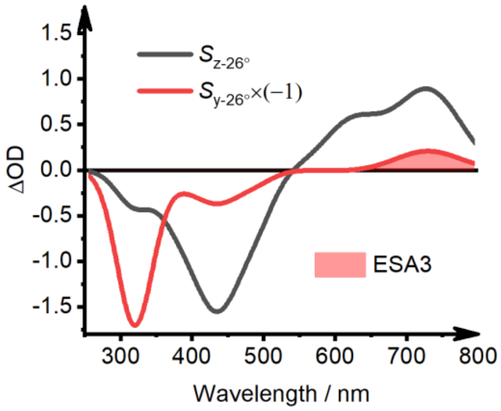

Figure 3.9 S_{z-26° (black filled) and S_{y-26° (red filled) spectra of the trail system, in which the S_{y-26° is flipped compared with the ESA3 (red filled region).

In this example, we successfully disentangled the GSB/SE and three ESA bands from the magic angle spectra. This approach is generally applicable to data with angles between TDMs that are feasible different from parallel.

SHORT SUMMARY

In this chapter and the according chapters in the appendix, we discussed the basics of polarization selective spectroscopy and derived the expressions for polarization-associated spectra (PAS). We also gave an example to show how PAS are able to isolate spectroscopic signatures in a trial system. Two application cases can be found in our publications, which are summarized in the next chapter.

4. PUBLICATIONS

All research articles serving as the basis for this publication-based thesis are summarized in this chapter. The individual contributions of each author are clearly stated. Reprints of the original articles and supporting information are provided in the Appendix B and C, with permission of the respective journal.

4.1. Isolating Pure Donor and Acceptor Signals by Polarization-Controlled Transient Absorption Spectroscopy

Yi Xu, Lars Mewes, Erling Thyrhaug, Vladislav Sláma, František Šanda, Heinz Langhals and Jürgen Hauer

The Journal of Physical Chemistry Letters 2023, 14, 23, 5390–5396

DOI: 10.1021/acs.jpclett.3c01451

4.1.1. Summary and Classification within the Thesis

In this paper, we apply the PAS method to decompose the time-resolved optical spectra of a molecular donor-acceptor (D-A) dyad. The D-A dyad features an orthogonal arrangement of the donor (D) and acceptor (A) moieties which suggest inefficient excitation energy transfer according to Förster theory. Nevertheless, in experimental studies carried out on similar ortho-FRET systems, EET takes place within a few picoseconds.[27, 92-94] This inconsistency in the simple Förster picture has inspired a wealth of competing theories, including thermally induced deviations from a strictly orthogonal molecular geometry,[27] non-Condon effects (excited state reorganization),[95] or low-frequency anharmonic structural motion.[96] In this work we add further aspects to this debate by experimental insight provided by polarization-controlled TA spectroscopy. We show that the decomposition of the TA data into PAS lets us ascribe spectral species and decay times to either donor- or acceptor moieties. We support our analysis of D-A with data from the isolated donor molecule in solution using the same methodology.

We showed that polarization-controlled TA spectroscopy in a D-A system with orthogonal TDMs allows for an intuitive and clear assignment of spectral species from GLA. At an optimal angle $\beta \sim 30°$, we retrieve pure donor and acceptor spectra in S_{z-30° and S_{y-30°, respectively. In essence, PAS transient spectra successfully disentangle the overlapping spectral signatures of different steps in an EET process. Our polarization-based measurements support the existence of significant geometric/dipole fluctuations in ortho-FRET dyads, supplementing the previous indirect evidence based on the Förster theory of EET.[96] The approach for disentangling TAA-dynamics as described in our work provides new impulses for the description of dipole fluctuations and helps to distinguish between competing theories.[95, 97] As demonstrated in the analysis of the isolated donor molecule D, the method presented here benefits from but is not limited to systems with orthogonally arranged TDMs.

4.1.2. INDIVIDUAL CONTRIBUTIONS

The presented experimental data was recorded and analyzed by Y. Xu under the guidance of L. Mewes, E. Thyrhaug, and J. Hauer. The theoretical work was done by V. Sláma and F. Šanda. The sample was provided by H. Langhals. The manuscript and supporting information were written by Y. Xu and edited by L. Mewes, V. Sláma, E. Thyrhaug, F. Šanda, H. Langhals and J. Hauer. All figures were created by Y. Xu.

4.2. DETERMINING EXCITED STATE ABSORPTION PROPERTIES OF A QUINOID FLAVIN BY POLARIZATION-RESOLVED TRANSIENT SPECTROSCOPY

Yi Xu, Martin T. Peschel, Miriam Jänchen, Richard Foja, Golo Storch, Erling Thyrhaug, Regina de Vivie-Riedle and Jürgen Hauer*

The Journal of Physical Chemistry A 2024, 128, 19, 3830–3839

DOI: 10.1021/acs.jpca.4c01260

4.2.1. SUMMARY AND CLASSIFICATION WITHIN THE THESIS

Flavins are important naturally occurring chromophores; their photo-physical properties have been extensively studied both experimentally and theoretically.[98] However, little is known about the TDM orientation of ESA transitions of these important compounds. This aspect is of great interest in the field of photocatalysis since the triplet yield can be further enhanced via re-excitation of the initially excited singlet state.[47-49] Knowing the orientation of ESA-TDMs with respect to the GSB-TDM will allow for a more efficient re-excitation process. In this study, we investigate the transient TDM-directions of a quinoid flavin derivative (3,10-dibutylbenzo[g]pteridine-2,4(3H,10H)-dione). The absorption spectrum of flavin features two broad bands with peaks at 440 nm ($S_0 \rightarrow S_1$) and 330 nm ($S_0 \rightarrow S_3$). We choose 400 nm and 325 nm pump pulses to selectively excite the two absorption bands. The TAS of the flavin shows three distinct ESA bands: sub-400 nm, at 478 nm, and above 600 nm. We refer to these as UV-ESA, blue-ESA, and red-ESA in the following but exclude the UV-ESA from further discussion.

By calculating the PAS, we determine the angle between the $S_1 \rightarrow S_0$ and $S_0 \rightarrow S_3$ TDMs to be 13°, which is consistent with results from fluorescence excitation anisotropy. Due to the vibronic coupling of the optically dark $S_0 \rightarrow S_2$ transition,[99] the DH-TDDFT calculated angle for the $S_1 \rightarrow S_0$ TDM deviates by 20° from the experimental result. Besides this discrepancy, we find the experimentally determined and calculated angles between the TDMs for $S_1 \rightarrow S_0$ (SE) and $S_1 \rightarrow S_8$ (red-ESA), $S_0 \rightarrow S_3$ and $S_1 \rightarrow S_0$ (SE) as well as $S_0 \rightarrow S_3$ and $S_1 \rightarrow S_8$ to agree well. The

$S_1 \rightarrow S_{11}$ (blue-ESA) transition however shows a ~ 20° mismatch between experiment and theory. We attribute this to the presence of dark states and the high energy of ~ 4.92 eV (39 683 cm^{-1}) of the S_{11} state. In summary, we have shown that the employed level of theory shows satisfactory agreement with measured TA spectra at MA orientation. Only when analyzing the relative orientation of TDMs, do we find discrepancies between experiment and theory, attributable to, *e.g.*, vibronic coupling. Hence, we have shown that polarization-controlled spectroscopy is an insightful method to benchmark quantum chemical methods for electronic excited states.

4.2.2. INDIVIDUAL CONTRIBUTIONS

The measurement set-up was modified by Y. Xu and M. Jänchen. The TA experimental data was recorded and analyzed by Y. Xu under the guidance of E. Thyrhaug and J. Hauer. Y. Xu derived all analytical results. The steady spectra and fluorescence lifetime were recorded by M. Jänchen. The theoretical work was done by M. T. Peschel and R. de Vivie-Riedle. The sample was provided by R. Foja and G. Storch. The manuscript and supporting information were written by Y. Xu and edited by M. T. Peschel, R. Foja, E. Thyrhaug, R. de Vivie-Riedle, and J. Hauer. All figures were created by Y. Xu except Figure 2 and Figure 3 created by M. T. Peschel.

5. CONCLUSION AND OUTLOOK

In this thesis, we developed the concept and methodology of PAS. This strategy not only provides information about the TDMs but also enables the reduction of spectral congestion in complex systems. This allows for detailed studies of electronic structure and energy transfer. Based on the two isotropic tensor components of a TAA signal,[87, 100-101] PAS are calculated by using suitable linear combinations of parallel and orthogonal spectra. PAS express the signal in terms of components in the molecular frame and thus bring better insight into the relative orientation of molecular TDMs. This approach meaningfully separates the isotropic spectrum into linearly independent components, and thus highly simplifies the experimental data. Furthermore, we can rotate the coordinate system to determine the orientation of molecular TDMs.

We applied the PAS strategy to a perylene-based energy transfer dyad system consisting of donor (D) and acceptor (A) moieties with orthogonal TDMs. We separated the TAS-data of the dyad into the pure D- and A-parts of the total signal, greatly reducing spectral congestion in complex systems and thus allowing for detailed studies of electronic structure and electronic energy transfer. Our study also supports the existence of significant geometric/dipole fluctuations in ortho-FRET dyads, supplementing the previous indirect evidence based on Förster theory of EET.[96]

We also applied PAS on the quinoid flavin to determine the orientation of TDMs connecting electronic excited states. We isolate pure ESA signals from ground-state bleach (GSB) and stimulated emission (SE). By comparing to more conventional methods of extracting pure ESA signals, we highlight the advantages of our approach. Furthermore, we determine the relative angle between the TDMs of two neighboring ESA transitions. Our study highlights the influence of vibronic coupling, which would have remained hidden in conventional transient absorption spectroscopy. This makes polarization-controlled spectroscopy an insightful method to benchmark the prediction of TDM-directions by quantum chemical methods for electronic excited states. On a broader scope, our findings have the potential to facilitate and inspire advanced photocatalytic strategies, in which the re-excitation of excited states increases the catalyst's redox potential.[102]

In future work, we plan to explore more applications of PAS to study more photocatalytic systems. To drive challenging reactions, the photocatalysis community designed reactions that overcome thermodynamic barriers by combining the energy of two or more excitation events.[103-104] Instead of using UV light, two or more separate excitations in the visible or even the NIR can be used to reach higher-lying states without photodamage and avoid undesired side reactions, as illustrated in Figure 5.1. For this purpose, knowing the TDMs orientation of excited state transitions is of great importance, *e.g.*, to achieve higher quantum yield by setting the right polarization of each light beam. Furthermore, PAS can be also used to describe states that are optically dark from the ground state, for example in carotenoids.[105] This makes PAS relevant in photosynthetic research.

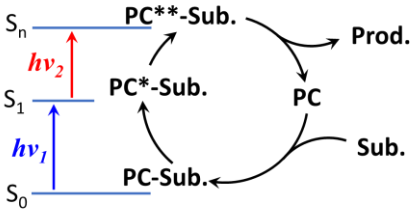

Figure 5.1 Simplified photocatalysis reaction circle with two consecutive photon excitations. PC denotes photocatalyst. The PC** (higher-lying state, S$_n$) is obtained by re-exciting the PC* (S$_1$ state). Sub. and Prod. denotes the substate and product respectively, PC-Sub. means the complex of the photocatalyst and substrate.

In this thesis, all the polarization-controlled TA measurements are done by sequentially changing the polarization of the pump pulse. This procedure is not ideal as it will introduce instability during the measurement, due to fluctuation of the laser. Simultaneous measurement of the parallel and perpendicular TA spectra is hence desirable. In the future, we will implement a single-shot TAA set-up that can obtain the parallel and perpendicular TA data simultaneously. Instead of setting the probe beam vertically, we use a 45° polarized probe pulse and split it after the sample by using a broadband polarizing beam splitter into the horizontal and vertical components (the pump will be set vertically). The probe beam's components can hence be monitored by two detectors simultaneously. See Figure 5.2. The inspiration is from Galli et. al.

and Min et. al.'s reports, who designed the single-shot TAA set-up with monochromatic excitation and detection.[17, 106] We can expand this design to broadband detection.

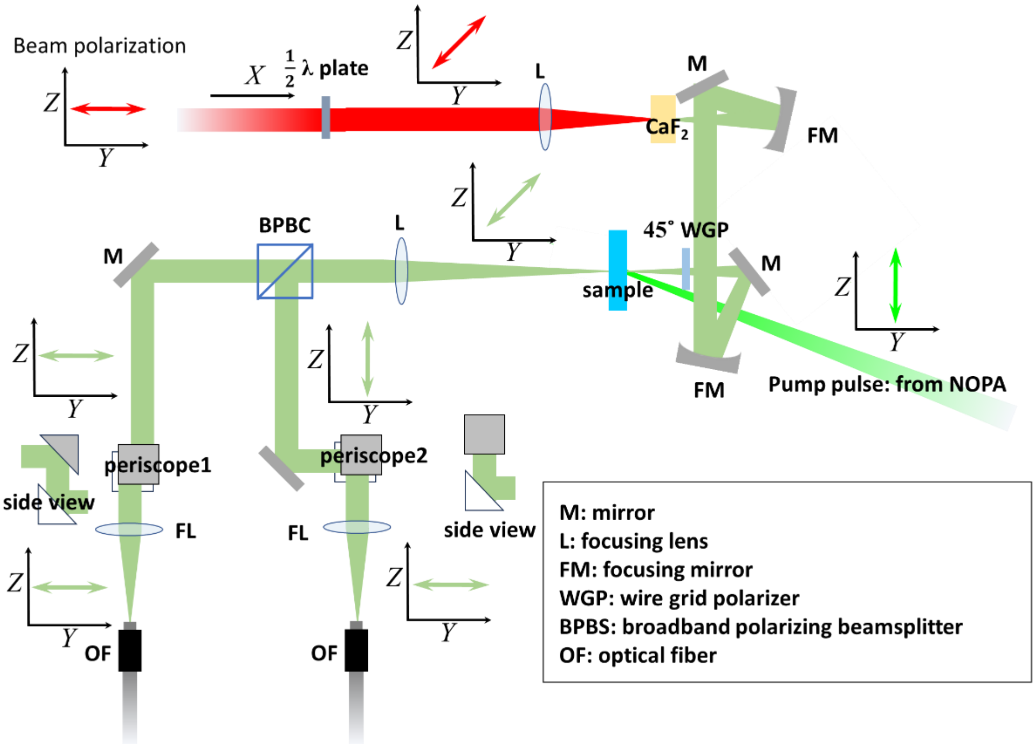

Figure 5.2 The broadband single-shot transient absorption anisotropy set-up. The white light is set 45° to the vertical by i) seeding the translating CaF$_2$ with a 45° polarized fundamental pulse and ii) putting a 45° oriented wired grid polarizer before the sample to keep the polarization. After the sample, the white light is split by a broadband polarizer splitter cube. After the polarizer, two periscopes are used to keep the polarizations of the two parts of probe pulses consistently the same before sending them to the fiber.

BIBLIOGRAPHY

(1) Goldemberg, J.; Johansson, T. B.; Coelho, S. T., World energy assessment: overview: 2004 update. **2004**.

(2) Lewis, N. S., Toward cost-effective solar energy use. *Science* **2007,** *315* (5813), 798-801.

(3) Malato, S.; Blanco, J.; Vidal, A.; Richter, C., Photocatalysis with solar energy at a pilot-plant scale: an overview. *Appl. Catal., B* **2002,** *37* (1), 1-15.

(4) Esswein, A. J.; Nocera, D. G., Hydrogen production by molecular photocatalysis. *Chem. Rev.* **2007,** *107* (10), 4022-4047.

(5) Miyake, G. M.; Theriot, J. C., Perylene as an organic photocatalyst for the radical polymerization of functionalized vinyl monomers through oxidative quenching with alkyl bromides and visible light. *Macromolecules* **2014,** *47* (23), 8255-8261.

(6) König, B.; Kümmel, S.; Svobodová, E.; Cibulka, R., Flavin photocatalysis. *Phys. Sci. Rev.* **2018,** *3* (8), 20170168.

(7) Ameta, R.; Solanki, M. S.; Benjamin, S.; Ameta, S. C., Photocatalysis. In *Advanced oxidation processes for waste water treatment*, Elsevier: 2018; pp 135-175.

(8) Zhao, X.; Hou, Y.; Liu, L.; Zhao, J., Triplet photosensitizers showing strong absorption of visible light and long-lived triplet excited states and application in photocatalysis: A mini review. *Energy Fuels* **2021,** *35* (23), 18942-18956.

(9) Blankenship, R. E., *Molecular mechanisms of photosynthesis*. John Wiley & Sons: 2021.

(10) Kumpulainen, T.; Lang, B.; Rosspeintner, A.; Vauthey, E., Ultrafast elementary photochemical processes of organic molecules in liquid solution. *Chem. Rev.* **2017,** *117* (16), 10826-10939.

(11) Rosspeintner, A.; Lang, B.; Vauthey, E., Ultrafast photochemistry in liquids. *Annu. Rev. Phys. Chem* **2013,** *64* (1), 247-271.

(12) Förster, T., Transfer mechanisms of electronic excitation energy. *Radiat. Res. Suppl.* **1960**, 326-339.

(13) Förster, T., Zwischenmolekulare energiewanderung und fluoreszenz. *Ann. Phys.* **1948,** *437* (1-2), 55-75.

(14) Zewail, A. H., Femtochemistry: atomic-scale dynamics of the chemical bond using ultrafast lasers (Nobel Lecture). *Angew. Chem. Int. Ed.* **2000,** *39* (15), 2586-2631.

(15) Holzwarth, A. R., [14] Time-resolved fluorescence spectroscopy. *Methods Enzymol.* **1995,** *246*, 334-362.

(16) van Amerongen, H.; van Grondelle, R., [9] Transient absorption spectroscopy in study of processes and dynamics in biology. In *Methods Enzymol.*, Elsevier: 1995; Vol. 246, pp 201-226.

(17) Min, C.-K.; Joo, T.; Yoon, M.-C.; Kim, C. M.; Hwang, Y. N.; Kim, D.; Aratani, N.; Yoshida, N.; Osuka, A., Transient absorption anisotropy study of ultrafast energy transfer in porphyrin monomer, its direct meso–meso coupled dimer and trimer. *J. Chem. Phys.* **2001,** *114* (15), 6750-6758.

(18) Wallin, S.; Davidsson, J.; Modin, J.; Hammarström, L., Femtosecond transient absorption anisotropy study on [Ru (bpy) 3] 2+ and [Ru (bpy)(py) 4] 2+. Ultrafast interligand randomization of the MLCT state. *J. Phys. Chem. A* **2005,** *109* (21), 4697-4704.

(19) Albrecht, A. C., Polarizations and assignments of transitions: the method of photoselection. *J. Mol. Spectrosc.* **1961,** *6*, 84-108.

(20) Thyrhaug, E.; Sorensen, T. J.; Gryczynski, I.; Gryczynski, Z.; Laursen, B. W., Polarization and symmetry of electronic transitions in long fluorescence lifetime triangulenium dyes. *J. Phys. Chem. A* **2013,** *117* (10), 2160-8.

(21) Xu, Y.; Mewes, L.; Thyrhaug, E.; Sláma, V.; Šanda, F. e.; Langhals, H.; Hauer, J. r., Isolating Pure Donor and Acceptor Signals by Polarization-Controlled Transient Absorption Spectroscopy. *J. Phys. Chem. Lett.* **2023,** *14*, 5390-5396.

(22) Macedo, A. G.; Christopholi, L. P.; Gavim, A. E.; de Deus, J. F.; Teridi, M. A. M.; Yusoff, A.; bin Mohd, R.; da Silva, W. J., Perylene derivatives for solar cells and energy harvesting: a review of materials, challenges and advances. *J. Mater. Sci.: Mater. Electron.* **2019,** *30* (17), 15803-15824.

(23) Huang, T.; Lu, D.; Ma, L.; Xi, X.; Liu, R.; Wu, D., A hit-and-run strategy towards perylene diimide/reduced graphene oxide as high performance sodium ion battery cathode. *Chem. Eng. J.* **2018,** *349*, 66-71.

(24) Häupler, B.; Wild, A.; Schubert, U. S., Carbonyls: powerful organic materials for secondary batteries. *Adv. Energy Mater.* **2015,** *5* (11), 1402034.

(25) Langhals, H., Farbstoffe für Fluoreszenz-Solarkollektoren. *Nachr. Chem. Tech. Lab.* **1980**, 716-718.

(26) Langhals, H., Control of the interactions in multichromophores: novel concepts. Perylene bis-imides as components for larger functional units. *Helv. Chim. Acta* **2005,** *88* (6), 1309-1343.

(27) Langhals, H.; Esterbauer, A. J.; Walter, A.; Riedle, E.; Pugliesi, I., Förster resonant energy transfer in orthogonally arranged chromophores. *J. Am. Chem. Soc.* **2010,** *132* (47), 16777-16782.

(28) Sebastian, E.; Hariharan, M., Null Exciton-Coupled Chromophoric Dimer Exhibits Symmetry-Breaking Charge Separation. *J. Am. Chem. Soc.* **2021,** *143* (34), 13769-13781.

(29) Li, C.; Wonneberger, H., Perylene imides for organic photovoltaics: yesterday, today, and tomorrow. *Adv. Mater.* **2012,** *24* (5), 613-636.

(30) Avlasevich, Y.; Li, C.; Müllen, K., Synthesis and applications of core-enlarged perylene dyes. *J. Mater. Chem.* **2010,** *20* (19), 3814-3826.

(31) Brown, K. E.; Salamant, W. A.; Shoer, L. E.; Young, R. M.; Wasielewski, M. R., Direct observation of ultrafast excimer formation in covalent perylenediimide dimers using near-infrared transient absorption spectroscopy. *J. Phys.l Chem. Lett.* **2014,** *5* (15), 2588-2593.

(32) Kölle, P.; Pugliesi, I.; Langhals, H.; Wilcken, R.; Esterbauer, A. J.; de Vivie-Riedle, R.; Riedle, E., Hole-transfer induced energy transfer in perylene diimide dyads with a donor–spacer–acceptor motif. *Phys. Chem. Chem. Phys.* **2015,** *17* (38), 25061-25072.

(33) Christensen, R. L.; Drake, R. C.; Phillips, D., Time-resolved fluorescence anisotropy of perylene. *J. Phys. Chem.* **1986,** *90* (22), 5960-5967.

(34) Ambrosino, F.; Califano, S., The vibrational spectrum of perylene. *Spectrochim. Acta* **1965,** *21* (8), 1401-1409.

(35) Geng, T.-M.; Li, D.-K.; Zhu, Z.-M.; Zhang, W.-Y.; Ye, S.-N.; Zhu, H.; Wang, Z.-Q., Fluorescent conjugated microporous polymer based on perylene tetraanhydride bisimide for sensing o-nitrophenol. *Anal. Chim. Acta* **2018,** *1011*, 77-85.

(36) Liu, K.; Shang, C.; Wang, Z.; Qi, Y.; Miao, R.; Liu, K.; Liu, T.; Fang, Y., Non-contact identification and differentiation of illicit drugs using fluorescent films. *Nat. Commun.* **2018,** *9* (1), 1-11.

(37) Georgiev, N. I.; Said, A. I.; Toshkova, R. A.; Tzoneva, R. D.; Bojinov, V. B., A novel water-soluble perylenetetracarboxylic diimide as a fluorescent pH probe: chemosensing, biocompatibility and cell imaging. *Dyes Pigments* **2019,** *160*, 28-36.

(38) He, J.; Chen, H.; Guo, Y.; Wang, L.; Zhu, L.; Karahan, H. E.; Chen, Y., Polycondensation of a perylene bisimide derivative and L-malic acid as water-soluble conjugates for fluorescent labeling of live mammalian cells. *Polymers* **2018,** *10* (5), 559.

(39) Yao, Z.; Zhang, M.; Wu, H.; Yang, L.; Li, R.; Wang, P., Donor/acceptor indenoperylene dye for highly efficient organic dye-sensitized solar cells. *J. Am. Chem. Soc.* **2015,** *137* (11), 3799-3802.

(40) Romero, E.; Gómez Castellanos, J. R.; Gadda, G.; Fraaije, M. W.; Mattevi, A., Same substrate, many reactions: Oxygen activation in flavoenzymes. *Chem. Rev.* **2018,** *118* (4), 1742-1769.

(41) Macheroux, P.; Kappes, B.; Ealick, S. E., Flavogenomics–a genomic and structural view of flavin-dependent proteins. *FEBS J* **2011,** *278* (15), 2625-2634.

(42) Massey, V., The chemical and biological versatility of riboflavin. *Biochem. Soc. Trans.* **2000,** *28* (4), 283-296.

(43) Zhang, M.; Wang, L.; Shu, S.; Sancar, A.; Zhong, D., Bifurcating electron-transfer pathways in DNA photolyases determine the repair quantum yield. *Science* **2016,** *354* (6309), 209-213.

(44) Srivastava, V.; Singh, P. K.; Srivastava, A.; Singh, P. P., Synthetic applications of flavin photocatalysis: a review. *RSC Adv.* **2021,** *11* (23), 14251-14259.

(45) Martin, C. B.; Shi, X.; Tsao, M.-L.; Karweik, D.; Brooke, J.; Hadad, C. M.; Platz, M. S., The photochemistry of riboflavin tetraacetate and nucleosides. A study using density functional theory, laser flash photolysis, fluorescence, UV− vis, and time resolved infrared spectroscopy. *J. Phys. Chem. B* **2002,** *106* (39), 10263-10271.

(46) Salzmann, S.; Martinez-Junza, V.; Zorn, B. r.; Braslavsky, S. E.; Mansurova, M.; Marian, C. M.; Gärtner, W., Photophysical properties of structurally and electronically modified flavin derivatives determined by spectroscopy and theoretical calculations. *J. Phys. Chem. A* **2009,** *113* (33), 9365-9375.

(47) Rajagopal, S. K.; Mallia, A. R.; Hariharan, M., Enhanced intersystem crossing in carbonylpyrenes. *Phys. Chem. Chem. Phys.* **2017,** *19* (41), 28225-28231.

(48) Schmid, L.; Glaser, F.; Schaer, R.; Wenger, O. S., High triplet energy iridium (III) isocyanoborato complex for photochemical upconversion, photoredox and energy transfer catalysis. *J. Am. Chem. Soc.* **2022,** *144* (2), 963-976.

(49) Cai, X.; Hara, M.; Kawai, K.; Tojo, S.; Majima, T., Sensitized reactions by benzophenones in the higher triplet excited state. *Chem. Phys. Lett.* **2003,** *371* (1-2), 68-73.

(50) Kao, Y.-T.; Tan, C.; Song, S.-H.; Öztürk, N.; Li, J.; Wang, L.; Sancar, A.; Zhong, D., Ultrafast dynamics and anionic active states of the flavin cofactor in cryptochrome and photolyase. *J. Am. Chem. Soc.* **2008,** *130* (24), 7695-7701.

(51) Brazard, J.; Usman, A.; Lacombat, F.; Ley, C.; Martin, M. M.; Plaza, P., New insights into the ultrafast photophysics of oxidized and reduced FAD in solution. *J. Phys. Chem. A* **2011,** *115* (15), 3251-3262.

(52) Weigel, A.; Dobryakov, A. L.; Veiga, M.; Pérez Lustres, J. L., Photoinduced processes in riboflavin: Superposition of ππ*− nπ* states by vibronic coupling, transfer of vibrational coherence, and population dynamics under solvent control. *J. Phys. Chem. A* **2008,** *112* (47), 12054-12065.

(53) Turro, N. J.; Ramamurthy, V.; Scaiano, J. C., *Modern molecular photochemistry of organic molecules*. University Science Books Sausalito, CA: 2010; Vol. 188.

(54) Maiuri, M.; Garavelli, M.; Cerullo, G., Ultrafast spectroscopy: state of the art and open challenges. *J. Am. Chem. Soc.* **2019,** *142* (1), 3-15.

(55) Rodger, A., [10] Linear dichroism. *Methods Enzymol.* **1993,** *226*, 232-258.

(56) Megerle, U.; Pugliesi, I.; Schriever, C.; Sailer, C. F.; Riedle, E., Sub-50 fs broadband absorption spectroscopy with tunable excitation: putting the analysis of ultrafast molecular dynamics on solid ground. *Appl. Phys. B* **2009,** *96*, 215-231.

(57) Bradler, M.; Riedle, E., Temporal and spectral correlations in bulk continua and improved use in transient spectroscopy. *JOSA B* **2014,** *31* (7), 1465-1475.

(58) Riedle, E.; Beutter, M.; Lochbrunner, S.; Piel, J.; Schenkl, S.; Spörlein, S.; Zinth, W., Generation of 10 to 50 fs pulses tunable through all of the visible and the NIR. *Appl. Phys. B* **2000,** *71*, 457-465.

(59) Homann, C.; Schriever, C.; Baum, P.; Riedle, E., Octave wide tunable UV-pumped NOPA: pulses down to 20 fs at 0.5 MHz repetition rate. *Opt. Express* **2008,** *16* (8), 5746-5756.

(60) Lochbrunner, S.; Wilhelm, T.; Piel, J.; Sporlein, S.; Riedle, E. In *Sub-20-fs tunable pulses in the visible and NIR by noncollinear optical parametric amplification (NOPA)*, Advanced Solid State Lasers, Optica Publishing Group: 1999; p TuA4.

(61) Hecht, E., *Optics*. Pearson Education, Incorporated: 2017.

(62) Trebino, R., Frog. *Frequency-resolved optical gating: the measurement of ultrashort laser pulses* **2000**, 101-115.

(63) Knorr, F. c.; Harris, J., Resolution of multicomponent fluorescence spectra by an emission wavelength-decay time data matrix. *Anal. Chem.* **1981,** *53* (2), 272-276.

(64) Knutson, J. R.; Walbridge, D. G.; Brand, L., Decay-associated fluorescence spectra and the heterogeneous emission of alcohol dehydrogenase. *Biochemistry* **1982,** *21* (19), 4671-4679.

(65) Ruckebusch, C.; Sliwa, M.; Pernot, P. d.; De Juan, A.; Tauler, R., Comprehensive data analysis of femtosecond transient absorption spectra: A review. *J. Photochem. Photobiol. C* **2012,** *13* (1), 1-27.

(66) van Stokkum, I. H.; Larsen, D. S.; Van Grondelle, R., Global and target analysis of time-resolved spectra. *Biochim. Biophys. Acta, Bioenerg.* **2004,** *1657* (2-3), 82-104.

(67) Slavov, C.; Hartmann, H.; Wachtveitl, J., Implementation and evaluation of data analysis strategies for time-resolved optical spectroscopy. *Anal. Chem.* **2015,** *87* (4), 2328-2336.

(68) Kovalenko, S. A.; Dobryakov, A. L.; Ruthmann, J.; Ernsting, N. P., Femtosecond spectroscopy of condensed phases with chirped supercontinuum probing. *Phys. Rev. A* **1999,** *59* (3), 2369.

(69) Ekvall, K.; Van Der Meulen, P.; Dhollande, C.; Berg, L.-E.; Pommeret, S.; Naskrecki, R.; Mialocq, J.-C., Cross phase modulation artifact in liquid phase transient absorption spectroscopy. *J. Appl. Phys.* **2000,** *87* (5), 2340-2352.

(70) Lorenc, M.; Ziolek, M.; Naskrecki, R.; Karolczak, J.; Kubicki, J.; Maciejewski, A., Artifacts in femtosecond transient absorption spectroscopy. *Appl. Phys. B* **2002,** *74*, 19-27.

(71) Jabłoński, A., Über den mechanismus der photolumineszenz von farbstoffphosphoren. *Z. Phys.* **1935,** *94* (1-2), 38-46.

(72) Kliger, D. S.; Lewis, J. W., *Polarized light in optics and spectroscopy*. Elsevier: 2012.

(73) Dörr, F., Spectroscopy with polarized light. *Angew. Chem. (Int. Ed.)* **1966,** *5* (5), 478-495.

(74) Rodger, A.; Nordén, B., *Circular dichroism and linear dichroism*. Oxford University Press, USA: 1997; Vol. 1.

(75) Lakowicz, J. R., *Principles of fluorescence spectroscopy*. Springer: 2006.

(76) Bulheller, B. M.; Rodger, A.; Hirst, J. D., Circular and linear dichroism of proteins. *Phys. Chem. Chem. Phys.* **2007,** *9* (17), 2020-2035.

(77) Rodger, A., How to study DNA and proteins by linear dichroism spectroscopy. *Sci. Prog.* **2008,** *91* (4), 377-396.

(78) Nordén, B.; Kurucsev, T., Analysing DNA complexes by circular and linear dichroism. *J. Mol. Recogn.* **1994,** *7* (2), 141-155.

(79) Steiner, R. F., Fluorescence anisotropy: theory and applications. In *Topics in fluorescence spectroscopy: Principles*, Springer: 1991; pp 1-52.

(80) Ma, L.; Kuang, Z.; Wang, Z.; Zhao, H.; Wan, Y.; Zhang, X.-F.; Li, Y.; Xia, A., Ultrafast Charge Separation Driven by Torsional Motion in Orthogonal Boron Dipyrromethene Dimer. *J. Phys. Chem. Lett.* **2023,** *14*, 702-708.

(81) Dutier, G.; de Beaucoudrey, V.; Zyss, J.; Brasselet, S. In *Photo-induced rotation of single molecules*, Physical Chemistry of Interfaces and Nanomaterials IV, SPIE: 2005; pp 104-111.

(82) Schalk, O.; Unterreiner, A. N., The influence of rotational diffusion on transient anisotropy in ultrafast experiments. *Phys. Chem. Chem. Phys.* **2010,** *12* (3), 655-666.

(83) Wan, C.; Johnson, C. K., Time-resolved two-photon induced anisotropy decay: The rotational diffusion regime. *J. Chem. Phys.* **1994,** *101* (12), 10283-10291.

(84) Thulstrup, E. W.; Eggers, J., Moment directions of the electronic transitions of fluoranthene. *Chem. Phys. Lett.* **1968,** *1* (13), 690-692.

(85) Michl, J.; Thulstrup, E. W., Ultraviolet and infrared linear dichroism: polarized light as a probe of molecular and electronic structure. *Acc. Chem. Res.* **1987,** *20* (5), 192-199.

(86) Thulstrup, E. W.; Michl, J., Polarized absorption spectroscopy of molecules aligned in stretched polymers bl. *Spectrochim. Acta A Mol. Spectrosc.* **1988,** *44* (8), 767-782.

(87) Andrews, D. L.; Thirunamachandran, T., On three-dimensional rotational averages. *J. Chem. Phys.* **1977,** *67* (11), 5026-5033.

(88) Andrews, D. L.; Blake, N. P., Three-dimensional rotational averages in radiation-molecule interactions: an irreducible cartesian tensor formulation. *J. Phys. A: Math. Gen.* **1989,** *22* (1), 49.

(89) Bonvicini, A.; Champagne, B., Three-Dimensional Rotational Averaging Using Irreducible Sets of Linearly Independent Fundamental Isotropic Cartesian Tensors: A Computational Approach. *J. Chem. Theory Comput.* **2023,** *19* (21), 7801-7815.

(90) Albrecht, A. C.; Simpson, W. T., Spectroscopic Study of Wurster's Blue and Tetramethyl-p-phenylenediamine with Assignments of Electronic Transitions1. *J. Am. Chem. Soc.* **1955,** *77* (17), 4454-4461.

(91) Thyrhaug, E.; Zidek, K.; Dostal, J.; Bina, D.; Zigmantas, D., Exciton Structure and Energy Transfer in the Fenna-Matthews-Olson Complex. *J. Phys. Chem. Lett.* **2016,** *7* (9), 1653-60.

(92) Langhals, H.; Walter, A., FRET in dyads with orthogonal chromophores and minimal spectral overlap. *J. Phys. Chem. A* **2020,** *124* (8), 1554-1560.

(93) Langhals, H.; Poxleitner, S.; Krotz, O.; Pust, T.; Walter, A., FRET in orthogonally arranged chromophores. *Eur. J. Org. Chem.* **2008**, 4559–4562.

(94) Langhals, H.; Dietl, C., Vibronic Intramolecular Resonant Energy Transfer along More than 5 nm: Synthesis of Dyads for a Re-Examination of the Distance Function of FRET. *J. Org. Chem.* **2022**.

(95) Renger, T.; Dankl, M.; Klinger, A.; Schlucker, T.; Langhals, H.; Muh, F., Structure-Based Theory of Fluctuation-Induced Energy Transfer in a Molecular Dyad. *J. Phys. Chem. Lett.* **2018,** *9* (20), 5940-5947.

(96) Slama, V.; Perlik, V.; Langhals, H.; Walter, A.; Mancal, T.; Hauer, J.; Sanda, F., Anharmonic Molecular Motion Drives Resonance Energy Transfer in peri-Arylene Dyads. *Front. chem.* **2020,** *8*, 579166.

(97) Nalbach, P.; Pugliesi, I.; Langhals, H.; Thorwart, M., Noise-induced Förster resonant energy transfer between orthogonal dipoles in photoexcited molecules. *Phys. Rev. Lett.* **2012,** *108* (21), 218302.

(98) Sun, M.; Moore, T., Molecular Luminescence Studies of Flavins. I. The Excited States of Flavins. *J. Amer. Chem. Soc* **1972,** *94* (5), 17301740.

(99) Weigel, A.; Dobryakov, A.; Klaumunzer, B.; Sajadi, M.; Saalfrank, P.; Ernsting, N., Femtosecond stimulated Raman spectroscopy of flavin after optical excitation. *J. Phys. Chem. B* **2011,** *115* (13), 3656-3680.

(100) Weyl, H., *The classical groups: their invariants and representations*. Princeton university press: 1946.

(101) Jeffreys, H. In *On isotropic tensors*, Mathematical Proceedings of the Cambridge philosophical society, Cambridge University Press: 1973; pp 173-176.

(102) McGimpsey, W. C.; Scaiano, J. C., Photoexcitation of benzophenone triplets: a two-photon pathway for ground state repopulation. *Chem. Phys. Lett.* **1987,** *138* (1), 13-17.

(103) Glaser, F.; Kerzig, C.; Wenger, O. S., Multi-photon excitation in photoredox catalysis: concepts, applications, methods. *Angew. Chem. Int. Ed.* **2020,** *59* (26), 10266-10284.

(104) Goez, M.; Hussein, B. H. M., Photoionization of xanthone via its triplet state or via its radical anion. *Phys. Chem. Chem. Phys.* **2004,** *6* (24), 5490-5497.

(105) Šebelík, V.; Duffy, C. D.; Keil, E.; Polívka, T.; Hauer, J., Understanding carotenoid dynamics via the vibronic energy relaxation approach. *J. Phys. Chem. B* **2022,** *126* (22), 3985-3994.

(106) Galli, C.; Wynne, K.; LeCours, S. M.; Therien, M.; Hochstrasser, R., Direct measurement of electronic dephasing using anisotropy. *Chem. Phys. Lett.* **1993,** *206* (5-6), 493-499.

APPENDIX

A. SUPPLEMENTARY INFORMATION FOR CHAPTER 3.3

- **Three-Dimensional Averaging**

To quantify the response of isotropic samples to polarized light, rotational averaging is necessary. As mentioned in Chapter 3.3 we have two Cartesian frames: the laboratory and molecular Cartesian frames. We introduced the laboratory axes X, Y, and Z, and the molecular axes, x, y, and z, as indicated in Figure A.1. It is convenient to specify the direction cosines in terms of Euler angles.[107-108] We write rotations in terms of rotation matrices $\boldsymbol{D}$, $\boldsymbol{C}$, and $\boldsymbol{B}$, then a general rotation $\boldsymbol{A}$ which is the product of the successive matrices,

$$\boldsymbol{A} = \boldsymbol{BCD} = \begin{pmatrix} cos\psi & sin\psi & 0 \\ -sin\psi & cos\psi & 0 \\ 0 & 0 & 1 \end{pmatrix} \cdot \begin{pmatrix} 1 & 0 & 0 \\ 0 & cos\theta & sin\theta \\ 0 & -sin\theta & cos\theta \end{pmatrix} \cdot \begin{pmatrix} cos\varphi & sin\varphi & 0 \\ -sin\varphi & cos\varphi & 0 \\ 0 & 0 & 1 \end{pmatrix} \qquad eq.\ \text{A-1}$$

The $\boldsymbol{D}$ transformation is the first rotation by an angle φ about the $\boldsymbol{z}$-axis, The $\boldsymbol{C}$ transformation corresponds to a rotation by an angle θ about the former $\boldsymbol{x}$-axis. Finally, $\boldsymbol{B}$ is a rotation by an angle ψ about the former z-axis and therefore has the same form as $\boldsymbol{D}$. φ, θ, ψ are called Euler angles. The valid ranges of them are $0 \leq \varphi \leq 2\pi$, $0 \leq \theta \leq \pi$, and $0 \leq \psi \leq 2\pi$, as illustrated in Figure A.1.

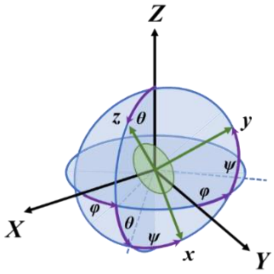

Figure A.1 laboratory axes, (X, Y, and Z), in black, and the molecular axes, (x, y, and z), in dark green, Cartesian frames. The relative orientations of these two Cartesian frames are defined through the Euler angles φ, θ, and ψ.[89, 108]

The expressions for the rotationally invariant observables associated with a given spectroscopic process can be derived by using the rotational averaging of Cartesian tensors,[89] which is expressed as,

$$\boldsymbol{S}^{(n)} = \langle l_{i_1\lambda_1} \ldots l_{i_n\lambda_n} \rangle = \frac{1}{8\pi^2}\int_0^{2\pi} d\psi \int_0^{2\pi} d\varphi \int_0^{\pi} l_{i_1\lambda_1} \ldots l_{i_n\lambda_n} \sin\theta \, d\theta \qquad eq.\text{ A-2}$$

Where the indices i_1,..., i_n, refer to the (X, Y, and Z) axes of the laboratory and indices, λ_1... λ_n, refer to the (x, y, and z) axes of the molecular frame. Each term in this direction cosines product, $l_{i_p\lambda_p}$, is the ($i_p\lambda_p$) element of the Euler angle matrix.

- **Cartesian Tensors of Rank 4**

TAS is, in essence, a four-wave mixing (4WM) process, we can express the signal as a four-point correlation function.[109]

$$\boldsymbol{S}^{(n)} = \langle(\hat{\mu}_\alpha \cdot \hat{E}_a)(\hat{\mu}_\beta \cdot \hat{E}_b)(\hat{\mu}_\gamma \cdot \hat{E}_c)(\hat{\mu}_\delta \cdot \hat{E}_d)\rangle\langle\mu_\alpha\mu_\beta\mu_\gamma\mu_\delta\rangle E_a E_b E_c E_d \qquad eq.\text{ A-3}$$

where $\hat{\mu}_\lambda$ and μ_λ ($\lambda = \alpha,\ \beta,\ \gamma$, and δ) are the magnitude and direction of the TDMs, respectively. $\hat{E}_i$ and E_i ($i = a,\ b,\ c$, and d) are the magnitude and direction of the $\boldsymbol{E}$-field (here we use hats to represent unit vectors, not operators). Since all the magnitudes are scalar, we will drop them in the later text. Considering the rotational average for Cartesian tensors of rank 4,[87-89] we have,

$$\begin{aligned} S^{(4)} &= \langle(\hat{\mu}_\alpha \cdot \hat{E}_a)(\hat{\mu}_\beta \cdot \hat{E}_b)(\hat{\mu}_\gamma \cdot \hat{E}_c)(\hat{\mu}_\delta \cdot \hat{E}_d)\rangle \qquad eq.\text{ A-4} \\ &= \frac{1}{30}\begin{pmatrix} (\hat{E}_a \cdot \hat{E}_b)(\hat{E}_c \cdot \hat{E}_d) \\ (\hat{E}_a \cdot \hat{E}_c)(\hat{E}_b \cdot \hat{E}_d) \\ (\hat{E}_a \cdot \hat{E}_d)(\hat{E}_b \cdot \hat{E}_c) \end{pmatrix}^T \begin{pmatrix} 4 & -1 & -1 \\ -1 & 4 & -1 \\ -1 & -1 & 4 \end{pmatrix} \begin{pmatrix} (\hat{\mu}_\alpha \cdot \hat{\mu}_\beta)(\hat{\mu}_\gamma \cdot \hat{\mu}_\delta) \\ (\hat{\mu}_\alpha \cdot \hat{\mu}_\gamma)(\hat{\mu}_\beta \cdot \hat{\mu}_\delta) \\ (\hat{\mu}_\alpha \cdot \hat{\mu}_\delta)(\hat{\mu}_\beta \cdot \hat{\mu}_\gamma) \end{pmatrix} \\ &= P^T M D \end{aligned}$$

As all the $\boldsymbol{E}$-fields and TDMs have a fixed relationship to each other, $\hat{E}_i$ and $\hat{\mu}_\lambda$ only represent unit vectors, we can simply write $\hat{E}_{i_1} \cdot \hat{E}_{i_2} = cos\theta_{i_1 i_2}$ and $\hat{\mu}_{\lambda_1} \cdot \hat{\mu}_{\lambda_2} = cos\theta_{\lambda_1\lambda_2}$, the θ represents the angle between the polarization of $\boldsymbol{E}$-fields ($\theta_{i_1 i_2}$) or between TDMs ($\theta_{\lambda_1\lambda_2}$). In 2D experiments, polarization conditions the of pulses sequence can be set to any arbitrary combination. If we only set the pump and probe pulses parallelly or perpendicularly, we can have 4 combinations of the polarization conditions of the pulse sequence: $ZZZZ$, $ZZYY$, $ZYZY$, and $ZYYZ$, where ZY-plane is orthogonal to the direction of light propagation X. In TA experiment, the first and second responses are the same, we only have $ZZZZ$ and $ZZYY$, Hence

$\hat{E}_a = \hat{E}_b$ and $\hat{E}_c = \hat{E}_d$. When the bandwidth of the pump pulse is narrow, the TDMs $\hat{\mu}_\alpha = \hat{\mu}_\beta$ and $\hat{\mu}_\gamma = \hat{\mu}_\delta$. Then *eq.* A-3 can be reduced to

$$\boldsymbol{S}^{(4)} = \langle (\hat{\mu}_\alpha \cdot \hat{E}_a)^2 (\hat{\mu}_\gamma \cdot \hat{E}_c)^2 \rangle \qquad eq.\text{ A-5}$$

$$= \frac{1}{30}\begin{pmatrix} \hat{E}_a{}^2 \cdot \hat{E}_c{}^2 \\ (\hat{E}_a \cdot \hat{E}_c)^2 \\ (\hat{E}_a \cdot \hat{E}_c)^2 \end{pmatrix}^T \begin{pmatrix} 4 & -1 & -1 \\ -1 & 4 & -1 \\ -1 & -1 & 4 \end{pmatrix} \begin{pmatrix} 1 \\ cos^2\theta_{\alpha\gamma} \\ cos^2\theta_{\alpha\gamma} \end{pmatrix} = \boldsymbol{P}^T\boldsymbol{MD}$$

For the measurement with $ZZZZ$ pulse sequence, in which $\hat{E}_a \cdot \hat{E}_c = 1$, we get from *eq.* A-5:

$$S_{ZZZZ} = \frac{2cos^2\theta_{\alpha\gamma} + 1}{15} \qquad eq.\text{ A-6}$$

θ represents the angle between the pumped and probed TDMs. The same holds for the $ZZYY$ pulse sequence, in which $\hat{E}_a \cdot \hat{E}_c = 0$. We obtain:

$$S_{ZZYY} = \frac{2 - cos^2\theta_{\alpha\gamma}}{15} \qquad eq.\text{ A-7}$$

We can calculate the anisotropy r and retrieve *eq.* 3-5:

$$r = \frac{S_{ZZZZ} - S_{ZZYY}}{S_{ZZZZ} + 2 \cdot S_{ZZYY}} = \frac{3cos^2\theta_{\alpha\gamma} - 1}{5} \qquad eq.\text{ A-8}$$

- **Pre-factor calculation**

In *eq.* A-5 we connected the molecular frame signals and the laboratory frame signals. In Chapter 3.3 we defined the absorption profanities along each direction r_x, r_y, and r_z, and the probability for the detection along each direction q_x, q_y, and q_z. Here we have combinations of the products of all r and q, see Table A-1. The signals along laboratory axes X, Y, and Z which can be experimentally measured, are the combination of the terms in Table A-1.

Table A-1 All the combinations of products of the absorption probabilities (r_x, r_y, and r_z,) and transition probabilities of excited states (q_x, q_y, and q_z) happen along each direction.

	r_x	r_{xy}	r_z
q_x	r_xq_x	r_yq_x	r_zq_x
q_y	r_xq_y	r_yq_y	r_yq_z
q_z	r_xq_z	r_zq_y	r_zq_z

The pre-factors for the products are encoded in $eq.$ A-5. We are now aiming to determine them.

We start with the $ZZZZ$ configuration, in which all the $\boldsymbol{E}$-fields are parallel. The $\boldsymbol{P}$ vector in eq. A-4 is

$$\boldsymbol{P}_{zzzz} = \begin{pmatrix} 1 & 1 & 1 \end{pmatrix} \qquad eq.\ \text{A-9}$$

In the case of $r_x q_x$, $r_y q_y$, and $r_z q_z$, we assume the axes coordinate origin of absorption and emission (or detected) TDMs to be the same. We have the $\boldsymbol{D}$ vector in $eq.$ A-5,

$$\boldsymbol{D} = \begin{pmatrix} 1 \\ 1 \\ 1 \end{pmatrix} \qquad eq.\ \text{A-10}$$

After insertion into $eq.$ A-5, we can determine the prefactors of $r_x q_x$, $r_y q_y$, and $r_z q_z$ for $ZZZZ$ to be $\frac{1}{5}$. Similarly, we can calculate the other terms in which r and q are orthogonal with each other. In this case

$$\boldsymbol{D} = \begin{pmatrix} 1 \\ 0 \\ 0 \end{pmatrix} \qquad eq.\ \text{A-11}$$

the pre-factors for the orthogonal terms are $\frac{1}{15}$. Similar procedures can be applied for $the\ ZZYY$ condition, in this case.

$$\boldsymbol{P}_{ZZYY} = \begin{pmatrix} 1 & 0 & 0 \end{pmatrix} \qquad eq.\ \text{A-12}$$

Here we list all the prefactors in Table A-2.

Table A-2 The prefactors for all r and q combinations at $ZZZZ$ and $ZZYY$ configurations.

	$r_x q_x$	$r_x q_y$	$r_x q_z$	$r_y q_y$	$r_y q_x$	$r_z q_x$	$r_z q_z$	$r_z q_y$	$r_z q_z$
$ZZZZ$	$\frac{1}{5}$	$\frac{1}{15}$	$\frac{1}{15}$	$\frac{1}{5}$	$\frac{1}{15}$	$\frac{1}{15}$	$\frac{1}{5}$	$\frac{1}{15}$	$\frac{1}{15}$
$ZZYY$	$\frac{1}{15}$	$\frac{2}{15}$	$\frac{2}{15}$	$\frac{1}{15}$	$\frac{2}{15}$	$\frac{2}{15}$	$\frac{1}{15}$	$\frac{2}{15}$	$\frac{2}{15}$

As we have all the prefactors, the intensity of detected signals polarized along the laboratory axes I_Z and I_Y can be expressed by the suitable combinations of the elements in Table A-1, as $eq.$ 3-8.

Bibliography for Appendix A

(87) Andrews, D. L.; Thirunamachandran, T., On three-dimensional rotational averages. *J. Chem. Phys.* **1977,** *67* (11), 5026-5033.

(88) Andrews, D. L.; Blake, N. P., Three-dimensional rotational averages in radiation-molecule interactions: an irreducible cartesian tensor formulation. *J. Phys. A: Math. Gen.* **1989,** *22* (1), 49.

(89) Bonvicini, A.; Champagne, B., Three-Dimensional Rotational Averaging Using Irreducible Sets of Linearly Independent Fundamental Isotropic Cartesian Tensors: A Computational Approach. *J. Chem. Theory Comput.* **2023,** *19* (21), 7801-7815.

(107) Euler, L., Novi commentarii academiae scientiarum petropolitanae. *Nr* **1776,** *20*, 189-207.

(108) Goldstein, H., *Classical mechanics*. Pearson Education India: 2011.

(109) Hamm, P.; Zanni, M., *Concepts and methods of 2D infrared spectroscopy*. Cambridge University Press: 2011.

B. FULL LENGTH ARTICLE OF SECTION 4.1

Reprinted with permission from Xu, Y.; Mewes, L.; Thyrhaug, E.; Sláma, V.; Šanda, F.; Langhals, H.; Hauer, J., Isolating pure donor and acceptor signals by polarization-controlled transient absorption spectroscopy. *J. Phys. Chem. Lett.* **2023,** *14*, 5390-5396.@ 2023 American Chemical Society.

The Supporting information is available free of charge, thus no reprint permission is necessary.

THE JOURNAL OF
PHYSICAL CHEMISTRY
LETTERS
A JOURNAL OF THE AMERICAN CHEMICAL SOCIETY

pubs.acs.org/JPCL
Letter

Isolating Pure Donor and Acceptor Signals by Polarization-Controlled Transient Absorption Spectroscopy

Yi Xu, Lars Mewes, Erling Thyrhaug, Vladislav Sláma, František Šanda, Heinz Langhals, and Jürgen Hauer*

Cite This: *J. Phys. Chem. Lett.* 2023, 14, 5390−5396

Read Online

ACCESS | Metrics & More | Article Recommendations | Supporting Information

ABSTRACT: The optical spectra of molecules are often highly congested, inhibiting definite assignment of features and dynamics. In this work, we demonstrate and apply a polarization-based strategy for the decomposition of time-resolved optical spectra to analyze the electronic structure and energy transfer in a molecular donor−acceptor (D−A) dyad. We choose a dyad with orthogonal transition dipole moments for D and A and high fluorescence quantum yield to show that polarization-controlled ultrafast transient absorption spectra can isolate the pure D and A parts of the total signal. This provides a strategy to greatly reduce spectral congestion in complex systems and thus allows for detailed studies of electronic structure and electronic energy transfer.

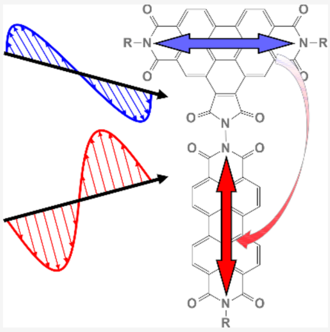

Investigations of primary processes in chemical dynamics, such as the breaking of individual bonds, charge separation, or excitation energy transfer (EET), are of great interest to both basic and applied research. Unravelling these processes calls for temporal resolution of nuclear motions on their natural time scales. Time-resolved optical spectroscopies have emerged as the state-of-the-art tools in this context. Routinely generated sub-100 fs optical pulses allow near-impulsive initiation of dynamics, after which the system's time-evolution can be followed in detail on time scales of vibrational periods or even shorter. A particularly notable success story for this approach is the investigation of EET in a variety of complex artificial and natural light harvesters, where ultrafast spectroscopies have been crucial in elucidating their functionality and underlying physical mechanisms.[1−3]

Femtosecond transient absorption (TA) spectroscopy[4,5] is the most widely used among the ultrafast optical techniques where photoinduced dynamics are monitored by changes in optical density (OD) as a function of time delay after excitation. The broad spectral range and high time-resolution in TA experiments yield data amenable to quantitative kinetic analysis techniques such as global target analysis (GTA)[6,7] and integral transform approaches.[8] Such quantitative methods become strictly necessary when spectral features in TA rapidly evolve or overlap, which is the norm rather than the exception, regardless of the size of the investigated system.[7,9] Experimental strategies to reduce the complexity of TA-data are thus clearly desirable. Presumably the most feasible approach is to exploit the polarization of light and the inherent directionality of molecular transition dipole moments (TDMs).[10]

Here, we demonstrate a new polarization-based method to reduce spectral congestion in TA experiments, thereby significantly alleviating the difficulties in quantitative data analysis. As in standard anisotropy measurements, our approach allows us to extract relative TDM directions but simultaneously separates the TA spectrum into two simpler components—the "polarization associated spectra" (PAS). We apply the methodology to the orthogonal intramolecular donor−acceptor (D−A) dyad perylene-benzoperylene quinquimide (PBQ) (Figure 1). Perylene bisimides (PBIs) are photoactive molecules used as functional materials[11−17] for optical and electrical sensors;[18−22] in labeling and imaging;[20,21] photovoltaics;[23−28] and in solar energy harvesting.[13,28−30] Both in applications and as model systems, they are of particular interest due to their chemical versatility and convenient spectroscopic properties, such as the high fluorescence quantum yield and photostability.[31−33] The D−A molecule as depicted in Figure 1 is a prototypical "ortho-FRET" dyad featuring an orthogonal arrangement of the donor (D) and acceptor (A) moieties. A naïve analysis based on the apparent orthogonality of donor and acceptor TDMs would suggest inefficient excitation energy transfer. Nevertheless, in experimental studies carried out on similar ortho-FRET systems, EET takes place within a few picoseconds.[32,34−36] This

Received: May 26, 2023
Accepted: June 1, 2023
Published: June 6, 2023

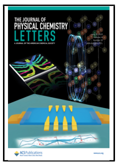

https://doi.org/10.1021/acs.jpclett.3c01451

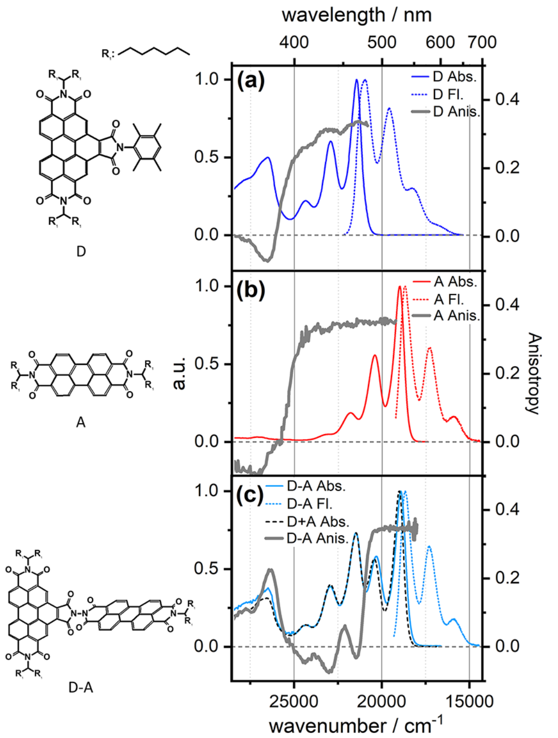

Figure 1. Normalized absorption (solid lines) and fluorescence (dotted lines) spectra of investigated molecules in chloroform solution: (a) benzo[*ghi*]perylenetriimide (D), (b) perylene bisimide (A), and (c) perylene-benzoperylene quinquimide (D−A). The dashed black line depicts the sum of isolated D and A absorption spectra. In panels a−c, the associated fluorescence excitation anisotropy as measured in poly(tetrahydrofuran) at 30 °C is shown as full gray lines.

inconsistency in the simple Förster picture has sparked a wealth of competing theories, including thermally induced deviations from a strictly orthogonal molecular geometry,[32] non-Condon effects (excited state reorganization),[37] or low-frequency anharmonic structural motion.[38] In the present work we add further aspects to this debate by experimental insight provided by polarization-controlled TA spectroscopy. We show that the decomposition of the TA-data into PAS lets us ascribe spectral species and decay times to either donor or acceptor moieties in the weakly coupled D−A system shown in Figure 1. We support our analysis of D−A with data from the isolated donor molecule in solution using the same methodology.

In Figure 1a−c we show absorption and fluorescence spectra of D, A, and the D−A dyad, respectively. All spectra are presented in TDM representation.[39,40] The relatively good absorption−emission mirror image symmetry for both D and A confirms the vibronic origin of the spectral progressions. Small deviations in spacing and relative peak magnitudes between absorption and emission spectra can be explained by slight anharmonicities of vibrational potentials.[37,41−43] The absorption spectrum of D−A, shown as the light-blue line in Figure 1c, corresponds almost exactly to the sum of the uncoupled molecules D and A, requiring only a minor red-shift of ∼50 cm^{-1} of A in order to achieve essentially perfect agreement. The small spectral shift demonstrates that the D−A electronic coupling is weak, suggesting that the assumptions underlying Förster theory for excitation transport are satisfied. The absence of D-fluorescence in D−A nevertheless implies fast and efficient EET. We calculated the donor−acceptor overlaps to estimate the possibility of Dexter transport (Supporting Information) but found the respective coupling to be about 0.1 cm^{-1}, which is orders of magnitude below what is necessary to explain the observed transfer rates. Hence, the D−A system treated in this work exhibits a discrepancy between fast EET and orthogonal geometry; similar effects have been reported and discussed for other ortho-FRET dyads.[32,44]

Superimposed onto the absorption spectra in Figure 1a−c we show the corresponding fluorescence excitation anisotropy spectra ($r(\lambda)$, gray solid lines) of the compounds, as recorded in poly-THF matrix. For $r(\lambda)$, we employ the standard definition:[45]

$$r(\lambda, t) = \frac{I_{\parallel} - I_{\perp}}{I_{\parallel} + 2I_{\perp}} = \frac{2}{5} \cdot \frac{3\cos^2\theta - 1}{2} \tag{1}$$

where $I_{\parallel}$ ($I_{\perp}$) is the measured signal for the detection polarized parallel (orthogonal) to the polarization of the excitation light and θ is the (time-dependent) angle between the excited and detected TDM. As seen in Figure 1a, $r(\lambda)$ reaches a maximal value of ∼0.34 for D at the red edge of the absorption spectrum. According to eq 1 this implies a relatively large effective angle of $\theta \approx 18°$ between the 0−0 transitions of absorption and emission in D. The anisotropy of A also fails to reach the limiting value of 0.4 corresponding to $\theta \approx 0$, although to a much smaller degree. This leads to a FRET-relevant angle between the TDMs of D de-excitation and A excitation of ∼72°. Following the estimations described in the Supporting Information, the effective angle between the dipole moments for D de-excitation and A excitation should be ∼61° to reproduce the experimentally observed transfer rates (see SI Table S2). In essence, while both spectroscopic measurements and the ultrafast transfer time discussed below support the notion of Förster transfer, the challenge lies in the correct estimation of the coupling constant. We have addressed this issue recently by detailed MD/QC calculations for a related ortho-dyad.[38]

The most widespread use of polarization control in ultrafast spectroscopy are TA-measurements under so-called "magic angle" (MA) conditions, where the relative polarization angle between excitation and detection fields are 54.7°. This allows for the extraction of excited-state population dynamics absent of depolarization artifacts. The number of studies combining more extensive polarization control and ultrafast spectroscopy is still limited.[10,46−50] Information on changes in molecular structure is extracted from transient absorption anisotropy (TAA) experiments, which—in direct analogy to common fluorescence anisotropy experiments discussed in Figure 1—reveal the relative angle between the photoexcited and detected TDM in its time-dependence by measuring $r(\lambda, t)$. While $r(\lambda, t)$ in principle contains all available information about relative TDM directions and their dynamics, its interpretation is more challenging. Three problems in particular stand out: (i) Unlike fluorescence, TA signals are signed and cancellations of the total signal occur in regions of spectral overlap between positive and negative signals. In this case, $r(\lambda, t)$ diverges, as depicted in Figure 2. (ii) In fluorescence anisotropy, the values for $r(\lambda, t)$ range from −0.2 to 0.4 for orthogonal and parallel TDMs in excitation and detection, respectively. In TAA, the values for $r(\lambda, t)$ may be found outside of this range if positive and negative TA-signals overlap, which would lead to unphysical values for the relative

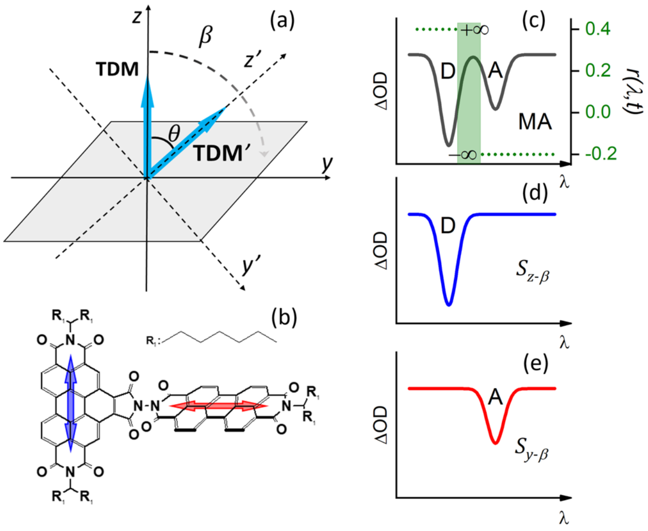

Figure 2. (a) Definition of angles θ and β. The former spans between pumped and probed TDMs of the investigated molecule, while β stands for the angle between the pumped TDM and the coordinate system, in which the signal components S_z and S_y are defined. (b) Sketch of the ortho-FRET D−A molecule under investigation. (c) Sketch of $r(\lambda, t)$ for the ortho-FRET molecule. (d and e) Respective S_z and S_y-signals, which are both nondivergent and retain spectral information as compared to $r(\lambda, t)$. Importantly, the signals are specific to either the donor- (S_z) or acceptor-moiety (S_y).

angles between TDMs. (iii) In contrast to TA-signals $r(\lambda, t)$ does not directly reflect population dynamics but also includes changes of the TDM-directions over time. This can make the time-evolution of TAA difficult to interpret.

These limitations call for strategies retaining the spectral signatures of TA, while highlighting how they are associated with the direction of the underlying TDM. Similar ideas were established in polarization-controlled steady-state spectroscopies, *e.g.*, the method of stepwise reduction by Thulstrup, Eggers, and Michl[51−53] as a straightforward technique to extract relative TDM angles from linear dichroism data. The TAA signal has two isotropic tensor components,[54−56] most simply represented by spectra derived from experiments with parallel and perpendicular polarizations between pump and probe pulses. This representation is in the macroscopic lab frame; suitable linear combinations of these spectra may express the signal in terms of components in the molecular frame and thus bring better insight into the relative orientation of molecular TDMs. This approach meaningfully separates the isotropic spectrum into linearly independent components. Special cases of this strategy have successfully been applied to fluorescence[10,57] and two-dimensional electronic spectroscopy.[47,50,58] In these approaches, the isotropic spectrum is projected into contributions which are either parallel (S_z, see eq 2 for $\beta = 0$), or orthogonal (S_y, see eq 3 for $\beta = 0$) to the TDM initially excited by the pump pulse. While this is a highly useful approach to decrease the complexity of spectra, the separation into orthogonal components does not retain information on relative TDM angles and may lead to poor separation of features in molecules of low symmetry. Here, we avoid this constraint and formulate general expressions suitable for systems where the relative angle between TDMs is arbitrary (see the Supporting Information for derivations). These expressions read[10,57]

$$S_z = (S_{\|}(\lambda, t) + 2\cdot S_{\perp}(\lambda, t))\cdot\left(\frac{3\cos^2\beta - (2 - 5\cdot r(\lambda, t))}{3\cdot(2\cdot\cos^2\beta - 1)}\right) = 3\cdot\mathrm{MA}\cdot\left(\frac{\cos^2\beta - (1 - \cos^2\theta)}{(2\cdot\cos^2\beta - 1)}\right) \tag{2}$$

and

$$S_y = (S_{\|}(\lambda, t) + 2\cdot S_{\perp}(\lambda, t))\cdot\left(\frac{3\cos^2\beta - (5\cdot r(\lambda, t) + 1)}{3\cdot(2\cdot\cos^2\beta - 1)}\right) = 3\cdot\mathrm{MA}\cdot\left(\frac{\cos^2\beta - \cos^2\theta}{(2\cdot\cos^2\beta - 1)}\right) \tag{3}$$

The terms $\left(\frac{3\cos^2\beta - (2 - 5\cdot r(\lambda, t))}{3\cdot(2\cdot\cos^2\beta - 1)}\right)$ and $\left(\frac{3\cos^2\beta - (5\cdot r(\lambda, t) + 1)}{3\cdot(2\cdot\cos^2\beta - 1)}\right)$ are directly analogous to $r(\lambda, t)$, in that they report on the angle θ between pumped and probed TDMs, but they are expressed in the frame of the molecule. We depict this schematically in Figure 2a, with the specific TDM orientation of D−A pumped (probed) TDMs shown as blue (red) arrows in Figure 2b.

In earlier work, the orientation of the molecular frame has in general been such that one coordinate axis (say, the z-axis) is oriented parallel to the pumped TDM.[10,58] In eqs 2 and 3, we allow the coordinate system defining the molecular frame to be rotated by an angle β away from the pumped TDM. Setting β to zero, we recover the expressions from earlier studies[10,58] with the pumped TDM being parallel to the z-axis. In this case, the terms in parentheses in eqs 2 and 3 simply reduce to $\cos^2\theta$ and $(1-\cos^2\theta)$—separating the probed TDM in projections onto the z-axis (S_z) and the x/y-plane (S_y), respectively.

Figure 2c−e illustrates how changing β is useful when investigating EET in a D−A system in which the TDMs of D and A moieties are nonparallel. From a conventional TAA experiment, we can extract the anisotropy $r(\lambda, t)$, which reports on the relative angle between the involved TDMs through the expression in eq 1. As noted, however, this representation retains no information on the spectral structure and diverges whenever the TA-signal approaches zero, as depicted in Figure 2c. If we now apply eqs 2 and 3 to the TAA data, we can extract polarization associated spectra S_z and S_y. These are the TA-analogue of linear dichroism spectra. In the idealized case of exactly orthogonal D- and A-transitions, the TA spectrum will thus decompose into linearly independent components at $\beta = 0$. As compared to $r(\lambda, t)$, spectral information is retained in S_z and S_y and there is no divergence problem as shown in Figure 2d,e. In more general case where θ is close to but not exactly 0° or 90°, an appropriate choice of β can still lead to components $S_{z,y}$ predominated by either D or A-character and thus a reduction of the overall spectral complexity. Moreover, by taking the approach of stepwise reduction, it becomes possible to assign relative angles to spectral features: at appropriate choice of β, it is possible to remove features from one of the component spectra. For isolated spectral features, this occurs exactly when β equals θ. In the following, we exemplify our approach on the D−A molecule depicted in Figures 1 and 2b.

As we are interested in the ultrafast D-to-A EET process, it is convenient to initiate the dynamics in a fs TA experiment by preferential excitation of the D−A donor moiety. We can achieve this to good approximation by using pump pulses centered at 400 nm (50 fs). We show the respective TA spectra recorded at magic angle (MA) conditions of D−A in Figure 3, where the pump pulse spectrum is shown as a dark blue filled curve in panel a. Corresponding transient absorption data of the isolated D molecule can be found in SI Figure S4a.

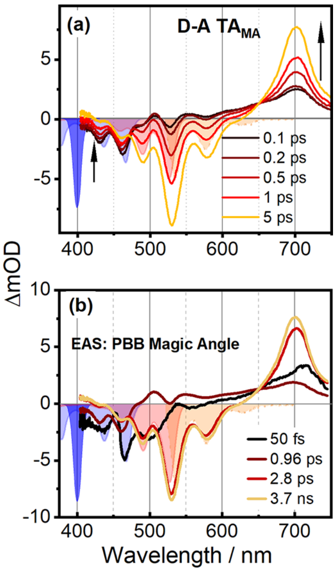

Figure 3. (a) Transient spectra of D–A at indicated delay times. The dark blue filled curve represents the pump pulse centered at 400 nm. The light blue (light red) filled curves are the absorption spectra of isolated donor (acceptor). (b) Evolution associated spectra for the D–A molecule. The indicated times denote the decay times of the respective spectral species.

The negative signals in the 400–600 nm range can be attributed to ground-state bleach (GSB) and stimulated emission (SE) of the donor and acceptor moieties, respectively, by comparison with absorption and fluorescence spectra. For both moieties the excited-state absorption (ESA) appears as broad, positive signal bands in the red to NIR range.

At increasing pump–probe delays we observe pronounced spectral changes, as highlighted by black arrows in Figure 3a. These changes can be directly attributed to EET between the donor and acceptor moieties of the D–A molecule. We extract quantitative insight into this process from global lifetime analysis (GLA) of the decay dynamics using the OPTIMUS software package.[59] The results of this analysis are shown in Figure 3b. Here, we find that the observed decay dynamics requires a model with four individual kinetic components, showing time constants of <100 fs, 0.96 ps, 2.8 ps, and 3.7 ns, respectively. Note that the last component was fixed to the D–A fluorescence lifetime, while the other time scales were fitted.[60] The fastest of these components can, based on the known solvation dynamics of chloroform, be associated with fast inertial solvation.[61,62] The 0.96 ps component that follows has essentially the spectral structure of D. As no subsequent components have traces of this spectrum, this demonstrates that population leaves D completely with a ∼1 ps time constant. The last two components (2.8 ps and 3.7 ns, fixed) are both highly similar to that of the isolated A moiety. We hence attribute them to relaxation within the acceptor-moiety (2.8 ps) and the overall ground-state recovery (3.7 ns).

Having performed TA and GLA of the photoinduced D–A dynamics, we now employ this simple system to demonstrate the potential for simplified analysis afforded by polarization spectroscopy. We calculate PS according to eqs 2 and 3 and denote them as S_z and S_y, respectively. $S_{z-0°}$ and $S_{y-0°}$ stand for PAS for $\beta = 0°$. The spectra of the $S_{z-0°}$ and $S_{y-0°}$ at 200 fs time delay for D are shown in Figure 4a,b as light-blue solid curves.

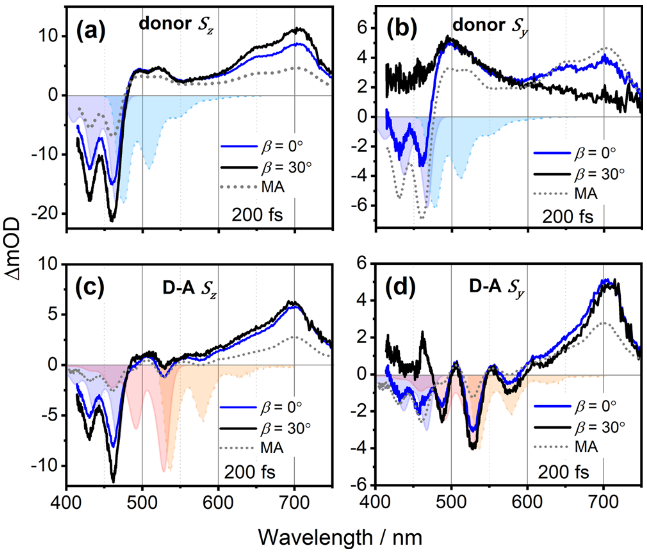

Figure 4. Polarization-associated TA spectra as a function of β for D–A (a and b) and D (c and d) at 200 fs delay time. The MA-TA spectrum is shown as a gray dotted line for comparison. The light blue (light red) filled curves are the absorption spectra of isolated donor (acceptor).

Compared with the MA TA data, shown as a gray dotted curve, the intensity of the GSB signal peaks at 430 and 460 nm is doubled in $S_{z-0°}$ and slightly suppressed in $S_{y-0°}$. We attribute this to an ESA-transition spectrally overlapping with the GSB band, yet with a difference in TDM. While this is an interesting finding, inspection of $S_{z-0°}$ and $S_{y-0°}$ for D–A in Figure 4c,d illustrates that the choice of $\beta = 0°$ is not ideal to decompose the TA data, as many features still appear in both component spectra. For example, $S_{z-0°}$ for D–A in Figure 4c shows a negative peak at 530 nm, which stems from acceptor GSB/SE. The latter signal should not appear in $S_{z-0°}$ if the TDM's of donor and acceptor moiety were orthogonal (and rigid) and hence be suppressed by an ideal projection scheme. Similarly, $S_{y-0°}$ should not contain negative signals at wavelengths shorter than 450 nm, as they stem from the donor-moiety and should therefore be *z*-polarized. In search for a better suited basis, we change β, which is equivalent to rotating the coordinate system spanned by S_z and S_y as depicted in Figure 3a. The choice of β is made according to the anisotropy value at 400 nm in Figure 1c. Following eq 1, an anisotropy value of −0.05 leads to a relative angle between excitation and emission of 30°. We note that the optimal value for β is stable with respect to the delay time (see Figure S5).

In the $S_{z-30°}$ of D–A as shown in Figure 4c, the GSB-peaks of the donor moiety at 430 and 460 nm are enhanced, while the acceptor-related peak at 530 nm is significantly reduced. The positive signals at 505 nm and above 560 nm correspond to the ESA of the donor moiety, strongly resembling the respective features in $S_{z-30°}$ spectrum of D, as shown in Figure 4a. The $S_{y-30°}$ spectrum of D–A shown in Figure 4d exhibits a complementary behavior: donor features are suppressed, leaving acceptor features as the dominant contribution. For example, $S_{y-30°}$ of D–A shows no negative signals at wavelengths shorter than 470 nm, as this is the GSB region of the donor with a TDM orthogonal to the S_y direction. In this region, the $S_{y-30°}$ spectrum reveals weak *y*-polarized ESA-features, the existence of which also explains the increase of GSB strength for $S_{z-30°}$ over MA, respectively (see Figure 4c).

GLA of the polarized TA spectral components reveals a central advantage of our approach. (We note that in order to avoid TAA contributions from orientational diffusion, we exclude TA data for delay times longer than 40 ps from our analysis.) The resulting time constants for D−A (Table 1) illustrate the same trend observed for the spectra in Figure 4: rotation of the coordinate system by changing β separates donor from acceptor-inherent dynamical components; donor (acceptor) features appear exclusively in $S_{z-30°}$ ($S_{y-30°}$). In particular, GLA analysis of the $S_{z-30°}$ spectra of D−A reveals only two components with lifetime constants of <100 fs and 1.09 ps, *i.e.*, inertial relaxation in the donor moiety and donor-to-acceptor transfer. Spectra are shown in the Supporting Information, Figure S3. The $S_{y-30°}$ transient spectra reveal three components with lifetime constants of 0.94 ps, 2.8 ps (fixed), and 3.7 ns (fixed). The fact that the ∼1 ps component appears in both $S_{y-30°}$ and $S_{z-30°}$ elegantly confirms its assignment to EET. Furthermore, the 2.8 ps component is found in $S_{y-30°}$ but not in $S_{z-30°}$, supporting its interpretation as relaxation within the acceptor moiety.

Table 1. Time Constants Extracted by Global Lifetime Analysis for D−A for Components of Indicated Polarization[a]

	TA_{MA}	$S_{z-30°}$	$S_{y-30°}$
$\tau_1 \sim$ sub-100 fs	50 fs	70 fs	
$\tau_2 \sim$ 1 ps	0.96 ps	1.09 ps	0.94 ps
$\tau_3 \sim$ several ps	2.8 ps		2.8 ps (f)
$\tau_4 \sim$ long decay	3.7 ns (f)		3.7 ns (f)

[a] (f) stands for fixed decay time.

We showed that polarization-controlled TA spectroscopy in a D−A system with orthogonal TDMs allows for an intuitive and clear assignment of spectral species from GLA. At an optimal angle $\beta \sim 30°$, we retrieve pure donor and acceptor spectra in $S_{z\text{-}30°}$ and $S_{y\text{-}30°}$, respectively. In essence, PAS transient spectra successfully disentangle the overlapping spectral signatures of different steps in an EET-process. Our polarization-based measurements support the existence of significant geometric/dipole fluctuations in ortho-FRET dyads, supplementing the previous indirect evidence based on Förster theory of EET.[38] The approach for disentangling TAA-dynamics as described in our work provides new impulses for the description of dipole fluctuations and helps to distinguish between competing theories.[37,44] As demonstrated in the analysis of the isolated donor molecule D, the method presented here benefits from but is not limited to systems with orthogonally arranged transition dipole moments.

■ ASSOCIATED CONTENT

Supporting Information

The Supporting Information is available free of charge at https://pubs.acs.org/doi/10.1021/acs.jpclett.3c01451.

> Sample preparation, excitation anisotropy, TA experimental design, derivation for expressions for S_z and S_y, kinetic analysis, QM and MD calculations, estimation of FRET times (PDF)

■ AUTHOR INFORMATION

Corresponding Author

Jürgen Hauer − *Technical University of Munich, TUM School of Natural Sciences, Department of Chemistry, Professorship of Dynamic Spectroscopy, 85748 Garching, Germany;* orcid.org/0000-0002-6874-6138;
Email: juergen.hauer@tum.de

Authors

Yi Xu − *Technical University of Munich, TUM School of Natural Sciences, Department of Chemistry, Professorship of Dynamic Spectroscopy, 85748 Garching, Germany;* orcid.org/0000-0003-4723-6312
Lars Mewes − *Technical University of Munich, TUM School of Natural Sciences, Department of Chemistry, Professorship of Dynamic Spectroscopy, 85748 Garching, Germany;* orcid.org/0000-0001-9269-1475
Erling Thyrhaug − *Technical University of Munich, TUM School of Natural Sciences, Department of Chemistry, Professorship of Dynamic Spectroscopy, 85748 Garching, Germany;* orcid.org/0000-0001-8634-9606
Vladislav Sláma − *Institute of Physics, Faculty of Mathematics and Physics, Charles University, Prague 12116, Czech Republic*
František Šanda − *Institute of Physics, Faculty of Mathematics and Physics, Charles University, Prague 12116, Czech Republic;* orcid.org/0000-0003-2416-8804
Heinz Langhals − *Department of Chemistry, Ludwig-Maximilians-Universität München, 81377 Munich, Germany;* orcid.org/0000-0002-8038-4547

Complete contact information is available at:
https://pubs.acs.org/10.1021/acs.jpclett.3c01451

Notes

The authors declare no competing financial interest.

■ ACKNOWLEDGMENTS

F.S. and V.S. thank the Czech Science Foundation (GACR) for financial support through grant no. 22-26376S. J.H. acknowledges funding by the DFG under Germany's Excellence Strategy (EXC 2089/1-390776260) and by projects 514636421 and INST 95/1500-1. Y.X. and J.H. acknowledge that the project was funded by the DFG − TRR 325-444632635.

■ REFERENCES

(1) Kumpulainen, T.; Lang, B.; Rosspeintner, A.; Vauthey, E. Ultrafast Elementary Photochemical Processes of Organic Molecules in Liquid Solution. *Chem. Rev.* **2017**, *117* (16), 10826−10939.

(2) Rosspeintner, A.; Lang, B.; Vauthey, E. Ultrafast Photochemistry in Liquids. *Annu. Rev. Phys. Chem.* **2013**, *64* (1), 247−271.

(3) Valkunas, L.; Abramavicius, D.; Mancal, T. *Molecular Excitation Dynamics and Relaxation: Quantum Theory and Spectroscopy*; John Wiley & Sons: Berlin, 2013.

(4) Maiuri, M.; Garavelli, M.; Cerullo, G. Ultrafast Spectroscopy: State of the Art and Open Challenges. *J. Am. Chem. Soc.* **2020**, *142* (1), 3−15.

(5) Zewail, A. H. Femtochemistry: Atomic-Scale Dynamics of the Chemical Bond Using Ultrafast Lasers (Nobel Lecture). *Angew. Chem., Int. Ed.* **2000**, *39* (15), 2586−2631.

(6) Beechem, J. M. Global Analysis of Biochemical and Biophysical Data. In *Methods in Enzymology*; Elsevier: 1992; Vol. *210*, pp 37−54.

(7) Ruckebusch, C.; Sliwa, M.; Pernot, P. d.; De Juan, A.; Tauler, R. Comprehensive Data Analysis of Femtosecond Transient Absorption Spectra: A Review. *J. Photochem. Photobiol., C* **2012**, *13* (1), 1−27.

(8) Kutta, R.-J.; Langenbacher, T.; Kensy, U.; Dick, B. Setup and Performance of a Streak Camera Apparatus for Transient Absorption Measurements in the Ns to Ms Range. *Appl. Phys. B: Laser Opt.* **2013**, *111*, 203−216.

(9) Beckwith, J. S.; Rumble, C. A.; Vauthey, E. Data Analysis in Transient Electronic Spectroscopy−an Experimentalist's View. *Int. Rev. Phys. Chem.* **2020**, *39* (2), 135−216.

(10) Thyrhaug, E.; Sorensen, T. J.; Gryczynski, I.; Gryczynski, Z.; Laursen, B. W. Polarization and Symmetry of Electronic Transitions in Long Fluorescence Lifetime Triangulenium Dyes. *J. Phys. Chem. A* **2013**, *117* (10), 2160−8.

(11) Li, C.; Wonneberger, H. Perylene Imides for Organic Photovoltaics: Yesterday, Today, and Tomorrow. *Adv. Mater.* **2012**, *24* (5), 613−636.

(12) Avlasevich, Y.; Li, C.; Müllen, K. Synthesis and Applications of Core-Enlarged Perylene Dyes. *J. Mater. Chem.* **2010**, *20* (19), 3814−3826.

(13) Macedo, A. G.; Christopholi, L. P.; Gavim, A. E.; de Deus, J. F.; Teridi, M. A. M.; Yusoff, A. R. b. M.; da Silva, W. J. Perylene Derivatives for Solar Cells and Energy Harvesting: A Review of Materials, Challenges and Advances. *J. Mater. Sci.: Mater. Electron.* **2019**, *30* (17), 15803−15824.

(14) Brown, K. E.; Salamant, W. A.; Shoer, L. E.; Young, R. M.; Wasielewski, M. R. Direct Observation of Ultrafast Excimer Formation in Covalent Perylenediimide Dimers Using near-Infrared Transient Absorption Spectroscopy. *J. Phys. Chem. Lett.* **2014**, *5* (15), 2588−2593.

(15) Kölle, P.; Pugliesi, I.; Langhals, H.; Wilcken, R.; Esterbauer, A. J.; de Vivie-Riedle, R.; Riedle, E. Hole-Transfer Induced Energy Transfer in Perylene Diimide Dyads with a Donor−Spacer−Acceptor Motif. *Phys. Chem. Chem. Phys.* **2015**, *17* (38), 25061−25072.

(16) Christensen, R. L.; Drake, R. C.; Phillips, D. Time-Resolved Fluorescence Anisotropy of Perylene. *J. Phys. Chem.* **1986**, *90* (22), 5960−5967.

(17) Ambrosino, F.; Califano, S. The Vibrational Spectrum of Perylene. *Spectrochim. Acta* **1965**, *21* (8), 1401−1409.

(18) Geng, T.-M.; Li, D.-K.; Zhu, Z.-M.; Zhang, W.-Y.; Ye, S.-N.; Zhu, H.; Wang, Z.-Q. Fluorescent Conjugated Microporous Polymer Based on Perylene Tetraanhydride Bisimide for Sensing O-Nitrophenol. *Anal. Chim. Acta* **2018**, *1011*, 77−85.

(19) Liu, K.; Shang, C.; Wang, Z.; Qi, Y.; Miao, R.; Liu, K.; Liu, T.; Fang, Y. Non-Contact Identification and Differentiation of Illicit Drugs Using Fluorescent Films. *Nat. Commun.* **2018**, *9* (1), 1−11.

(20) Georgiev, N. I.; Said, A. I.; Toshkova, R. A.; Tzoneva, R. D.; Bojinov, V. B. A Novel Water-Soluble Perylenetetracarboxylic Diimide as a Fluorescent Ph Probe: Chemosensing, Biocompatibility and Cell Imaging. *Dyes Pigm.* **2019**, *160*, 28−36.

(21) He, J.; Chen, H.; Guo, Y.; Wang, L.; Zhu, L.; Karahan, H. E.; Chen, Y. Polycondensation of a Perylene Bisimide Derivative and L-Malic Acid as Water-Soluble Conjugates for Fluorescent Labeling of Live Mammalian Cells. *Polymers* **2018**, *10* (5), 559.

(22) Yao, Z.; Zhang, M.; Wu, H.; Yang, L.; Li, R.; Wang, P. Donor/Acceptor Indenoperylene Dye for Highly Efficient Organic Dye-Sensitized Solar Cells. *J. Am. Chem. Soc.* **2015**, *137* (11), 3799−3802.

(23) Würthner, F. Perylene Bisimide Dyes as Versatile Building Blocks for Functional Supramolecular Architectures. *Chem. Commun.* **2004**, No. 14, 1564−1579.

(24) Liu, F.; Hou, T.; Xu, X.; Sun, L.; Zhou, J.; Zhao, X.; Zhang, S. Recent Advances in Nonfullerene Acceptors for Organic Solar Cells. *Macromol. Rapid Commun.* **2018**, *39* (3), 1700555.

(25) Zhan, X.; Tan, Z. a.; Domercq, B.; An, Z.; Zhang, X.; Barlow, S.; Li, Y.; Zhu, D.; Kippelen, B.; Marder, S. R. A High-Mobility Electron-Transport Polymer with Broad Absorption and Its Use in Field-Effect Transistors and All-Polymer Solar Cells. *J. Am. Chem. Soc.* **2007**, *129* (23), 7246−7247.

(26) Liu, Y.; Cole, M. D.; Jiang, Y.; Kim, P. Y.; Nordlund, D.; Emrick, T.; Russell, T. P. Chemical and Morphological Control of Interfacial Self-Doping for Efficient Organic Electronics. *Adv. Mater.* **2018**, *30* (15), 1705976.

(27) Hou, J.; Inganäs, O.; Friend, R. H.; Gao, F. Organic Solar Cells Based on Non-Fullerene Acceptors. *Nat. Mater.* **2018**, *17* (2), 119−128.

(28) Häupler, B.; Wild, A.; Schubert, U. S. Carbonyls: Powerful Organic Materials for Secondary Batteries. *Adv. Energy Mater.* **2015**, *5* (11), 1402034.

(29) Huang, T.; Lu, D.; Ma, L.; Xi, X.; Liu, R.; Wu, D. A Hit-and-Run Strategy Towards Perylene Diimide/Reduced Graphene Oxide as High Performance Sodium Ion Battery Cathode. *Chem. Eng. J. (Lausanne)* **2018**, *349*, 66−71.

(30) Langhals, H. Farbstoffe Für Fluoreszenz-Solarkollektoren. *Nachr. Chem. Technol. Lab.* **1980**, *28*, 716−718.

(31) Langhals, H. Control of the Interactions in Multichromophores: Novel Concepts. Perylene Bis-Imides as Components for Larger Functional Units. *Helv. Chim. Acta* **2005**, *88* (6), 1309−1343.

(32) Langhals, H.; Esterbauer, A. J.; Walter, A.; Riedle, E.; Pugliesi, I. Förster Resonant Energy Transfer in Orthogonally Arranged Chromophores. *J. Am. Chem. Soc.* **2010**, *132* (47), 16777−16782.

(33) Sebastian, E.; Hariharan, M. Null Exciton-Coupled Chromophoric Dimer Exhibits Symmetry-Breaking Charge Separation. *J. Am. Chem. Soc.* **2021**, *143* (34), 13769−13781.

(34) Langhals, H.; Walter, A. FRET in Dyads with Orthogonal Chromophores and Minimal Spectral Overlap. *J. Phys. Chem. A* **2020**, *124* (8), 1554−1560.

(35) Langhals, H.; Poxleitner, S.; Krotz, O.; Pust, T.; Walter, A. FRET in Orthogonally Arranged Chromophores. *Eur. J. Org. Chem.* **2008**, *2008*, 4559−4562.

(36) Langhals, H.; Dietl, C. Vibronic Intramolecular Resonant Energy Transfer Along More Than 5 Nm: Synthesis of Dyads for a Re-Examination of the Distance Function of FRET. *J. Org. Chem.* **2022**, *87* (15), 9454−9465.

(37) Renger, T.; Dankl, M.; Klinger, A.; Schlücker, T.; Langhals, H.; Müh, F. Structure-Based Theory of Fluctuation-Induced Energy Transfer in a Molecular Dyad. *J. Phys. Chem. Lett.* **2018**, *9* (20), 5940−5947.

(38) Sláma, V.; Perlík, V.; Langhals, H.; Walter, A.; Mancal, T.; Hauer, J.; Šanda, F. Anharmonic Molecular Motion Drives Resonance Energy Transfer in Peri-Arylene Dyads. *Front. Chem.* **2020**, *8*, 579166.

(39) Didraga, C.; Pugžlys, A.; Hania, P. R.; von Berlepsch, H.; Duppen, K.; Knoester, J. Structure, Spectroscopy, and Microscopic Model of Tubular Carbocyanine Dye Aggregates. *J. Phys. Chem. B* **2004**, *108* (39), 14976−14985.

(40) Angulo, G.; Grampp, G.; Rosspeintner, A. Recalling the Appropriate Representation of Electronic Spectra. *Spectrochim. Acta, Part A* **2006**, *65* (3−4), 727−731.

(41) Galestian Pour, A.; Lincoln, C. N.; Perlík, V.; Šanda, F.; Hauer, J. Anharmonic Vibrational Effects in Linear and Two-Dimensional Electronic Spectra. *Phys. Chem. Chem. Phys.* **2017**, *19* (36), 24752−24760.

(42) McCoy, E.; Ross, I. Electronic States of Aromatic Hydrocarbons: The Franck-Condon Principle and Geometries in Excited States. *Aust. J. Chem.* **1962**, *15* (4), 573−590.

(43) Langhals, H. Fluorescence and Fluorescent Dyes. *Phys. Sci. Rev.* **2020**, *5* (8), 20190100 DOI: 10.1515/psr-2019-0100.

(44) Nalbach, P.; Pugliesi, I.; Langhals, H.; Thorwart, M. Noise-Induced Förster Resonant Energy Transfer between Orthogonal Dipoles in Photoexcited Molecules. *Phys. Rev. Lett.* **2012**, *108* (21), 218302.

(45) Lakowicz, J. R. *Principles of Fluorescence Spectroscopy*; Springer: New York, 2006.

(46) Brixner, T.; Gerber, G. Femtosecond Polarization Pulse Shaping. *Opt. Lett.* **2001**, *26* (8), 557−559.

(47) Read, E. L.; Schlau-Cohen, G. S.; Engel, G. S.; Wen, J.; Blankenship, R. E.; Fleming, G. R. Visualization of Excitonic Structure in the Fenna-Matthews-Olson Photosynthetic Complex by Polar-

ization-Dependent Two-Dimensional Electronic Spectroscopy. *Biophys. J.* **2008**, *95* (2), 847−856.

(48) Folie, B. D.; Tan, J. A.; Huang, J.; Sercel, P. C.; Delor, M.; Lai, M.; Lyons, J. L.; Bernstein, N.; Efros, A. L.; Yang, P.; et al. Effect of Anisotropic Confinement on Electronic Structure and Dynamics of Band Edge Excitons in Inorganic Perovskite Nanowires. *J. Phys. Chem. A* **2020**, *124* (9), 1867−1876.

(49) Kim, Y. S.; Wang, J.; Hochstrasser, R. M. Two-Dimensional Infrared Spectroscopy of the Alanine Dipeptide in Aqueous Solution. *J. Phys. Chem. B* **2005**, *109* (15), 7511−7521.

(50) Voronine, D. V.; Abramavicius, D.; Mukamel, S. Manipulating Multidimensional Electronic Spectra of Excitons by Polarization Pulse Shaping. *J. Chem. Phys.* **2007**, *126* (4), 044508.

(51) Thulstrup, E. W.; Eggers, J. Moment Directions of the Electronic Transitions of Fluoranthene. *Chem. Phys. Lett.* **1968**, *1* (13), 690−692.

(52) Michl, J.; Thulstrup, E. W. Ultraviolet and Infrared Linear Dichroism: Polarized Light as a Probe of Molecular and Electronic Structure. *Acc. Chem. Res.* **1987**, *20* (5), 192−199.

(53) Thulstrup, E. W.; Michl, J. Polarized Absorption Spectroscopy of Molecules Aligned in Stretched Polymers Bl. *Spectrochim. Acta A Mol. Spectrosc.* **1988**, *44* (8), 767−782.

(54) Weyl, H. *The Classical Groups: Their Invariants and Representations*; Princeton University Press, 1946.

(55) Jeffreys, H. On Isotropic Tensors. *Math. Proc. Cambridge Philos. Soc.* **1973**, *73*, 173−176, DOI: 10.1017/S0305004100047587.

(56) Andrews, D. L.; Thirunamachandran, T. On Three-Dimensional Rotational Averages. *J. Chem. Phys.* **1977**, *67* (11), 5026−5033.

(57) Albrecht, A. C. Polarizations and Assignments of Transitions: The Method of Photoselection. *J. Mol. Spectrosc.* **1961**, *6*, 84−108.

(58) Thyrhaug, E.; Zidek, K.; Dostal, J.; Bina, D.; Zigmantas, D. Exciton Structure and Energy Transfer in the Fenna-Matthews-Olson Complex. *J. Phys. Chem. Lett.* **2016**, *7* (9), 1653−60.

(59) Slavov, C.; Hartmann, H.; Wachtveitl, J. Implementation and Evaluation of Data Analysis Strategies for Time-Resolved Optical Spectroscopy. *Anal. Chem.* **2015**, *87* (4), 2328−36.

(60) Kalinin, S.; Speckbacher, M.; Langhals, H.; Johansson, L. B.-Å. A New and Versatile Fluorescence Standard for Quantum Yield Determination. *Phys. Chem. Chem. Phys.* **2001**, *3* (2), 172−174.

(61) Horng, M.; Gardecki, J.; Papazyan, A.; Maroncelli, M. Subpicosecond Measurements of Polar Solvation Dynamics: Coumarin 153 Revisited. *J. Phys. Chem.* **1995**, *99* (48), 17311−17337.

(62) Zhu, H.; Li, M.; Hu, J.; Wang, X.; Jie, J.; Guo, Q.; Chen, C.; Xia, A. Ultrafast Investigation of Intramolecular Charge Transfer and Solvation Dynamics of Tetrahydro [5]-Helicene-Based Imide Derivatives. *Sci. Rep.* **2016**, *6* (1), 1−12.

Supporting Information for

Isolating Pure Donor and Acceptor Signals by Polarization-Controlled Transient Absorption Spectroscopy

*Yi Xu[1], Lars Mewes[1], Erling Thyrhaug[1], Vladislav Sláma[2], František Šanda[2], Heinz Langhals[3] and Jürgen Hauer[1] **

[1] Technical University of Munich, TUM School of Natural Sciences, Department of Chemistry, Professorship of Dynamic Spectroscopy, Lichtenbergstraße 4, 85748 Garching, Germany

[2] Institute of Physics, Faculty of Mathematics and Physics, Charles University, Ke Karlovu 5, Prague 121 16, Czech Republic

[3] Department of Chemistry, Ludwig-Maximilians-Universität München, Munich, Germany

Corresponding Author

*juergen.hauer@tum.de

Table of Contents:

Sample preparation

2,10-Bis(1-hexylheptyl)-6-[4′-{2-(3,8,9,10-tetrahydro-9-(1-hexylheptyl)-1,3,8,10-tetraoxoanthra[2,1,9-*def*:6,5,10-*d′e′f′*]diisoquinoline-2(1*H*)-yl]-1*H*-pyrrolo[3′,4′:4,5]pyreno[2,1,10-*def*:7,8,9-*d′e′f′*]diisoquinoline-1,3,5,7,9,11(2*H*,6*H*,10*H*)hexaone: *N*,*N′*-Bis(1-hexylheptyl)benzo[*ghi*]-perylene-2,3,8,9,11,12-hexacarboxylic-2,3:8,9-bis(dicarboximid)-11,12-anhydride (CAS RN 259880-39-2, 110 mg, 130 μmol) and 2-amino-9-(1-hexylheptyl)anthra[2,1,9-*def*;6,5,10-*d'e'f'*]diisoquinoline-1,3,8,10-tetraone (RN 207394-04-5, 100 mg, 170 μmol) were dissolved in quinoline (8 mL) and heated at 150°C for 16 h, allowed to cool, treated with 2 M aqueous HCl (50 mL), extracted with chloroform (3 × 50 mL), dried with magnesiumsulphate, and purified by column separation (silica gel, $CHCl_3$/EtOH 50:1, 600 × 22 mm). Yield 95 mg (52 %) orange red solid, m.p. > 250°C. R_f-value (silica gel, $CHCl_3$/EtOH 50:1) = 0.29. IR (ATR): $\tilde{\nu}$ = 2954.0 (m), 2924.9 (s), 2856.0 (m), 2361.5 (w), 2335.0 (w), 1793.3 (w), 1745.8 (m), 1727.8 (m), 1702.6 (vs), 1662.0 (vs), 1626.2 (w), 1593.8 (m), 1524.7 (w), 1456.6 (w), 1414.4 (m), 1404.3 (w), 1365.3 (m), 1320.9 (vs), 1245.1 (w), 1211.5 (w), 1171.9 (m), 1105.8 (w), 963.9 (w), 852.8 (w), 810.6 (m), 763.1 (w), 749.7 cm^{-1} (w). ^1H-NMR (600 MHz, $CDCl_3$, 25°C, TMS): δ = 0.79-0.84 (m, 18 H, 6 × CH_3), 1.21-1.41 (m, 48 H, 24 × CH_2), 1.85-1.96 (m, 6 H, 3 × β-CH_2), 2.23-2.34 (m, 6 H, 3 × β-CH_2), 5.17-5.23 (m, 1 H, N-CH), 5.26-5.32 (m, 2 H, 2 × N-CH), 8.67-8.78 (m, 8 H, 8 × $CH_{perylene}$), 9.20-9.28 (m, 2 H, 2 × $CH_{perylene}$), 9.51 (d, ^3J(H,H) = 8.4 Hz, 2 H, 2 × $CH_{perylene}$), 10.48-10.53 ppm (m, 2 H, 2 × $CH_{perylene}$). ^{13}C-NMR (150 MHz, $CDCl_3$, 25°C, TMS): δ = 14.0, 22.6, 27.0, 29.2, 31.7, 32.4, 54.9, 55.3, 122.2, 123.1, 123.5, 123.9, 124.4, 125.3, 126.1, 126.4, 126.8, 127.0, 127.9, 128.6, 129.5, 130.0, 131.2, 132.7, 133.5, 133.9, 136.2, 160.5, 163.9 ppm. UV/Vis ($CHCl_3$): λ_{max} (ε) = 377.9 (45000), 411.1 (16500), 436.7 (44300), 466.1 (78300), 492.4

(59200), 529.5 nm (95100). Fluorescence ($CHCl_3$, λ_{exc} = 437 nm): λ_{max} (I_{rel}) = 538.8 (1.00), 582.6 (0.51), 632.0 nm (0.12). Fluorescence quantum yield ($CHCl_3$, λ_{exc} = 437 nm, $E_{437\,nm\,/\,1\,cm}$ = 0.0096, reference: **C25** RN 335458-21-4 with Φ = 1.00): 0.98. MS (FAB$^+$): *m/z* (%): 1417 (4) [M^+-H], 1236 (14) [M^+], 1055 (15), 1054 (15), 872 (22). $C_{91}H_{95}N_5O_{10}$ (1417.7): Calcd. C 77.04, H 6.75, N 4.94; found C 76.73, H 6.57, N 4.93.

Steady-state spectroscopy

Standard absorption and emission measurements of the BPTI (donor, **D**), PDI (acceptor, **A**) and PBB (dyad, **D-A**) are performed in chloroform at an optical density (OD) of 0.35 at the respective absorption maxima inside a 1 cm cuvette. The absorption spectra are recorded on a UV–VIS spectrophotometer (Lambda 365 UV–VIS spectrophotometer, PerkinElmer Instruments Inc.) and fluorescence spectra are measured on an FS5 spectrofluorometer from Edinburgh Instruments.

Excitation anisotropy

In order to minimize depolarization due to rotational diffusion, all anisotropy measurements were performed on samples dissolved in poly(tetrahydrofuran) (pTHF, average Mn ~2900, Aldrich chemistry). The polymer samples were kept at 30 °C with an electronic Peltier element in order to maintain the transparency of the sample. Excitation anisotropy measurement are performed on the FS5 spectrofluorometer (Edinburgh Instruments) together with two polarizer assemblies, one in the excitation beam path, the other in the emission beam path. Each polarizer assembly contains an α-BBO polarizing prism with an operating range from 220 nm to 900 nm. The rotation of the polarizing prism is computer controlled to an accuracy of 0.5°. An angle of 0° corresponds to vertically linear polarized light, whereas an angle of 90° corresponds to horizontally linear polarized light (vertical and horizontal refer to the optical plane of the FS5 spectrometer). Samples for anisotropy measurement were prepared in poly(tetrahydrofuran) (poly-THF, average $M_n \approx 2900$, Aldrich chemistry) and inside a quartz cuvette with a path length of 1 cm at room temperature, the maximum OD is less than 0.05 to reduce self-absorption. The excitation anisotropy was calculated from

eq. S1
$$r(\lambda_{ex}) = \frac{F_{VV}(\lambda_{ex}) - G(\lambda_{ex}) \cdot F_{VH}(\lambda_{ex})}{F_{VV}(\lambda_{ex}) + 2 \cdot G(\lambda_{ex}) \cdot F_{VH}(\lambda_{ex})},$$

where F represents the fluorescence intensity and the subscripts refer to the settings of the excitation and emission polarizers, respectively. V is the vertical and H the horizontal setting. The $G(\lambda_{ex})$ factor, which is the ratio of the sensitivities of the detection system for vertically and horizontally, is used to corrected the measured spectra and is determined as

eq. S2
$$G(\lambda_{ex}) = \frac{F_{HV}(\lambda_{ex})}{F_{HH}(\lambda_{ex})}.$$

Transient absorption spectroscopy

Femtosecond time-resolved experiments are performed on a home-built transient absorption setup. 800 nm amplified laser pulses (Coherent Legend Elite Duo HE+) with 30 fs (FWHM) temporal duration and a repetition rate of 5 kHz are divided into pump and probe pulses and a temporal delay up to 1.5 ns with a minimum step size of 15 fs is achieved via optical path length variations using a mechanical delay stage (Newport, M-IMS300C) equipped with a Broadband retroreflector (Newport, M-BBR2.5-0.5). The pump pulse is frequency doubled inside a 100 µm thin beta-barium borate crystal (Bluebean Optical Tech Ltd.) to yield 400 nm excitation pulses with a temporal duration of approx. 54 fs (FWHM) determined from the instrument response function after GLA in OPTIMUS.[1] Its polarization is controlled by a broadband UV (300-470 nm) $\lambda/2$ plate (B.Halle Nachfl. GmbH). 1 µJ pulse is yielded by tuning another broadband visible (600-1200 nm) $\lambda/2$ plate (B.Halle Nachfl. GmbH) before BBO crystal. The pump pulse is focused using a 1 m focal length spherical mirror, and the sample is located in front of the focus where the beam spot size is ~ 1 mm in diameter. White light for detection is generated by focusing the probe laser pulse into a 5 mm thick CaF_2 crystal that is continuously translated in a plane orthogonal to the beam direction, in order to avoid optical damage to the crystal. The focal length is 100 mm and the numerical aperture of the focused beam is chosen to yield a white light spectrum that extends down to 350 nm. The white light pulse is collimated using a 100 mm focal length spherical mirror and the intensity of the fundamental is decreased using a heat absorbing filter. The white light is split into two parts, one part is chosen for probe and another for reference. The probe pulse is focused into the sample by using a 150 mm focal length spherical mirror and the spot size is ~ 100 µm and overlaps with the center of pump, and recollimated by using a 100 mm focal length spherical mirror. The probe and reference laser pulses are detected using a home-built prism spectrometer in combination with a pair of high-speed CMOS linear array cameras (Glaz LineScan-I-Gen2, Synertronic Designs). All the measurements performed in chloroform at an optical density (OD) of 0.3 at the respective absorption maxima at a cuvette with 100 µm optical path length. In addition to **D-A**, the isolated donor molecule was also measured by using same way for comparison. The experiment was done by setting the pump and probe pulses orthogonal, parallel and at MA with each other.

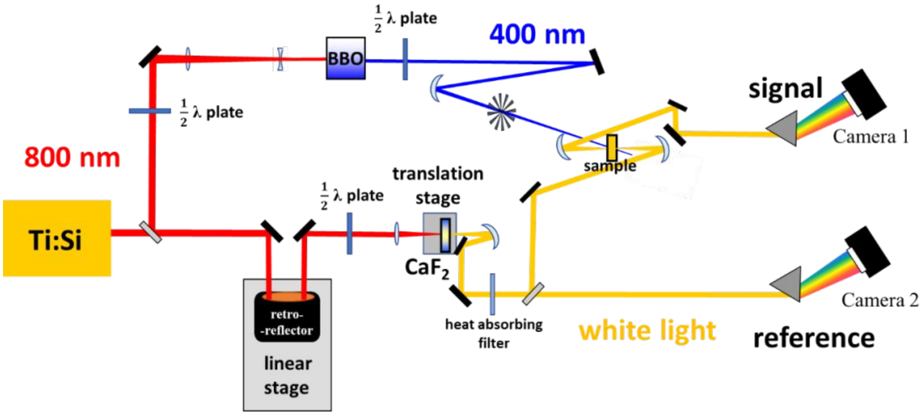

Figure S1 The layout used for polarization-controlled TA experiment

Transient absorption anisotropy spectroscopy

Transient absorption anisotropy spectroscopy (TAA) is obtained by measuring TA spectra for parallel and perpendicular orientation of pump and probe polarizations, $S_{\parallel}(\lambda,t)$ and $S_{\perp}(\lambda,t)$, respectively. This allows to calculate TAA as [2-5]

$$\text{eq. S3} \qquad r(\lambda,t) = \frac{S_{\parallel}(\lambda,t) - S_{\perp}(\lambda,t)}{S_{\parallel}(\lambda,t) + 2S_{\perp}(\lambda,t)}.$$

λ and t are written explicitly to highlight the wavelength- and time-dependent nature of the transient signals.

Transient absorption anisotropies (TAA) for both PBB and pure donor were presented in **Fig S4**, traces for each molecule at 435, 510, and 702 nm were plotted. For both dyad and pure donor, the spectral region around 435 nm is dominated GSB of donor. The fact that $r(\lambda,t)$ in this region is constant until 10 ps and then decays due to lack of GSB-signal indicates that rotational diffusion of the molecules is negligible within the observation window of our experiment. Due to energy transfer, the anisotropy trace of the dyad become noisy and lost information after 1 ps, and also cause the anisotropies at 530 and 702 nm in PBB decreased dramatically.

The anisotropy trace of the pure donor keeps steady in the initial 50 ps for all wavelength, which again indicates that rotational diffusion is negligible for this early time window. At 702 nm the ESA transitions is strongest. In absence of energy transfer, we can calculate the ESA-TDM angle β (relative to the GSB-TDM) by using

eq. S4
$$r(\lambda,t) = \frac{2}{5}\cdot\left(\frac{3\cdot cos^2\beta - 1}{2}\right).$$

This leads to values for β between 42 and 45° at 510 nm, and 30 to 33 ° degree for 702 nm. At 510 nm, we observe two different contributions at early and later times: initially, $r(510nm,t) \approx -0.2$, which speaks for an orthogonal TDM with respect to the GSB's TDM. Hence, we predominantly observe GSB of the acceptor at 510 nm at early times. At later times, $r(510nm,t)$ approaches zero, which is a sign of overall relaxation back to the electronic ground state.

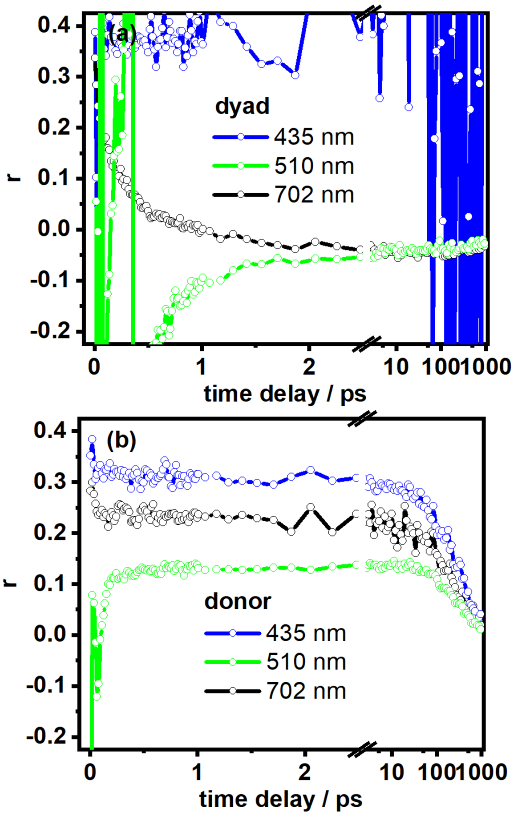

Figure S2 (a) Transient absorption anisotropy spectroscopy (TAA) trances for **(a) D-A** and **(b) D** at 435 nm, 510 nm and 702 nm.

Modification of the S_z and S_y expressions

An experimental set-up is placed in a laboratory Cartesian coordinate system with axes *A*, *B*, and *C*. Light is sent into the sample along the axis *B* and detected in the direction of *C*. The sample consists of randomly oriented, but fixed, molecules with an internal Cartesian axes *X*, *Y*, and *Z*. The polarization of the excitation light will show a component *p* in the direction of *A* and (1-*p*) along *C*. Albrecht showed (see ref. 21 of the main text) that the intensity of light polarized along the laboratory axes is proportional to:

$$\begin{aligned} &I_{\boldsymbol{A}} \propto (1-p)\, I_{\boldsymbol{B}} + [3(r_x q_x + r_y q_y + r_z q_z) + q_x(r_y + r_z) + q_y(r_x + r_z) + q_z(r_x + r_y)] \\ \text{eq. S5} \quad &I_{\boldsymbol{B}} \propto r_x q_x + r_y q_y + r_z q_z + 2[q(r_y + r_z) + q_y(r_x + r_z) + q_z(r_x + r_y)] \\ &I_{\boldsymbol{C}} \propto p\, I_{\boldsymbol{B}} + (1-p)[3(r_x q_x + r_y q_y + r_z q_z) + q_x\,(r_y + r_z) + q_y(r_x + r_z) + q_z(r_x + r_y)] \end{aligned}$$

The factors r_n and q_n refer to absorption and emission along the molecular *n*-axis respectively. In our set-up the exciting light is polarized entirely along the axis *A*-axis - i.e. $p = 1$. We arbitrarily choose the absorption and emission to occur in the molecular *YZ*-plane so that both absorption and emission along *X* is equal to zero, and the expressions above reduce to:

$$\text{eq. S6} \qquad \begin{aligned} I_{\boldsymbol{A}} &= 3(r_y q_y + r_z q_z) + r_y q_z + r_z q_y \\ I_{\boldsymbol{B}} = I_{\boldsymbol{C}} &= r_y q_y + r_z q_z + 2(r_y q_z + r_z q_y) \end{aligned}$$

The polarized "unit-vector" spectra can now be constructed by requiring that the absorption from both components sum up to one, i.e.: r_y=1-r$_z$ and r_z=1-r_y. Emission occurs at an angle β, which stands for differences between the TDMs defining the first and last light matter interaction in a TA-sequence induced by thermal fluctuation

$$\text{eq. S7} \qquad \begin{aligned} I_{\boldsymbol{A}} &= (2r_y + 1)\, q_y + (3 - 2r_y)\,(1 - q_y) = (3 - 2\, r_z)\,(1 - q_z) + (2\, r_z + 1)\, q_z \\ I_{\boldsymbol{B}} = I_{\boldsymbol{C}} &= (2 - r_y)\, q_y + (1 + r_y)\,(1 - q_y) = (1 + r_z)\,(1 - q_z) + (2 - r_z)\, q_z \end{aligned}$$

These expressions are inserted into the expression for the fundamental anisotropy r$_0$:

$$\text{eq. S8} \qquad \begin{aligned} r(\lambda{,}t) &= \frac{(I_A - I_B)}{(I_A + I_B + I_C)} = \frac{(I_A - I_B)}{(I_A + 2I_B)} \\ &= \tfrac{1}{5}\,[(3r_y - 1)\, q_y + (2 - 3\, r_y)\,(1 - q_y)] = \tfrac{1}{5}[(2 - 3\, r_z)\,(1 - q_z) + (3\, r_z - 1)\, q_z] \end{aligned}$$

Instead of setting $q_y = 1$ and $q_z = 0$ as ref 6-7, we set $q_y = \cos^2\beta$ and $q_z = \sin^2\beta$. Inserting these requirements into the relevant expressions yields:

$$\text{eq. S9} \qquad \begin{aligned} r_z &= \frac{3cos^2\beta - (2 - 5\cdot r(\lambda{,}t))}{3\cdot(2\cdot cos^2\beta - 1)} \\ r_y &= \frac{3cos^2\beta - (5\cdot r(\lambda{,}t) + 1)}{3\cdot(2\cdot cos^2\beta - 1)} \end{aligned}$$

The spectral "unit vectors" along *Y* and *Z* can hence be related directly to the experimentally determined anisotropy $r(\lambda{,}t)$.

Finally, the purely polarized spectra S_z and S_y can be extracted from the isotropic spectrum $(I_A + 2I_B)$ by projecting it on the appropriate axes using the expressions for the unit vectors above. Using the ordinary notation from polarized spectroscopy, indicating polarizer orientations as either vertical (V) or horizontal (H), the expressions for the purely polarized spectra are:

eq. S10
$$S_z = (S_{\parallel}(\lambda,t) + 2 \cdot S_{\perp}(\lambda,t)) \cdot \left(\frac{3cos^2\beta - (2 - 5 \cdot r(\lambda,t))}{3 \cdot (2 \cdot cos^2\beta - 1)}\right) = 3 \cdot MA \cdot \left(\frac{cos^2\beta - (1 - cos^2\theta)}{(2 \cdot cos^2\beta - 1)}\right)$$
$$S_y = (S_{\parallel}(\lambda,t) + 2 \cdot S_{\perp}(\lambda,t)) \cdot \left(\frac{3cos^2\beta - (5 \cdot r(\lambda,t) + 1)}{3 \cdot (2 \cdot cos^2\beta - 1)}\right) = 3 \cdot MA \cdot \left(\frac{cos^2\beta - cos^2\theta}{(2 \cdot cos^2\beta - 1)}\right)$$

Data analysis: Kinetics

All TA datasets were pre-analyzed by singular value decomposition (SVD) and analyzed by GLA[8] in OPTIMUS.[1] The fitted function includes a sum of 3 to 4 exponentials functions, as well as a combination of Gaussian and Gaussian derivatives to account for the coherent artefact. Evolution-associated spectra (EAS) are obtained based on a sequential kinetic model.

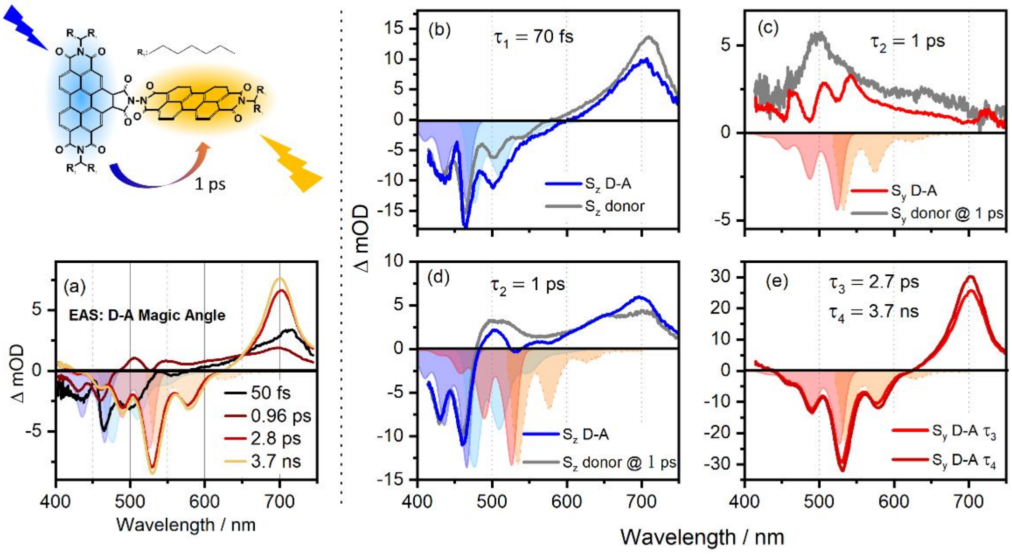

Figure S3 (a) Results from GLA of MA-TA data for **D-A.** **(b)** the sub-100 fs components of $S_{z-30°}$ retrieved from **D-A** (blue, solid) and **D** (grey, dash dot), **(c)** ~1 ps components of $S_{y-30°}$ for **D-A** (blue, solid) and **D** (grey, dash dot) **(d)** ~1 ps components of $S_{z-30°}$ for **D-A** (red, solid) and **D** (grey, dash dot), and **(e)** the ~ 2.8 ps component of $S_{y-30°}$ (red, solid) and the long-life time component (dark red, solid).

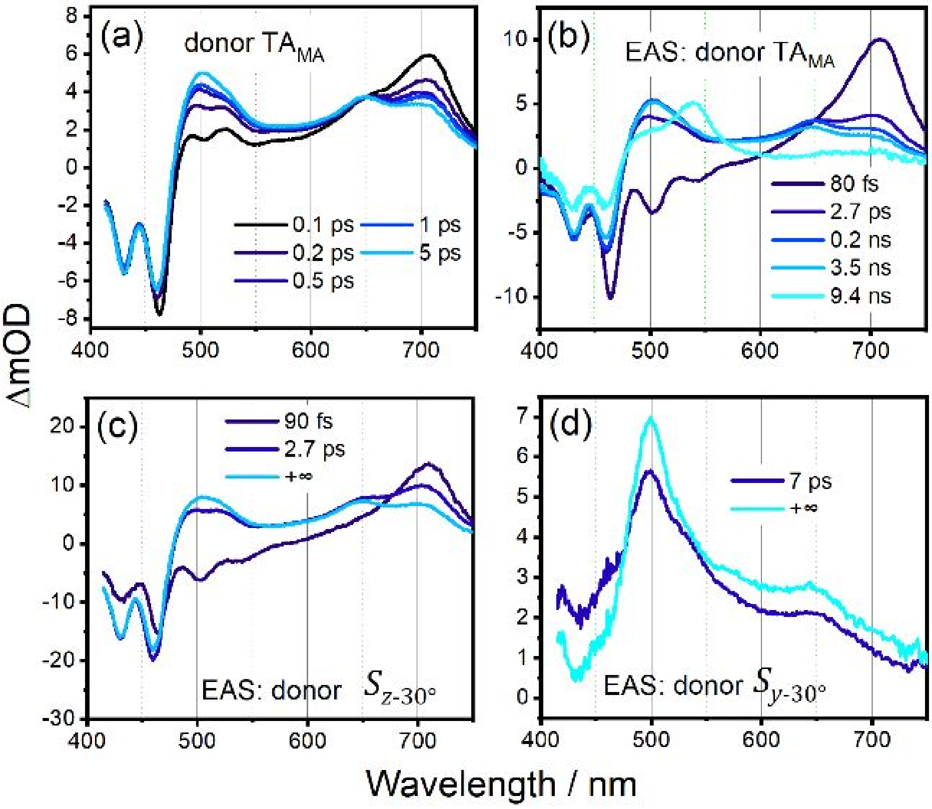

Figure S4 (a) Transient spectra of **D** at indicated delay times, and results from GLA of (b) MA-TA, (c) S_{z-30° and (d) S_{y-30° data for **D.**

Table S1 Time constant extracted by global lifetime analysis of MA spectra and corrected spectra of $S_{z-30^\circ}$and S_{y-30° of BPTI.

	TA$_{MA}$	$\boldsymbol{S_{z-30^\circ}}$	$\boldsymbol{S_{y-30^\circ}}$
$\boldsymbol{\tau_1}$ **sub-100 fs**	80 fs	90 fs	--
$\boldsymbol{\tau_2}$	2.7 ps	2.7 ps	7 ps*
$\boldsymbol{\tau_3}$*	0.2 ns *	--	--
$\boldsymbol{\tau_4}$	3.5 ns(f)	+∞	--
$\boldsymbol{\tau_5}$	9.4 ns (f)	--	+∞

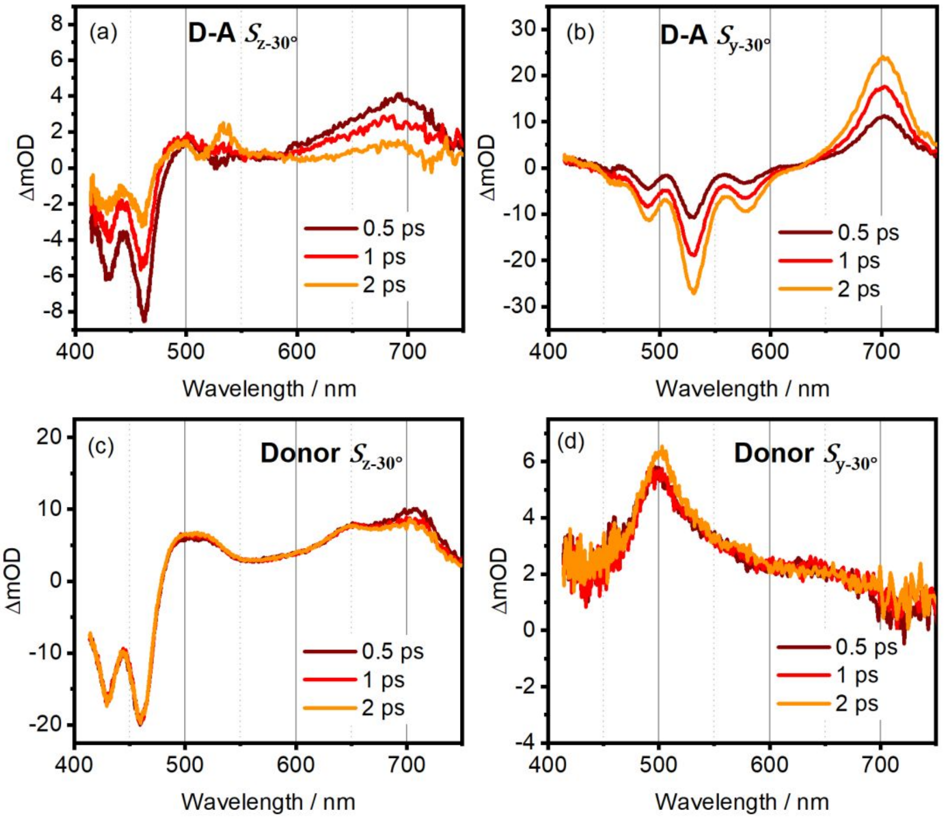

Figure 5 S_z and S_y spectra of **D-A** (top row, (a) and (b)) and **D** (bottom row, (c) and (d)) at 0.5, 1 and 2 ps pump-probe delay. All spectra shown at β values of 30°

QM and MD calculations

All QM calculations are performed using the Gaussian 16 quantum chemistry software.[9] Ground state geometries are optimized with the B3LYP DFT functional and 6-311G(d,p) basis set and the excited state calculations are performed with a long range corrected cam-B3LYP DFT functional[10] and 6-311G(d,p) basis set.[11] Solvent effects were included using a polarizable continuum model (PCM). For computing of the MO overlaps the geometry of the monomers was obtained from the dyad and the missing chemical bond was capped by a hydrogen atom.

Due to the small distance between the donor and acceptor moieties in **D-A** there exists the added possibility of the Dexter type excitation energy transfer.[12] Our computational results, however, indicate that the orthogonal TDMs arrangement of the individual moieties leads to negligible molecular orbital overlap, which is on the order of 4×10^{-4} and 5×10^{-4} for the HOMO and LUMO orbitals, respectively. Overlap between other relevant molecular orbitals is even lower. Such a small molecular orbital overlap yields negligible coupling constants, lower than 0.1 cm^{-1} for Dexter type energy transfer and therefore, even though the donor and acceptor moiety are only separated by a single chemical bond, the geometric arrangement of the moieties leads to negligible molecular orbital overlap and the absence of Dexter type energy transfer.

The orthogonal arrangement of the transition densities of the **D** and **A** in the optimal ground state geometry leads to negligible coupling between the individual moieties. However, the thermal motion of the dyad disrupts the

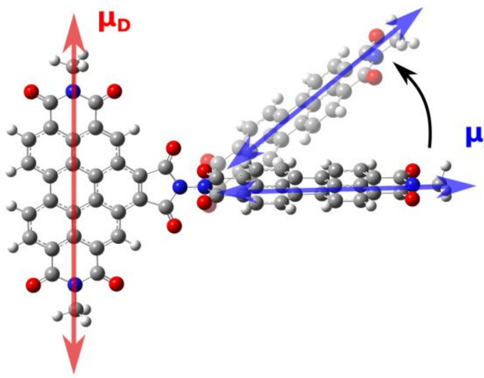

perfect orthogonal arrangement of the transition dipoles of the **D** and **A** moiety and induce coordinate dependent exciton coupling and hence also the excitation energy transfer as was already shown for the dyads with the benzene linker.[11] The major contribution to the coordinate dependent coupling originate from the bending motion of the dyad which leads to the non-orthogonal arrangement of the transition dipole moments of the **D** and **A** moiety. In order to estimate the effect of such molecular motion on the exciton coupling and resulting excitation energy transfer times, the **A** moiety was rotated around the center of the linker in plane defined by **D** moiety (**Figure S6**). For each conformation the transition dipoles were computed for **D** and **A** acceptor moiety separately and placed in the center of charge r_{COC} of each moiety. The center of charge was obtained from integration of the transition density as

eq. S11 $$r_{coc} = \frac{\int r|\rho_{ge}(r)|}{\int |\rho_{ge}(r)|dr},$$

where *r* is electron coordinate and $\rho_{ge}(r)$is the transition density between the ground and excited state. The exciton coupling *J* between **D-A** was then computed within the point transition dipole approximation as

eq. S12 $$J = \frac{1}{4\pi\epsilon_0} \frac{\mu_{ge}^{A} \cdot \mu_{ge}^{b}}{|r_{COC}^{A} - r_{COC}^{B}|^3} - 3\frac{\mu_{ge}^{A} \cdot (r_{COC}^{A} - r_{COC}^{B})\mu_{ge}^{B} \cdot (r_{COC}^{A} - r_{COC}^{B})}{|r_{COC}^{A} - r_{COC}^{B}|^5},$$

where μ_{ge}^{A} and $\mu_{ge}^{B}$are transition dipole moments of the acceptor and donor, respectively. The exciton couplings for different mutual angles between the transition dipoles of the **D** and **A** moieties can be found in the Table S2.

Figure S6 The bending motion of the D-A system leads to the non-orthogonal arrangement of the transition dipole moments of the **D** and **A** moiety

Förster energy transfer times estimation

We have recently calculated transfer rates in an ortho-dyad of the same chromophores yet with more distance between D and A, realized by a benzene spacer[11]. After comparing several theoretical approaches, quantitatively accurate estimates were only found only for costly MD/QC simulations, which properly sample both inter- and intra-molecular vibrational motions. In the present work, we limit our efforts to check that the couplings found in Ref [11] rescale correctly for closer arrangement of chromophores with no spacer. Förster energy transfer times were estimated by using the Eq. **(1)** in ref 13 and Eq. **(1)** in ref 14. Using a QM approach described in the previous section, we vary the relative TDM directions of D and A. Results on coupling constant and respective transfer time are shown in Table S2. For the ortho-FRET system including the benzene spacer, the observed EET-time of 9.4 ps, corresponding to an angle of 67°.[13] Applied to the present nullspacer dyad, the Förster rate is calculated to be 1.6 ps, see table S2. This compares well to our experimental finding of 0.96 ps . From other point of view the nullspacer lifetime correspond to 61° angle between donor and acceptor dipoles as reported in the main text. We conclude that both spectra and transport data qualitatively support the picture of Förster type of transport, but the estimate of orientation factor for Förster formula remains challenging.

Table S2 Förster energy transfer times of D-A system with and without benzene spacer estimated by dipole-dipole approximation. The coupling values obtained by MD method with different angle between TDMs of donor and acceptor.

Spacer	Angle between TDM of D and A / °	Coupling (dip-dip)/ cm^{-1}	Life time estimated / ps
Benzene	76	10.62	25.62
	72	13.68	15.44
	68	16.82	10.21
	64	20.07	7.17
	60	23.45	5.25
	56	27.00	3.96
	52	30.71	3.06
	48	34.65	2.41
Null	76	24.97	4.63
	72	32.61	2.72
	68	40.47	1.76
	64	48.60	1.22
	60	57.06	0.89
	56	65.93	0.66
	52	75.28	0.51
	48	85.18	0.40

REFERENCES

(1) Slavov, C.; Hartmann, H.; Wachtveitl, J. Implementation and Evaluation of Data Analysis Strategies for Time-Resolved Optical Spectroscopy. *Anal. Chem.* **2015,** *87* (4), 2328-36, DOI: 10.1021/ac504348h.

(2) Jonas, D. M.; Lang, M. J.; Nagasawa, Y.; Joo, T.; Fleming, G. R. Pump−Probe Polarization Anisotropy Study of Femtosecond Energy Transfer within the Photosynthetic Reaction Center of Rhodobacter Sphaeroides R26. *J. Phys. Chem.* **1996,** *100* (30), 12660-12673, DOI: 10.1021/jp960708t.

(3) Yeh, A. T.; Shank, C. V.; McCusker, J. K. Ultrafast Electron Localization Dynamics Following Photo-Induced Charge Transfer. *Science* **2000,** *289* (5481), 935-8, DOI: 10.1126/science.289.5481.935.

(4) Mewes, L.; Ingle, R. A.; Megow, S.; Böhnke, H.; Baranoff, E.; Temps, F.; Chergui, M. Ultrafast Intersystem Crossing and Structural Dynamics of [Pt (Ppy)(M-T Bu2pz)] 2. *Inorg. Chem.* **2020,** *59* (20), 14643-14653, DOI: 10.1021/acs.inorgchem.0c00902.

(5) Wallin, S.; Davidsson, J.; Modin, J.; Hammarstrom, L. Femtosecond Transient Absorption Anisotropy Study on [Ru(Bpy)3]2+ and [Ru(Bpy)(Py)4]2+. Ultrafast Interligand Randomization of the Mlct State. *J. Phys. Chem. A* **2005,** *109* (21), 4697-704, DOI: 10.1021/jp0509212.

(6) Thyrhaug, E.; Zidek, K.; Dostal, J.; Bina, D.; Zigmantas, D. Exciton Structure and Energy Transfer in the Fenna-Matthews-Olson Complex. *J. Phys. Chem. Lett.* **2016,** *7* (9), 1653-60, DOI: 10.1021/acs.jpclett.6b00534.

(7) Thyrhaug, E.; Sorensen, T. J.; Gryczynski, I.; Gryczynski, Z.; Laursen, B. W. Polarization and Symmetry of Electronic Transitions in Long Fluorescence Lifetime Triangulenium Dyes. *J. Phys. Chem. A* **2013,** *117* (10), 2160-8, DOI: 10.1021/jp312376k.

(8) Landl, G.; Langthaler, T.; Englt, H. W.; Kauffmann, H. F. Distribution of Event Times in Time-Resolved Fluorescence: The Exponential Series Approach—Algorithm, Regularization, Analysis. *J. Comput. Phys.* **1991,** *95* (1), 1-28, DOI: 10.1016/0021-9991(91)90250-O.

(9) Frisch, M. J.; Trucks, G. W.; Schlegel, H. B.; Scuseria, G. E.; Robb, M. A.; Cheeseman, J. R.; Scalmani, G.; Barone, V.; Petersson, G. A.; Nakatsuji, H., et al. *Gaussian 16 Rev. A.03*, Wallingford, CT, 2016.

(10) Yanai, T.; Tew, D. P.; Handy, N. C. A New Hybrid Exchange–Correlation Functional Using the Coulomb-Attenuating Method (Cam-B3lyp). *Chem. Phys. Lett.* **2004,** *393* (1-3), 51-57, DOI: 10.1016/j.cplett.2004.06.011.

(11) Slama, V.; Perlik, V.; Langhals, H.; Walter, A.; Mancal, T.; Hauer, J.; Sanda, F. Anharmonic Molecular Motion Drives Resonance Energy Transfer in Peri-Arylene Dyads. *Front. Chem.* **2020,** *8*, 579166, DOI: 10.3389/fchem.2020.579166.

(12) Dexter, D. L. A Theory of Sensitized Luminescence in Solids. *J. Chem. Phys.* **1953,** *21* (5), 836-850, DOI: 10.1063/1.1699044.

(13) Renger, T.; Dankl, M.; Klinger, A.; Schlucker, T.; Langhals, H.; Muh, F. Structure-Based Theory of Fluctuation-Induced Energy Transfer in a Molecular Dyad. *J. Phys. Chem. Lett.* **2018,** *9* (20), 5940-5947, DOI: 10.1021/acs.jpclett.8b02403.

(14) Langhals, H.; Dietl, C. Vibronic Intramolecular Resonant Energy Transfer Along More Than 5 Nm: Synthesis of Dyads for a Re-Examination of the Distance Function of Fret. *J. Org. Chem.* **2022,** *87* (15), 9454-9465, DOI: 10.1021/acs.joc.1c02682.

C. FULL LENGTH ARTICLE OF SECTION 4.2

Reprinted with permission from Xu, Y., Martin, T. P., Jänchen, M., Foja, R., Storch, G., Thyrhaug, E., de Vivie-Riedle, R., and Hauer, J., Determining Excited-State Absorption Properties of a Quinoid Flavin by Polarization-Resolved Transient Spectroscopy. *J. Phys. Chem. A*, **2024**.@ 2024 American Chemical Society.

The Supporting information is available free of charge, thus no reprint permission is necessary.

THE JOURNAL OF PHYSICAL CHEMISTRY A
A JOURNAL OF THE AMERICAN CHEMICAL SOCIETY

pubs.acs.org/JPCA
Article

Determining Excited-State Absorption Properties of a Quinoid Flavin by Polarization-Resolved Transient Spectroscopy

Yi Xu, Martin T. Peschel, Miriam Jänchen, Richard Foja, Golo Storch, Erling Thyrhaug, Regina de Vivie-Riedle, and Jürgen Hauer*

Cite This: J. Phys. Chem. A 2024, 128, 3830−3839

Read Online

ACCESS | Metrics & More | Article Recommendations | Supporting Information

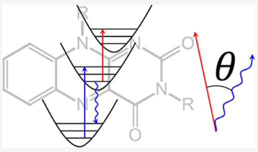

ABSTRACT: As important naturally occurring chromophores, photophysical/chemical properties of quinoid flavins have been extensively studied both experimentally and theoretically. However, little is known about the transition dipole moment (TDM) orientation of excited-state absorption transitions of these important compounds. This aspect is of high interest in the fields of photocatalysis and quantum control studies. In this work, we employ polarization-associated spectra (PAS) to study the excited-state absorption transitions and the underlying TDM directions of a standard quinoid flavin compound. As compared to transient absorption anisotropy (TAA), an analysis based on PAS not only avoids diverging signals but also retrieves the relative angle for ESA transitions with respect to known TDM directions. Quantum chemical calculations of excited-state properties lead to good agreement with TA signals measured in magic angle configuration. Only when comparing experiment and theory for TAA spectra and PAS, do we find deviations when and only when the $S_0 \rightarrow S_1$ of flavin is used as a reference. We attribute this to the vibronic coupling of this transition to a dark state. This effect is only observed in the employed polarization-controlled spectroscopy and would have gone unnoticed in conventional TA.

1. INTRODUCTION

Spectroscopy with polarized light is a versatile tool to disentangle congested regions of molecular absorption spectra and to provide insights into molecular structure. For example, circular dichroism is a standard method to determine the relative content of helical structures in proteins.[1] Linear dichroism is commonly employed to investigate the structural and orientational properties of molecules in different environments, e.g., to understand the alignment of biomolecules in biological membranes.[2−4] All polarization-resolved spectroscopic methods rely on the tensorial nature of transition dipole moments (TDMs) connecting initial and final molecular states. For linear and circular dichroism, the initial state is equivalent to the ground state. If the initial state is an electronically excited state, the probed TDM can connect to even higher-lying states, as found in excited-state absorption (ESA) transitions in transient absorption (TA) spectroscopy. Such information on excited-state TDMs is an important benchmark for modern advanced quantum mechanical approaches, such as multireference perturbation theory (CASPT2, NEVPT2), coupled-cluster theory (CC2, CC3, EOM-CC), or double-hybrid time-dependent density functional theory (DH-TDDFT).[5−9] However, experimental data on excited-state TDM directions are sparse at best. The most common approach relies on TA anisotropy (TAA), which is troubled by diverging signals if the underlying TA signals approach zero.[10,11] In this work, we employ polarization-associated spectra (PAS) as an extension of TAA, in which the problem of diverging signals is averted. We show how the PAS of a quinoid flavin sample lets us determine the relative TDM angles for all observed ESA transitions with respect to known directions of ground-state TDMs. We also show how transient spectra and TAA can be obtained from quantum chemical simulations using DH-TDDFT and compare the results to the experimental measurements.

Flavins are important naturally occurring chromophores in biology and play essential roles in various metabolic and enzymatic processes in living organisms.[12−14] They exhibit multiple redox and protonation states,[15] which allows them to participate in biochemical redox reactions as essential cofactors of many oxidoreductases.[16] Due to their absorption and emission properties,[17] flavins also serve as chromophores in several photoreceptors and light-responsive enzymes. These properties make flavins crucial in natural processes, such as DNA repair, cell apoptosis, signal transduction, and biological imaging.[16,18−22]

Photochemically excited flavin cofactors in flavin-dependent enzymes unlock a variety of synthetically interesting catalytic transformations.[23] In the organic laboratory, molecular flavins serve as versatile and easily modifiable catalysts.[24,25] Most catalytic applications use quinoid flavins as excited-state oxidants. The corresponding photocatalytic cycle starts with the excitation of the quinoid flavin in its ground state to the

Received: February 27, 2024
Revised: April 19, 2024
Accepted: April 25, 2024
Published: May 6, 2024

https://doi.org/10.1021/acs.jpca.4c01260
J. Phys. Chem. A 2024, 128, 3830−3839

singlet excited state ($^1\pi\pi^*$), followed by an intersystem crossing (ISC) to the photocatalytically active triplet state ($^3\pi\pi^*$) within several nanoseconds.[25−27] This efficient ISC process also explains the moderate fluorescence quantum yield of ∼30% at room temperature.[27−29] The triplet yield can be further enhanced via re-excitation of the initially excited singlet state.[30−32] The desire to drive such excited-state transitions efficiently underlines the importance of knowing the excited-state TDM directions.

Outside the fields of thermal and photodriven catalysis, Roth et al. studied quantum control systems based on flavins,[33] in which two nearly identical flavin molecules with subtle differences only in their side chains were excited by a phase-shaped 400 nm pulse. The molecules were distinguished by differences in fluorescence depletion by a subsequent 800 nm pulse. This again calls for an in-depth understanding of the excited-state properties of flavins, in particular the TDMs of flavin's various excited states.

Despite a large body of work on transient spectroscopy on flavins,[20,34,35] little is known about the TDM orientation of ESA transitions. Experimental approaches to this problem, based on TAA, have been reported in our earlier work.[36] Our approach uses TAA data to separate the TA spectra from isotropic samples into linearly independent—and more readily interpreted—spectral components, i.e., PAS.[37−39] In the present study, we employ this method to dissect the TA signal of a quinoid flavin in solution. Furthermore, we determine the relative angle between the TDMs of two neighboring ESA transitions. We isolate pure ESA signals from ground-state bleach (GSB) and stimulated emission (SE). By comparing to more conventional methods of extracting pure ESA signals, we highlight the advantages of our approach.

2. MATERIALS AND METHODS

2.1. Steady-State Spectroscopy. Linear absorption and emission experiments of the quinoid flavin (3,10-dibutylbenzo-[*g*]pteridine-2,4(3*H*,10*H*)-dione) (compound **1**, structure shown in Figure 1) were performed in *N*,*N*-dimethylformamide (DMF) in a 1 cm fused silica cuvette. The absorption spectra were recorded on a PerkinElmer Lambda 365 UV−vis spectrophotometer, while fluorescence and fluorescence anisotropy spectra were measured using an Edinburgh FS5 spectrofluorometer equipped with polarizer assemblies in both excitation and emission paths.

In all fluorescence measurements, the maximum optical density (OD) was kept below 0.05 in order to avoid inner filter effects. The sample for fluorescence anisotropy measurements was prepared in poly(tetrahydrofuran) (poly-THF, average M_n ≈ 2900, Aldrich chemistry). The polymer sample was kept close to the melting point at 30 °C with an electronic Peltier element in order to simultaneously maintain sufficiently high viscosity for the anisotropy measurements and solvent transparency. The fluorescence (excitation) anisotropy was calculated according to the standard formula as:[40]

$$r(\lambda_{\mathrm{ex}}) = \frac{F_{\mathrm{VV}}(\lambda_{\mathrm{ex}}) - F_{\mathrm{VH}}(\lambda_{\mathrm{ex}})}{F_{\mathrm{VV}}(\lambda_{\mathrm{ex}}) + 2\cdot F_{\mathrm{VH}}(\lambda_{\mathrm{ex}})} = \frac{2}{5}\cdot\frac{3\cos^2\theta - 1}{2} \qquad (1)$$

where F_{nm} is the recorded fluorescence intensity, with excitation and emission polarizer settings denoted by subscripts V (vertical) and H (horizontal). The relative angle θ between the excited and emission TDMs can be retrieved.

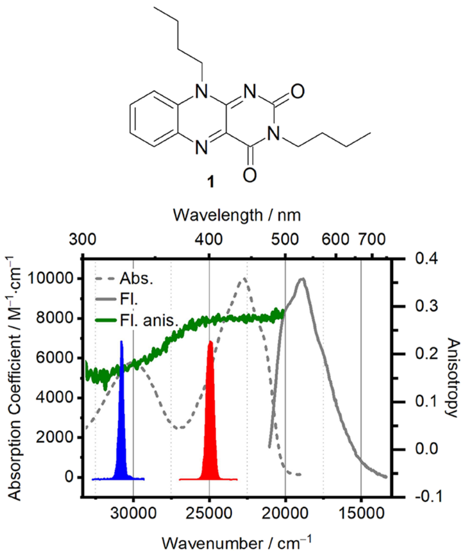

Figure 1. Upper panel shows the molecular structure of (3,10-dibutylbenzo[g]pteridine-2,4(3H,10H)-dione) of quinoid flavin (**1**) in DMF solution. The bottom panel shows the corresponding UV−vis absorption (gray dashed), fluorescence (gray solid, normalized to the strongest absorption peak), and fluorescence anisotropy spectrum (dark green solid). The red (blue) filled areas represent pump pulses at the two employed excitation wavelengths of 400 and 325 nm, respectively.

2.2. TA Spectroscopy. Femtosecond TA experiments were performed using a home-built TA setup detailed previously.[36] Briefly, a 5 kHz train of 800 nm, 36 fs fwhm laser pulses generated by a regenerative amplifier (Coherent Legend Elite Duo HE+) was divided into pump and probe arms. Two pump wavelengths, 400 and 325 nm, were chosen to selectively excite the $S_0 \rightarrow S_1$ and $S_0 \rightarrow S_3$ transitions (see Figure 1). The 400 nm excitation pump pulse was obtained via second harmonic generation (SHG) of the 800 nm fundamental pulse inside a 200 μm-thin beta-barium borate crystal (BBO, Bluebean Optical Tech Ltd.). The 325 nm UV pump is obtained by frequency doubling the output of a tunable noncollinear optical parametric amplifier (NOPA).[41] The NOPA was used to generate 12 nm pulses full width at half-maximum centered at 650 nm, with a resulting pulse duration of 38 fs as determined by SGH Frequency Resolved Optical Gating (SHG-FROG).[42] The 400 and 325 nm pump pulse durations were estimated to be 90 and 108 fs (fwhm), respectively, from fitting the instrument response function using the program package OPTIMUS1.[43] White light for probing was generated by focusing 4 μJ of 800 nm light into a translated 5 mm thick CaF_2 crystal. The white light was split into a probe part and a reference part. The probe pulse was focused into the sample by using a 150 mm focal length spherical mirror and the spot size is 30 μm. The probe spatially overlaps with the center of the pump and is recollimated after the sample by using an achromatic lens with a 75 mm focal length. The probe and reference laser pulses were detected using a home-built prism spectrometer in combination with a pair of high-speed CMOS linear array cameras (Glaz LineScan-I-Gen2, Synertronic Designs). All the measurements were performed in DMF solution at an optical density (OD) of 0.1 at the absorption maxima in a flow cuvette with 100 μm optical path length. For both 400 and 325 nm pump−probe measurements, the experiments were done by setting the pump and probe pulses orthogonal, parallel, and at a magic angle (MA) with each other by using a waveplate in the pump arm (300−470 nm $\lambda/2$ plate, B.Halle Nachfl. GmbH). Sketches of the 400 and 325 nm pump−probe setups can be found in Figures S2 and S3.

2.3. TA Anisotropy and PAS Calculation. TA spectra were recorded with excitation- and probe-pulse polarizations being either parallel ($S_{\parallel}(\lambda, t)$) or perpendicular ($S_{\perp}(\lambda, t)$) to each other. The TAA can be calculated as:[44−46]

$$r(\lambda, t) = \frac{S_{\parallel}(\lambda, t) - S_{\perp}(\lambda, t)}{S_{\parallel}(\lambda, t) + 2S_{\perp}(\lambda, t)} = \frac{2}{5}\cdot\frac{3\cos^2\theta - 1}{2} \tag{2}$$

where θ is the angle between the excited and detected TDMs. In analogy with the fluorescence anisotropy, $r(\lambda, t)$ provides useful structural information as it reports on relative angles between the initially excited and probed TDMs.[11] However, the interpretation of TAA data is less straightforward, in particular because the signal diverges whenever the denominator in eq 2, equal to three times the MA signal amplitude, approaches zero. PAS mitigates this problem.[36,47,48] PAS are projections of the isotropic TA spectrum into contributions that are either parallel (S_z) or orthogonal (S_y) to the TDM initially excited by the pump pulse. The expressions for these projections are given by

$$\begin{aligned} S_z &= (S_{\parallel}(\lambda, t) + 2\cdot S_{\perp}(\lambda, t))\cdot\left(\frac{3\cos^2\beta - (2 - 5\cdot r(\lambda, t))}{3\cdot(2\cdot\cos^2\beta - 1)}\right) \\ &= 3\cdot\mathrm{MA}\cdot\left(\frac{\cos^2\beta - (1 - \cos^2\theta)}{(2\cdot\cos^2\beta - 1)}\right) \end{aligned} \tag{3}$$

and

$$\begin{aligned} S_y &= (S_{\parallel}(\lambda, t) + 2\cdot S_{\perp}(\lambda, t))\cdot\left(\frac{3\cos^2\beta - (5\cdot r(\lambda, t) + 1)}{3\cdot(2\cdot\cos^2\beta - 1)}\right) \\ &= 3\cdot\mathrm{MA}\cdot\left(\frac{\cos^2\beta - \cos^2\theta}{(2\cdot\cos^2\beta - 1)}\right) \end{aligned} \tag{4}$$

The terms $\left(\frac{3\cos^2\beta - (2 - 5\cdot r(\lambda,t))}{3\cdot(2\cdot\cos^2\beta - 1)}\right)$ and $\left(\frac{3\cos^2\beta - (5\cdot r(\lambda,t) + 1)}{3\cdot(2\cdot\cos^2\beta - 1)}\right)$ are analogous to $r(\lambda, t)$, in which they report on the angle θ between pumped and probed TDMs, but are expressed in the frame of the molecule. The detailed derivation of the above expressions can be found elsewhere.[28] The coordinate system of the molecular frame is defined by the direction of the initially excited TDM, by convention set to be parallel to the z-axis. In eqs 3 and 4, angle β is introduced. β rotates the molecular-frame z-axis away from the originally excited TDM. Accordingly, setting β to zero leaves the initially excited TDM parallel to the z-axis and recovers the expressions used in earlier works.[47−49] Conceptually, this rotation by the angle β is useful as it alters how strongly the signal at a given wavelength projects into the PAS components given by eqs 3 and 4. For a spectrally isolated feature, the signal strength is minimized (maximized) in one PAS component exactly when β equals the angle θ between the initially excited TDM and the TDM being probed at the given wavelength. Importantly, the S_z/S_y-PAS will be free of diverging signals often encountered in TAA when the TA spectra show a zero-crossing (see eq 2 and ref 36).

2.4. Quantum Chemical Simulations and Modeling of the Spectra. Modeling EAS is a challenging task since it requires an accurate description of high-lying excited states. Thus, butyl side chains of the quinoid flavin **1** as depicted in Figure 1 were replaced by methyl groups to avoid extensive sampling due to high conformational flexibility. This change was found not to alter the electronic structure of **1** significantly. TDDFT using the range-separated hybrid functional ωB97-X-D3 was not able to predict bright states at the correct energy to explain the observed ESA features. However, using a range-separated double hybrid functional (SCS-ωPBEPP86),[50] bright states close to the observed ESA features were obtained. At the Franck−Condon point, these states match calculations at the DLPNO-STEOM-CCSD level. However, a solvent model for excited states was necessary to obtain the correct Stokes shift. As there is, currently, no implementation of such a model for DLPNO-STEOM-CCSD, this method could not be used for calculations away from the Franck−Condon point. Further discussions are hence based on calculations at the SCS-ωPBEPP86 level.

All quantum chemical calculations were performed using the ORCA 5.0 program package.[51] Minima of the ground state (S_0) and first excited state (S_1) were optimized using ωB97-X-D3/ma-def2-TZVP.[52] Excitation and emission energies at these points were calculated using the range-separated double-hybrid functional SCS-ωPBEPP86[50] with the aug-cc-PVTZ basis set. All calculations used a linear-response conductor-like polarizable continuum model (LR-CPCM) solvent model with DMF as the solvent. ESA and SE transitions are calculated at the optimized S_1 structure with the solvent model equilibrated to the first excited state. GSB transitions are calculated at the optimized S_0 structure with the solvent equilibrated to S_0. Detailed inputs to perform the calculations can be found in the Supporting Information.

Vibrational broadening was included in the calculated spectra on a semiclassical level. To this end, 250 samples were drawn from a Wigner distribution[53,54] centered at each of the optimized structures and excitation and/or emission energies for each sample were calculated. With these data in hand, a fit to the TA traces at 1 ps using three parameters (Gaussian width, redshift, relative emission intensity) was performed to model the experimental data. Accordingly, the excitation and emission energies from the Wigner distribution were convoluted with a Gaussian (σ = 0.093 eV), red-shifted by 0.110 eV, and emission intensities were scaled relative to absorption by a factor of 0.56. Finally, all absorption/emission intensities were scaled to match the respective intensities of the experimental MA spectra. Further details on the calculation of spectra for parallel and perpendicular polarizations of the pump and probe pulses can be found in the Supporting Information.

3. RESULTS AND DISCUSSION

3.1. Absorption and Fluorescence Spectroscopy. A simplified flavin chromophore was chosen for this study in order to obtain experimental data as close as possible to the calculated data. The *N*3,*N*10-disubstituted flavin **1** serves this purpose, while the two butyl substituents ensure solubility. We show the steady-state absorption (gray dashed line) and emission spectra (gray solid line) of DMF solutions of **1** in TDM representation[55,56] in Figure 1, in which we correct the absorption spectrum by dividing the first power of the wavenumber and the emission spectrum by the third.[55] The absorption spectrum of **1** exhibits two broad absorption features in the UV/vis range, with peaks at 440 nm (22,727 cm^{-1}, $S_0 \rightarrow S_1$) and 330 nm (30,303 cm^{-1}, $S_0 \rightarrow S_3$). There is evidence for an optically dark $n\pi^*$ state (S_2) between these two bands.[27,29,35] The shape and central wavelength of the two absorption peaks are in agreement with previous works.[34,57−60] The determined molar extinction coefficients of 10,000 and 8000 M^{-1} cm^{-1} are in good agreement with literature values for flavin in aprotic solvents.[34,61] The 1300 cm^{-1} vibronic progression observed in both absorption and emission corresponds largely to C−C and C−N stretching and bending vibrations of the isoalloxazine ring.[62] The fluorescence spectrum peaks around 530 nm (18,868 cm^{-1}) and shows good mirror image symmetry with the absorption.

Thus, the lowest energy absorption and emission involve the same electronic state, S_1. Figure 2 shows the density difference associated with the transitions in the observed spectral range. The $S_0 \rightarrow S_1$ transition is associated with a redistribution of electrons inside the π system along the long axis of the molecule. The third excited singlet state, S_3, is also of $\pi\pi^*$ character and forms the second band centered at 330 nm. In contrast, $S_2(n\pi^*)$ is symmetry forbidden, as it redistributes electron density from the π system toward the oxygen lone pairs outside the ring (σ symmetry). However, the vibronic coupling of this state to its neighbors likely influences the observed line shapes.[29,35]

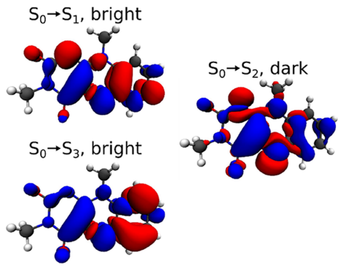

Figure 2. Density differences for the relevant to the static absorption spectrum, GSB, and SE transitions of the quinoid flavin (isovalue: 0.001) were calculated using ωPBEPP86[50]/aug-cc-PVTZ. Electron density is shown in red, and hole density is shown in blue.

The excitation fluorescence anisotropy of **1**, calculated according to eq 1, is superimposed on the spectra in Figure 1 as a dark green solid line. $r(\lambda)$ reaches a maximal value of ~0.28 at the red edge of the absorption spectrum. This failure to reach the limiting value of 0.4 implies substantial rotation of the TDM upon excitation, resulting in an effective angle of ~27° between the relevant TDMs for absorption and emission.[29] The anisotropy of the $S_0 \rightarrow S_3$ transition at 330 nm is similarly low, reaching a value of only 0.15—corresponding to an effective angle θ of 40°. We thus determine the angle between $S_0 \rightarrow S_1$ and $S_0 \rightarrow S_3$ to 13°, in good agreement with the 20 ± 5° value from earlier theoretical[63] and experimental studies.[29]

3.2. Magic Angle TA Spectroscopy: Experiment and Simulation.

In Figure 3, we show selected MA TA spectra of **1** after excitation at 400 (panel a) and 325 nm (panel b). The spectral structure and dynamics observed here are in good agreement with previously reported results.[60,64] For both employed excitation wavelengths, the negative signals at 440 and 530 nm can be attributed to GSB and SE, respectively. Inverted absorption (light blue-filled) and fluorescence (light red-filled) spectra are shown for comparison. Positive-valued ESA features overlap with the GSB and SE over most of the UV/vis spectral range, resulting in three distinct positive bands: sub-400 nm, at 478 nm, and above 600 nm. We refer to these as UV-ESA, blue-ESA, and red-ESA in the following but exclude the UV-ESA from further discussion, as we only detect its red edge. The dynamics after 400 and 325 nm excitation are compared in Table 1. Employing a global kinetic analysis scheme,[65] we obtain three lifetime components (see Table 1, the corresponding evolution-associated spectra are shown in Figure S5). We note that the overall shape and dynamics of the TA spectra for 325 nm excitation (excitation to S_3) and 400 nm excitation (excitation to S_1) are similar and the deactivation dynamics show no relevant dependence on excitation wavelength. Thus, to explain the observed similarities there has to be ultrafast internal conversion between S_3 and S_1, likely mediated by the dark S_2 state on a few-femtosecond time scale. Accordingly, conical intersections between S_3 and S_2 as well as S_2 and S_1 were found close to the Franck−Condon region (see Supporting Information Sections 8−11). The observed components with lifetimes τ_1 and τ_2 are associated with structural relaxation and -most likely- solvation dynamics of S_1. The shorter lifetime for this component after 325 nm excitation is explained by the increased excess energy after internal conversion to S_1.[35,57,66] The long-lived component τ_3 is consistent with the fluorescence lifetime of **1**, which was determined to be 5.7 ns in an independent time-correlated single-photon counting measurement.

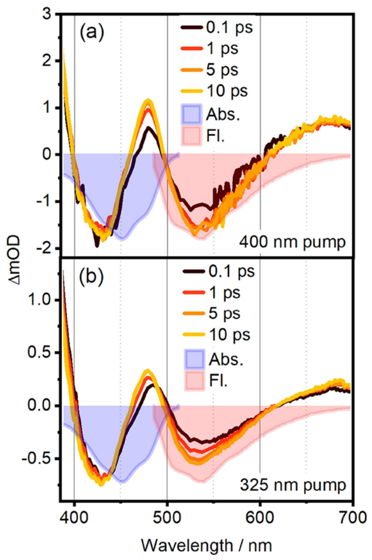

Figure 3. TA spectra slices at 0.5, 1, 5, and 10 ps for (a) 400 and (b) 325 nm pump. The light blue (light red) filled curves are the absorption/fluorescence spectra of quinoid flavin with inverted signs.

Table 1. Time Constants for 1 Extracted by Global Lifetime Analysis of MA TA Spectra Pumped by 400 and 325 nm (Evolution-Associated Spectra Are Shown in Figure S5a,b)[a]

	400 nm	325 nm
τ_1	200 fs	170 fs
τ_2	19.5 ps	4.7 ps
τ_3	+∞	+∞

[a] The long-lived component τ_3 stems from the 5.7 ns fluorescence lifetime of **1**, which is not resolved in the TA delay time window.

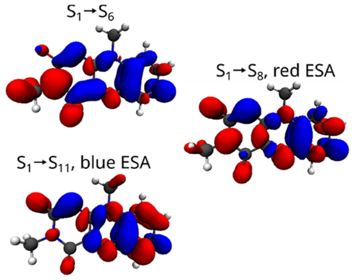

Figure 4. Bright transitions contributing to the ESA with nomenclature (“red ESA”, “blue ESA”) from Section 3.2. See Figure 2 legend and associated discussion for details.

Figure 4 illustrates the density differences associated with the ESA transitions. The numbering of the final states depends significantly on the quantum chemical method and the geometry. The state-ordering is presented here for SCS-ωPBEPP86/aug-cc-PVTZ at the S_1 minimum, the characters of the bright states are, however, consistent with calculations at the DLPNO-STEOM-CCSD level of theory. Due to symmetry, three states of $\pi\pi^*$ character form the main contribution to the observed ESA signal. The $S_1 \to S_6$ and $S_1 \to S_8$ transitions contribute to the red ESA and the $S_1 \to S_{11}$ transition to the blue ESA. Of these transitions, $S_1 \to S_{11}$ and $S_1 \to S_6$ are polarized along the long axis of the molecule, while $S_1 \to S_8$ is polarized along the short axis of the molecule. The full MA signal calculated from the Wigner sampling is displayed in Figure 5a, together with the experimental signal at 1 ps.[53,54] The overall agreement of the calculated and measured signals is excellent. The maximum of the ESA (blue line) in the blue region is due to the $S_1 \to S_{11}$ transition which has the highest oscillator strength of all the ESA transitions. $S_1 \to S_6$ and $S_1 \to S_8$ form a tail toward the red edge of the spectrum that overlaps with the SE and forms the red ESA band. As the Wigner distribution contains nonsymmetric structures, many other states also contribute, leading to a broad total ESA signal.

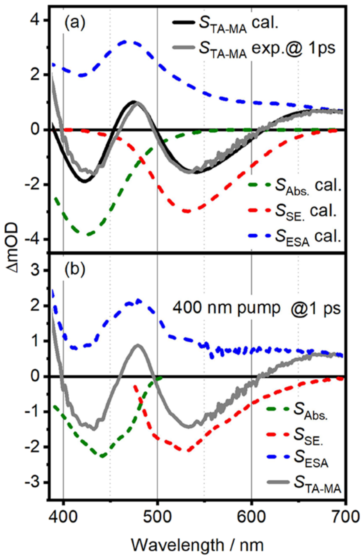

Figure 5. (a) TA slice at 1 ps for 400 nm pump (gray), compared to calculated TA (black). The dashed lines indicate the GSB (dark green), SE (red), and ESA (blue) contributions to the calculated signal. The fit of the calculated signal to the experimental data is discussed in the main text. (b) Pure ESA spectrum (blue dashed) calculated according to eq 5. The components entering eq 5 are the total TA signal (gray solid) at 1 ps delay time, and the scaled absorption (dark green dashed) and SE spectrum (red dashed).

To validate the simulation results, we employ a commonly used approach to isolate pure ESA spectra. We apply the following expression:

$$S_{ESA} = S_{TA} - N_a \cdot S_{Abs.} - N_{SE} \cdot S_{SE} \tag{5}$$

where S_{ESA}, $S_{Abs.}$, S_{SE}, and S_{TA} are the pure ESA spectrum, absorption spectrum, SE spectrum—approximated as the fluorescence spectrum in the TDM representation—and TA spectrum, respectively. N_a and N_{SE} represent scaling factors for GSB and SE, respectively, N_a is obtained via the calculated excitation probability, defined by the pump fluence and the overlap between the pump and absorption spectrum.[67] The ratio of N_a and N_{SE} was set to 1.07 to ensure that the pure ESA signal at 560 nm is positive.

The extracted pure ESA spectrum at 1 ps pump−probe delay, and 400 nm excitation is shown as the gray solid line in Figure 5b. The according spectra for 325 nm pumping (not shown) are qualitatively similar. The ESA spectrum exhibits only positive values as expected and consists of a shoulder below 400 nm (UV-ESA), a peak centered at 480 nm (blue-ESA), and a broad red feature above 610 nm (red-ESA). As evident from the discussion of eq 5, the most questionable assumption behind this approach is equating the SE spectrum with the fluorescence spectrum in TDM representation. Any SE from unrelaxed excited states will lead to uncertainties in the obtained ESA spectra. Furthermore, no information on the relative angle between the observed excited-state transitions can be obtained. Anisotropy-based approaches provide elegant solutions to these problems. Takaya et al.[68] resolved the spectral components for two overlapping species by applying eqs S1 and S2 (see Supporting Information) to isolate two components with different initial anisotropy values (see Figure S6).

As apparent from Figure 5, the qualitative agreement between experiment and simulation is very good with respect to pure ESA features, considering the uncertainties discussed in the previous section. In an effort to arrive at a more quantitative comparison for excited-state properties, we resort to relative angles between TDMs. An established way of getting to this information is measuring TAA spectra as discussed in the next section. The relation between anisotropy and relative angles is again given by the standard expression (see eq 2).

3.3. TA Anisotropy. In Figure 6a,b, we show TAA slices at 1 ps after excitation at 400 (red full line) and 325 nm (blue), respectively. These spectra represent the relation between transition dipoles well since diffusional depolarization is minimal at such short time scales (see Figure S4). The spectra diverge at wavelengths of zero-crossings in the TA spectrum, indicated by the gray-shaded area. The TAA spectra for 400 and 325 nm excitation are offset from each other due to their initially excited TDMs being nonparallel (see Figure 1). Quantitatively, there are significant differences between the calculated and measured anisotropies. As illustrated by a comparison between Figure 6a,b, the simulated anisotropies are much closer to the experiment in the case of 325 nm excitation. As the only difference in the simulation of these two spectra is the TDM directions of the absorbing states S_1 and S_3

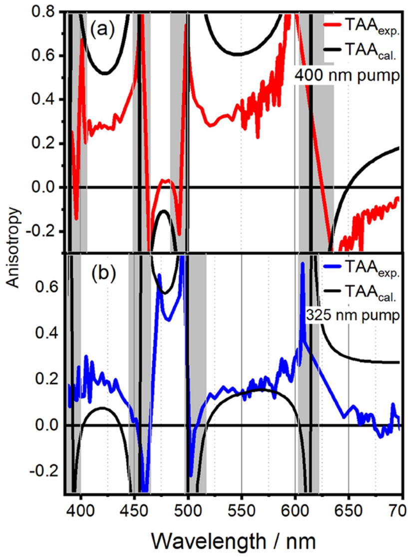

Figure 6. TA anisotropies of **1** with (a) 400 nm pump and (b) 325 nm pump. Experimental anisotropies are shown in red for 400 nm excitation and blue for 325 nm excitation, calculated anisotropies are shown in black. Experimental anisotropies are given for a pump−probe delay of 1 ps.

at the Franck−Condon point, there has to be a source of error that predominantly affects S_1 in the Franck−Condon region.[66] Due to the presence of an S_1−S_2 conical intersection in the Franck−Condon region, excitation at 400 nm leads to a wavepacket composed of vibronic states that are a mixture of $S_1(\pi\pi^*)$ and the dark $S_2(n\pi^*)$.[66] This mixing apparently alters significantly the TDM direction. These vibronic coupling effects are not reproduced without an explicit treatment of the excited-state dynamics of the system.[53,54] Accordingly, our model fails to reproduce the depolarization of the S_1 state (see also Figure 1, green line), i.e., the 27° rotation between the absorbing and emitting dipoles. Two other factors should also be considered: first, there are known, significant solvent influences on the excited states of flavins,[35,69,70] which also show up in our simulations as an inability to capture the Stokes shift without an appropriate solvent model. Changes in nontrivial solvent interactions that are not captured by a continuum model might lead to a rotation of the effective transition dipole moment of a solvent−solute complex upon relaxation. Such a mechanism has been proposed previously by Weigel et al.,[66] who suggest that solvent rearrangement is coupled to $n\pi^*/\pi\pi^*$ interconversion. Finally, for the DH-TDDFT functional used in this work, energies are expected to be of higher accuracy than TDMs. Especially, the CIS(D) correction used in the double-hybrid part of the functional applies only to the excitation energies; TDMs are only of hybrid TDDFT quality.

We note that the above discussion on the possible role of vibronic coupling in S_1 would not have been possible based on the simulation of TA spectra alone (see Figure 5), where the agreement between measured data and simulation was satisfactory. Only the analysis of TAA data in Figure 6 reveals the underlying discrepancy between the experiment and TDDFT-based theory. To investigate this matter further based on an easily quantifiable observable, we now turn to the relative angle between TDMs. The latter can in principle be calculated from TAA data using eq 2. However, this approach requires separated spectral components; if at a given detection wavelength two or more spectral species overlap, their values for $r(\lambda, t)$ will add up. This problem is addressed by using PAS in the subsequent section.

3.4. Polarization-Associated Spectra. In the following section, we will show that PAS delivers the angle of the TDM directions by increasing β. The first step in the PAS approach is to calculate S_z and S_y according to eqs 3 and 4 with coordinate-system rotation angle β set to zero. In the case of **1** studied here, we found poor separation in PAS for both pump wavelengths, with essentially all signals contributing in both PAS components (see Figure S7). In other words: for $\beta = 0$, there are no spectral features that would be minimized (maximized) in neither S_z nor S_y, meaning that the PAS approach does not bring new insights for the chosen value of $\beta = 0$. The fluorescence anisotropy data in Figure 1 already imply an angle $\theta = 27°$ between excitation and emission TDM as a useful starting point for β. Setting $\beta = \theta = 27°$ for 400 nm pump wavelength should hence maximize SE-contributions in $S_{z-27^\circ}^{400\ \mathrm{nm}}$, where the superscript denotes the pump wavelength. The corresponding PAS is shown in Figure 7a, blue line. We see a clear enhancement of both GSB and SE contributions in $S_{z-27^\circ}^{400\ \mathrm{nm}}$ compared to TA-MA, see blue vs gray line in Figure 7a. We note that PAS exhibit smooth signals over a broad detection range, which is an important advantage of TAA and its diverging signals (see Figure 5). This means that PAS allows for global (target) analysis (GTA), shown for PAS and TA-MA in Figure S5.

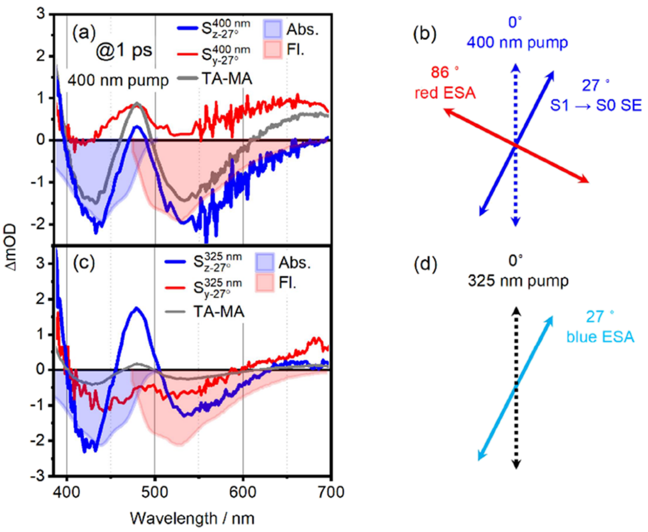

Figure 7. (a) PAS for 400 nm excitation. The $S_{z-27^\circ}^{400\ \mathrm{nm}}$ component (blue) optimizes the SE component with respect to the MA TA spectrum (dark gray). Panel (b) sketches the resulting TDM directions. (c) PAS for 325 nm excitation and $\beta = 27°$, emphasizing the blue ESA peaking at 480 nm. The resulting TDM directions are sketched in (d).

For easier identification of GSB and SE signals, we add the absorption (blue-filled area) and fluorescence spectrum (red-filled area). The fact that the GSB signal can be enhanced by a change of β implies that there is an ESA feature at the same detection wavelength but with a different TDM direction. Accordingly, the $S_{y-27^\circ}^{400\ \mathrm{nm}}$ PAS (red line) shows ESA signals in the spectral region where $S_{z-27^\circ}^{400\ \mathrm{nm}}$ exceeds the TA-MA signal. We note that $S_{y-27^\circ}^{400\ \mathrm{nm}}$ is positive throughout the entire detection window. Between 380 and 530 nm, there is good overlap between the pure ESA signal and $S_{y-27^\circ}^{400\ \mathrm{nm}}$. The pure ESA signal

Table 2. Comparison of Angles between Each Transition Obtained by Experimental Method and Theoretical Calculation

TDM_1	TDM_2	experimental method	θ_{1-2} exp.	θ_{1-2} calc.
$S_0 \rightarrow S_3$	$S_0 \rightarrow S_1$	fl. anis. and 325/400 nm pumped PAS	13°	33°
$S_1 \rightarrow S_0$ (SE)	$S_1 \rightarrow S_8$ (red ESA)	400 nm pumped PAS	86°	83°
$S_0 \rightarrow S_3$	$S_1 \rightarrow S_0$ (SE)	fl. anis in combination with 400 nm pumped PAS	40°	35°
$S_0 \rightarrow S_3$	$S_1 \rightarrow S_{11}$ (blue-ESA)	325 nm pumped PAS	27°	4.9°
$S_0 \rightarrow S_3$	$S_1 \rightarrow S_8$ (red-ESA)	325 nm pumped PAS	55°	62°

is discussed in Figure 5 and shown as a dotted line in Figure 7a. The red-ESA for detection wavelengths longer than 530 nm is enhanced beyond the level of the pure ESA signal in $S^{400\ \mathrm{nm}}_{y-27^\circ}$. Furthermore, the red-ESA is completely missing in $S^{400\ \mathrm{nm}}_{z-27^\circ}$, as this component overlaps perfectly with the fluorescence spectrum between 530 and 700 nm (see Figure 7a, red filled area). This leads us to the conclusion that the TDM of the red-ESA must be nearly orthogonal to the TDM of the SE. The latter is at 27° with respect to the ground-state transition at 400 nm, as determined by fluorescence anisotropy, see Figure 1. We summarize these findings pictorially in Figure 7b. As compared to TAA and its diverging signals (see Figure 6).

We found $\beta = 31^\circ$ is the best-suited value for minimizing the red-ESA in $S^{400\ \mathrm{nm}}_{z-31^\circ}$ (see Figure S9a), which gives us an 86° angle between the TDM of the red-ESA and SE. The blue-ESA transition, peaking at 480 nm, does not lend itself to such a straightforward assignment, as it is observable both in $S^{400\ \mathrm{nm}}_{z-27^\circ}$ and $S^{400\ \mathrm{nm}}_{y-27^\circ}$. Given the strong spectral congestion in this wavelength range, we refrain from determining the TDM angle of the blue-ESA via its relative contribution to $S^{400\ \mathrm{nm}}_{z-27^\circ}$ and $S^{400\ \mathrm{nm}}_{y-27^\circ}$. Instead, we find the strongest enhancement of the blue-ESA signal at $\beta = 27^\circ$ after 325 nm excitation. The respective spectra are shown in Figure 7c (We note that the correspondence between the values of β in Figure 7a,c is coincidental). The $S^{325\ \mathrm{nm}}_{z-27^\circ}$ PAS, shown in blue in Figure 7c, shows strong enhancement of the blue-ESA peaking at 480 nm in comparison to the TA-MA spectrum. More importantly, the corresponding $S^{325\ \mathrm{nm}}_{y-27^\circ}$ PAS lacks any ESA feature at 480 nm, as $S^{325\ \mathrm{nm}}_{y-27^\circ}$ shows good overlap between the absorption and SE spectrum in this region (see red vs filled blue and red curve). Hence, we can conclude that the blue-ESA's TDM has a 27° angle with respect to the TDM of the 325 nm transition. This scenario is depicted in Figure 7d.

Knowing the angle between the TDM of $S_0 \rightarrow S_3$ (325 nm) and the TDM of $S_0 \rightarrow S_1$ (400 nm) to be 13° (see Figure 1), we can deduce the angle between the TDMs of the 400 nm transition and the TDM of the blue-ESA to be 13° + 27° = 40°. An angle so close to 45°, where the PAS components in eqs 5 and 6 become degenerate, explains why we were unable to find a value for β to maximize the blue-ESA while minimizing GSB or SE signals. The red-ESA can be minimized when $\beta = 35^\circ$, as can be seen in $S^{325\ \mathrm{nm}}_{y-35^\circ}$ at 700 nm (see Figure S9b). This indicates that the angle between the red-ESA and the $S_0 \rightarrow S_3$ TDMs is 55°. The comparison of angles between TDMs obtained experimentally and theoretically are listed in Table 2.

The theoretically calculated angles between $S_1 \rightarrow S_0$ (SE) and $S_1 \rightarrow S_8$ (red ESA), $S_0 \rightarrow S_3$ and $S_1 \rightarrow S_0$, as well as $S_0 \rightarrow S_3$ and $S_1 \rightarrow S_8$ are 83, 35, and 62°, respectively, which are in good agreement with our experimental results. However, there are nonnegligible discrepancies (20°) in the angles when comes to $S_0 \rightarrow S_1$ and $S_1 \rightarrow S_{11}$ (blue-ESA). The deviation concerning $S_0 \rightarrow S_1$, as we mentioned in 3.1, can be explained by vibronic coupling of S_1 to the neighbor dark state S_2. Similarly, the presence of dark states energetically close to S_{11} can also influence the TDM orientation of $S_1 \rightarrow S_{11}$. Furthermore, the relatively high energy of the S_{11} state (4.92 eV or 39,683 cm^{-1}) can also be the source of the observed inaccuracies of TDM calculations.

4. CONCLUSIONS

We employ polarization-resolved transient spectroscopy to reveal new insights into quinoid flavin. While there is good agreement between magic angle TA and simulations (see Figure 5), polarization-resolved spectra show intriguing differences. We explain them by vibronic coupling between the S_1 state and the optically dark S_2 state. As a result, all TDMs involving the S_1 state deviate from experimental results, while there is a good agreement for all other transitions, as summarized in Table 2. In other words, our polarization-resolved approach highlights the influence of vibronic coupling, which would have remained hidden in conventional TA spectroscopy. This makes polarization-controlled spectroscopy an insightful method to benchmark the prediction of transition dipole moment directions by quantum chemical methods for electronic excited states. On a broader scope, our findings have the potential to facilitate and inspire advanced photocatalytic strategies, in which the re-excitation of excited states increases the catalyst's redox potential.[71] Knowing the relative angle between TDMs will allow for optimizing the yield of the re-excitation process.

■ ASSOCIATED CONTENT

Supporting Information

The Supporting Information is available free of charge at https://pubs.acs.org/doi/10.1021/acs.jpca.4c01260.

> Experimental details, evolution-associated spectra, Red-ESA disentanglement, transient anisotropy spectra time traces, PAS for $\beta = 0^\circ$, minimizing Red-ESA, calculation of polarized spectra and anisotropies, ORCA 5.0 inputs, coordinates of optimized structures of (3,10-dimethylbenzo[*g*]pteridine-2,4(3*H*,10*H*)-dione, calculated (transient) absorption energies and transition dipoles at the minima (PDF)

■ AUTHOR INFORMATION

Corresponding Author

Jürgen Hauer − *TUM School of Natural Sciences, Department of Chemistry and Catalysis Research Center, Technical University of Munich, 85748 Garching, Germany;*
orcid.org/0000-0002-6874-6138;
Email: juergen.hauer@tum.de

Authors

Yi Xu − *TUM School of Natural Sciences, Department of Chemistry and Catalysis Research Center, Technical University of Munich, 85748 Garching, Germany;*
orcid.org/0000-0003-4723-6312

Martin T. Peschel − *Department of Chemistry, Ludwig-Maximilians-Universität München, 81377 München, Germany;* orcid.org/0000-0001-5075-8555
Miriam Jänchen − *TUM School of Natural Sciences, Department of Chemistry and Catalysis Research Center, Technical University of Munich, 85748 Garching, Germany;* orcid.org/0009-0005-1859-6361
Richard Foja − *TUM School of Natural Sciences, Department of Chemistry and Catalysis Research Center, Technical University of Munich, 85748 Garching, Germany*
Golo Storch − *TUM School of Natural Sciences, Department of Chemistry and Catalysis Research Center, Technical University of Munich, 85748 Garching, Germany;* orcid.org/0000-0002-6747-3035
Erling Thyrhaug − *TUM School of Natural Sciences, Department of Chemistry and Catalysis Research Center, Technical University of Munich, 85748 Garching, Germany;* orcid.org/0000-0001-8634-9606
Regina de Vivie-Riedle − *Department of Chemistry, Ludwig-Maximilians-Universität München, 81377 München, Germany;* orcid.org/0000-0002-7877-5979

Complete contact information is available at:
https://pubs.acs.org/10.1021/acs.jpca.4c01260

Notes

The authors declare no competing financial interest.

■ ACKNOWLEDGMENTS

Y.X., M.T.P., R.d.V.-R., R.F., G.S., and J.H. acknowledge funding by the Deutsche Forschungsgemeinschaft (DFG, German Research Foundation)—TRR 325 (projects B7, B8, C5) and 514636421. J.H. acknowledges funding by DFG under Germany's Excellence Strategy-EXC 2089/1−390776260. R.F. thanks the Studienstiftung des Deutschen Volkes for a Ph.D. fellowship. G.S. thanks the DFG for support through the Emmy Noether Programme (STO 1175/3-1). Martin T. Peschel thanks Maximilian Lloyd Ach for initial exploratory calculations on the flavins.

■ REFERENCES

(1) Nordén, B.; Rodger, A.; Dafforn, T. *Linear dichroism and circular dichroism: a textbook on polarized-light spectroscopy*; RSC Publishing: Cambridge, UK, 2010.

(2) Daviter, T.; Chmel, N.; Rodger, A., Circular and linear dichroism spectroscopy for the study of protein−ligand interactions. In *Protein-ligand interactions: methods and applications*, 2013; 211−241.

(3) Norden, B.; Lindblom, G.; Jonas, I. Linear dichroism spectroscopy as a tool for studying molecular orientation in model membrane systems. *J. Phys. Chem.* **1977**, *81* (22), 2086−2093.

(4) Johansson, L. B.-Å. Analysis and application of linear dichroism on membranes. Description of a linear-dichroism spectrometer. *J. Chem. Soc., Faraday Trans. 1* **1985**, *81* (6), 1375−1388.

(5) Mester, D.; Kállay, M. Charge-transfer excitations within density functional theory: How accurate are the most recommended approaches? *J. Chem. Theory Comput.* **2022**, *18*, 1646−1662.

(6) Sarkar, R.; Loos, P.-F.; Boggio-Pasqua, M.; Jacquemin, D. Assessing the performances of CASPT2 and NEVPT2 for vertical excitation energies. *J. Chem. Theory Comput.* **2022**, *18* (4), 2418−2436.

(7) Kurashige, Y.; Chalupský, J.; Lan, T. N.; Yanai, T. Complete active space second-order perturbation theory with cumulant approximation for extended active-space wavefunction from density matrix renormalization group. *J. Chem. Phys.* **2014**, *141* (17), No. 174111.

(8) Dutta, A. K.; Nooijen, M.; Neese, F.; Izsák, R. Exploring the accuracy of a low scaling similarity transformed equation of motion method for vertical excitation energies. *J. Chem. Theory Comput.* **2018**, *14* (1), 72−91.

(9) Loos, P.-F.; Lipparini, F.; Boggio-Pasqua, M.; Scemama, A.; Jacquemin, D. A mountaineering strategy to excited states: Highly accurate energies and benchmarks for medium sized molecules. *J. Chem. Theory Comput.* **2020**, *16* (3), 1711−1741.

(10) Andersson, P. O.; Gillbro, T. Photophysics and dynamics of the lowest excited singlet state in long substituted polyenes with implications to the very long-chain limit. *J. Chem. Phys.* **1995**, *103* (7), 2509−2519.

(11) Wallin, S.; Davidsson, J.; Modin, J.; Hammarström, L. Femtosecond transient absorption anisotropy study on [Ru (bpy) 3] 2+ and [Ru (bpy)(py) 4] 2+. Ultrafast interligand randomization of the MLCT state. *J. Phys. Chem. A* **2005**, *109* (21), 4697−4704.

(12) Romero, E.; Gómez Castellanos, J. R.; Gadda, G.; Fraaije, M. W.; Mattevi, A. Same substrate, many reactions: Oxygen activation in flavoenzymes. *Chem. Rev.* **2018**, *118* (4), 1742−1769.

(13) Macheroux, P.; Kappes, B.; Ealick, S. E. Flavogenomics−a genomic and structural view of flavin-dependent proteins. *FEBS J.* **2011**, *278* (15), 2625−2634.

(14) Massey, V. The chemical and biological versatility of riboflavin. *Biochem. Soc. Trans.* **2000**, *28* (4), 283−296.

(15) Zhang, M.; Wang, L.; Shu, S.; Sancar, A.; Zhong, D. Bifurcating electron-transfer pathways in DNA photolyases determine the repair quantum yield. *Science* **2016**, *354* (6309), 209−213.

(16) Edwards, A. M., General properties of flavins. In *Flavins: Photochemistry and photobiology*, Silva, E.; Edwards, A. M., Ed.; The Royal Society of Chemistry: Cambridge, UK, 2006; *6*, 1−11.

(17) Sikorski, M.; Khmelinskii, I.; Sikorska, E. Flavin-based fluorescent proteins: emerging paradigms in biological imaging. *Curr. Opin. Biotechnol.* **2021**, 67−96.

(18) Sancar, A. Structure and function of DNA photolyase and cryptochrome blue-light photoreceptors. *Chem. Rev.* **2003**, *103* (6), 2203−2238.

(19) Zhong, D. Electron transfer mechanisms of DNA repair by photolyase. *Annu. Rev. Phys. Chem.* **2015**, *66*, 691−715.

(20) Kao, Y.-T.; Tan, C.; Song, S.-H.; Öztürk, N.; Li, J.; Wang, L.; Sancar, A.; Zhong, D. Ultrafast dynamics and anionic active states of the flavin cofactor in cryptochrome and photolyase. *J. Am. Chem. Soc.* **2008**, *130* (24), 7695−7701.

(21) Mukherjee, A.; Schroeder, C. M. Flavin-based fluorescent proteins: emerging paradigms in biological imaging. *Curr. Opin. Biotechnol.* **2015**, *31*, 16−23.

(22) Seth, D. Photoenzymic repair of UV-damaged DNA: a chemist's perspective. *Chem. Soc. Rev.* **1995**, *24* (4), 289−297.

(23) Emmanuel, M. A.; Bender, S. G.; Bilodeau, C.; Carceller, J. M.; DeHovitz, J. S.; Fu, H.; Liu, Y.; Nicholls, B. T.; Ouyang, Y.; Page, C. G.; Qiao, T.; Raps, F. C.; Sorigué, D. R.; Sun, S.-Z.; Turek-Herman, J.; Ye, Y.; Rivas-Souchet, A.; Cao, J.; Hyster, T. K. Photobiocatalytic Strategies for Organic Synthesis. *Chem. Rev.* **2023**, *123* (9), 5459−5520.

(24) König, B.; Kümmel, S.; Svobodová, E.; Cibulka, R. Flavin photocatalysis. *Phys. Sci. Rev.* **2018**, *3* (8), 20170168.

(25) Srivastava, V.; Singh, P. K.; Srivastava, A.; Singh, P. P. Synthetic applications of flavin photocatalysis: a review. *RSC Adv.* **2021**, *11* (23), 14251−14259.

(26) Martin, C. B.; Shi, X.; Tsao, M.-L.; Karweik, D.; Brooke, J.; Hadad, C. M.; Platz, M. S. The photochemistry of riboflavin tetraacetate and nucleosides. A study using density functional theory, laser flash photolysis, fluorescence, UV−vis, and time resolved infrared spectroscopy. *J. Phys. Chem. B* **2002**, *106* (39), 10263−10271.

(27) Salzmann, S.; Martinez-Junza, V.; Zorn, B. r.; Braslavsky, S. E.; Mansurova, M.; Marian, C. M.; Gärtner, W. Photophysical properties of structurally and electronically modified flavin derivatives determined by spectroscopy and theoretical calculations. *J. Phys. Chem. A* **2009**, *113* (33), 9365−9375.

(28) Heelis, P. The photophysical and photochemical properties of flavins (isoalloxazines). *Chem. Soc. Rev.* **1982**, *11* (1), 15−39.

(29) Sun, M.; Moore, T. Molecular Luminescence Studies of Flavins. I. The Excited States of Flavins. *J. Am. Chem. Soc.* **1972**, *94* (5), 1730−1740.

(30) Rajagopal, S. K.; Mallia, A. R.; Hariharan, M. Enhanced intersystem crossing in carbonylpyrenes. *Phys. Chem. Chem. Phys.* **2017**, *19* (41), 28225−28231.

(31) Schmid, L.; Glaser, F.; Schaer, R.; Wenger, O. S. High triplet energy iridium (III) isocyanoborato complex for photochemical upconversion, photoredox and energy transfer catalysis. *J. Am. Chem. Soc.* **2022**, *144* (2), 963−976.

(32) Cai, X.; Hara, M.; Kawai, K.; Tojo, S.; Majima, T. Sensitized reactions by benzophenones in the higher triplet excited state. *Chem. Phys. Lett.* **2003**, *371* (1−2), 68−73.

(33) Roth, M.; Guyon, L.; Roslund, J.; Boutou, V.; Courvoisier, F.; Wolf, J.-P.; Rabitz, H. Quantum control of tightly competitive product channels. *Phys. Rev. Lett.* **2009**, *102* (25), No. 253001.

(34) Brazard, J.; Usman, A.; Lacombat, F.; Ley, C.; Martin, M. M.; Plaza, P. New insights into the ultrafast photophysics of oxidized and reduced FAD in solution. *J. Phys. Chem. A* **2011**, *115* (15), 3251−3262.

(35) Weigel, A.; Dobryakov, A. L.; Veiga, M.; Pérez Lustres, J. L. Photoinduced processes in riboflavin: Superposition of $\pi\pi^*$−nπ^* states by vibronic coupling, transfer of vibrational coherence, and population dynamics under solvent control. *J. Phys. Chem. A* **2008**, *112* (47), 12054−12065.

(36) Xu, Y.; Mewes, L.; Thyrhaug, E.; Sláma, V.; Šanda, F. e.; Langhals, H.; Hauer, J. Isolating pure donor and acceptor signals by polarization-controlled transient absorption spectroscopy. *J. Phys. Chem. Lett.* **2023**, *14*, 5390−5396.

(37) Weyl, H. *The classical groups: their invariants and representations*; Princeton university press: 1946.

(38) Jeffreys, H. In *On isotropic tensors, Mathematical Proceedings of the Cambridge philosophical society*; Cambridge University Press: 1973; 173−176.

(39) Andrews, D. L.; Thirunamachandran, T. On three-dimensional rotational averages. *J. Chem. Phys.* **1977**, *67* (11), 5026−5033.

(40) Lakowicz, J. R. *Principles of fluorescence spectroscopy*; Springer: New York, 2008.

(41) Riedle, E.; Beutter, M.; Lochbrunner, S.; Piel, J.; Schenkl, S.; Spörlein, S.; Zinth, W. Generation of 10 to 50 fs pulses tunable through all of the visible and the NIR. *Appl. Phys. B: Laser Opt.* **2000**, *71*, 457−465.

(42) Trebino, R. *Frequency-Resolved Optical Gating: The Measurement of Ultrashort Laser Pulses: The Measurement of Ultrashort Laser Pulses*; Springer Science & Business Media, 2000.

(43) Slavov, C.; Hartmann, H.; Wachtveitl, J. Implementation and evaluation of data analysis strategies for time-resolved optical spectroscopy. *Anal. Chem.* **2015**, *87* (4), 2328−2336.

(44) Jonas, D. M.; Lang, M. J.; Nagasawa, Y.; Joo, T.; Fleming, G. R. Pump−probe polarization anisotropy study of femtosecond energy transfer within the photosynthetic reaction center of Rhodobacter sphaeroides R26. *J. Phys. Chem.* **1996**, *100* (30), 12660−12673.

(45) Yeh, A. T.; Shank, C. V.; McCusker, J. K. Ultrafast electron localization dynamics following photo-induced charge transfer. *Science* **2000**, *289* (5481), 935−938.

(46) Mewes, L.; Ingle, R. A.; Megow, S.; Böhnke, H.; Baranoff, E.; Temps, F.; Chergui, M. Ultrafast intersystem crossing and structural dynamics of [Pt (ppy)(μ-t Bu2pz)] 2. *Inorg. Chem.* **2020**, *59* (20), 14643−14653.

(47) Albrecht, A. C. Polarizations and assignments of transitions: the method of photoselection. *J. Mol. Spectrosc.* **1961**, *6*, 84−108.

(48) Thyrhaug, E.; Sorensen, T. J.; Gryczynski, I.; Gryczynski, Z.; Laursen, B. W. Polarization and symmetry of electronic transitions in long fluorescence lifetime triangulenium dyes. *J. Phys. Chem. A* **2013**, *117* (10), 2160−2168.

(49) Thyrhaug, E.; Zidek, K.; Dostal, J.; Bina, D.; Zigmantas, D. Exciton structure and energy transfer in the Fenna-Matthews-Olson complex. *J. Phys. Chem. Lett.* **2016**, *7* (9), 1653−1660.

(50) Casanova-Páez, M.; Goerigk, L. Time-dependent long-range-corrected double-hybrid density functionals with spin-component and spin-opposite scaling: A comprehensive analysis of singlet−singlet and singlet−triplet excitation energies. *J. Chem. Theory Comput.* **2021**, *17* (8), 5165−5186.

(51) Neese, F. Software update: The ORCA program system—Version 5.0. *Wiley Interdiscip. Rev. Comput. Mol. Sci.* **2022**, *12* (5), No. e1606.

(52) Lin, Y.-S.; Li, G.-D.; Mao, S.-P.; Chai, J.-D. Long-range corrected hybrid density functionals with improved dispersion corrections. *J. Chem. Theory Comput.* **2013**, *9* (1), 263−272.

(53) Dahl, J. P.; Springborg, M. The Morse oscillator in position space, momentum space, and phase space. *J. Chem. Phys.* **1988**, *88* (7), 4535−4547.

(54) Mai, S.; Avagliano, D.; Heindl, M.; Marquetand, P.; Menger, M. F. S. J.; Oppel, M.; Plasser, F.; Polonius, S.; Ruckenbauer, M.; Shu, Y.; Truhlar, D. G.; Zhang, L.; Zobel, P.; González, L. *SHARC3.0: Surface Hopping Including Arbitrary Couplings − Program Package for Non-Adiabatic Dynamics*, 2023.

(55) Didraga, C.; Pugžlys, A.; Hania, P. R.; von Berlepsch, H.; Duppen, K.; Knoester, J. Structure, spectroscopy, and microscopic model of tubular carbocyanine dye aggregates. *J. Phys. Chem. B* **2004**, *108* (39), 14976−14985.

(56) Angulo, G.; Grampp, G.; Rosspeintner, A. Recalling the appropriate representation of electronic spectra. *Spectrochim. Acta A Mol. Biomol. Spectrosc.* **2006**, *65* (3−4), 727−731.

(57) Stanley, R. J. MacFarlane, Ultrafast excited state dynamics of oxidized flavins: Direct observations of quenching by purines. *J. Phys. Chem. A* **2000**, *104* (30), 6899−6906.

(58) Kabir, M. P.; Orozco-Gonzalez, Y.; Gozem, S. Electronic spectra of flavin in different redox and protonation states: a computational perspective on the effect of the electrostatic environment. *Phys. Chem. Chem. Phys.* **2019**, *21* (30), 16526−16537.

(59) Jacoby Morris, K.; Barnard, D. T.; Narayanan, M.; Byrne, M. C.; McBride, R. A.; Singh, V. R.; Stanley, R. J. Comparing ultrafast excited state quenching of flavin 1,N^6-ethenoadenine dinucleotide and flavin adenine dinucleotide by optical spectroscopy and DFT calculations. *Photochem. Photobiol. Sci.* **2022**, *21* (6), 959−982.

(60) Megerle, U.; Wenninger, M.; Kutta, R.-J.; Lechner, R.; König, B.; Dick, B.; Riedle, E. Unraveling the flavin-catalyzed photooxidation of benzylic alcohol with transient absorption spectroscopy from sub-pico-to microseconds. *Phys. Chem. Chem. Phys.* **2011**, *13* (19), 8869−8880.

(61) Ghisla, S.; Massey, V.; Lhoste, J.-M.; Mayhew, S. G. Fluorescence and optical characteristics of reduced flavines and flavoproteins. *Biochemistry* **1974**, *13* (3), 589−597.

(62) Klaumünzer, B.; Kröner, D.; Saalfrank, P. (TD-) DFT calculation of vibrational and vibronic spectra of riboflavin in solution. *J. Phys. Chem. B* **2010**, *114* (33), 10826−10834.

(63) Climent, T.; González-Luque, R.; Merchán, M.; Serrano-Andrés, L. Theoretical insight into the spectroscopy and photochemistry of isoalloxazine, the flavin core ring. *J. Phys. Chem. A* **2006**, *110* (50), 13584−13590.

(64) Immeln, D.; Weigel, A.; Kottke, T.; Perez Lustres, J. L. Primary events in the blue light sensor plant cryptochrome: intraprotein electron and proton transfer revealed by femtosecond spectroscopy. *J. Am. Chem. Soc.* **2012**, *134* (30), 12536−12546.

(65) van Stokkum, I. H.; Larsen, D. S.; van Grondelle, R. Global and target analysis of time-resolved spectra. *Biochim. Biophys. Acta, Bioenerg.* **2004**, *1657* (2−3), 82−104.

(66) Weigel, A.; Dobryakov, A.; Klaumunzer, B.; Sajadi, M.; Saalfrank, P.; Ernsting, N. Femtosecond stimulated Raman spectroscopy of flavin after optical excitation. *J. Phys. Chem. B* **2011**, *115* (13), 3656−3680.

(67) Milota, F.; Prokhorenko, V. I.; Mancal, T.; von Berlepsch, H.; Bixner, O.; Kauffmann, H. F.; Hauer, J. Vibronic and vibrational

coherences in two-dimensional electronic spectra of supramolecular J-aggregates. *J. Phys. Chem. A* **2013**, *117* (29), 6007−6014.

(68) Takaya, T.; Hamaguchi, H.-O.; Iwata, K. Femtosecond time-resolved absorption anisotropy spectroscopy on 9, 9′-bianthryl: Detection of partial intramolecular charge transfer in polar and nonpolar solvents. *J. Chem. Phys.* **2009**, *130* (1), No. 014501.

(69) Valle, L.; Morán Vieyra, F. E.; Borsarelli, C. D. Hydrogen-bonding modulation of excited-state properties of flavins in a model of aqueous confined environment. *Photochem. Photobiol. Sci.* **2012**, *11*, 1051−1061.

(70) Zenichowski, K.; Gothe, M.; Saalfrank, P. Exciting flavins: Absorption spectra and spin−orbit coupling in light−oxygen−voltage (LOV) domains. *J. Photochem. Photobiol., A* **2007**, *190* (2−3), 290−300.

(71) McGimpsey, W. C.; Scaiano, J. C. Photoexcitation of benzophenone triplets: a two-photon pathway for ground state repopulation. *Chem. Phys. Lett.* **1987**, *138* (1), 13−17.

Supporting Information for

Determining Excited State Absorption Properties of a Quinoid Flavin by Polarization-Resolved Transient Spectroscopy

*Yi Xu[1], Martin Peschel[2], Miriam Jänchen[1], Richard Foja[1], Golo Storch[1], Erling Thyrhaug[1], Regina de Vivie-Riedle[2] and Jürgen Hauer[1]**

[1]Technical University of Munich, TUM School of Natural Sciences, Department of Chemistry and Catalysis Research Center, Lichtenbergstraße 4, 85748 Garching, Germany;

[2]Ludwig-Maximilians-Universität München, Department of Chemistry, 81377 München, Germany;

Table of Contents

1. Experimental Section

1.1. General Remarks

1.1.1. Synthetic Techniques, Solvents, and Chemicals

Room temperature is defined as 21–23°C. All reactions with air-sensitive reactants were carried out under an argon atmosphere (Ar 4.8) applying standard Schlenk technique. Unless otherwise noted, all chemicals were obtained from Sigma-Aldrich, Acros, TCI, abcr, or Alfa Aesar and used without further purification. Dichloromethane (2×MB-KOL-A type 2, aluminium oxide), diethyl ether (1×MB-KOL-A type 2, aluminium oxide), and tetrahydrofuran (2×MB-KOL-M type 2, 3 Å molecular sieves) were obtained from a MBSPS 800 MBraun solvent purification system. All other solvents were purchased from commercial suppliers and used without further purification unless otherwise noted. *N*,*N*'-dimethyl formamide (DMF) for spectroscopy was purchased from Sigma-Aldrich (HPLC grade ≥ 99 %).

1.1.2. NMR Spectroscopy

NMR spectra were recorded on Bruker AVHD-300, AVHD-400, AVHD-500, or AV-III-500 spectrometers at ambient temperature unless otherwise noted. Deuterated NMR solvents were purchased from Deutero GmbH or Sigma Aldrich and were used without further purification. Spectra were processed with MestReNova 10.0.1 using the manual phasing and polynomial baseline correction capabilities. Splitting was determined using the multiplet analysis function with manual intervention as necessary. Spectral data is reported as follows: chemical shift (multiplicity [singlet (s), doublet (d), triplet (t), quartet (q), pentet (p), multiplet (m)], coupling constant, integration, assignment). Broad signals are labeled as such (br). Chemical shifts are reported in ppm (δ) and coupling constants are reported in Hz. Resonances are referenced to solvent residual signals.[1] Assignment of all signals was performed by two-dimensional experiments (^{1}H-^{1}H-COSY, ^{1}H-^{13}C-HSQC-ME, and ^{1}H-^{13}C-HMBC). In cases where an unambiguous assignment was not possible, this is indicated by "/" between atom positions in question, while "," is used in cases where resonances of two or more atoms overlap. Apparent multiplets which occur as a result of accidental equality of coupling constants to those of magnetically non-equivalent protons are marked as virtual (*virt.*).

1.1.3. Mass spectrometry

High-resolution mass spectrometry (HR-ESI) was performed on a Thermo Scientific LTQ-FT Ultra (ESI) instrument.

1.1.4. Infrared Spectroscopy

Infrared spectra were recorded on a Perkin Elmer Frontier ATR/FT-IR spectrometer, and ν_{max} are partially reported in cm^{-1}.

1.1.5 Liquid Chromatography

Analytical HPLC measurements were performed on Thermo Fisher Ultimate 3000 series instruments equipped with DAD 3000 detectors, LPG 3400SD pumps, TCC 3000SD thermostats, and WPS 3000SL ANALITICAL autosamplers.

Analytical thin layer chromatography was performed using 60 Å Silica Gel F254 (Merck) pre-coated glass plates. TLC plates were visualized by irradiation with a UV lamp or staining. Preparative flash column chromatography was performed on silica 60 (Merck, 230-400 mesh).

1.2. Flavin Synthesis

1.2.1. *N*-Butyl-2-nitroaniline (SI-1)

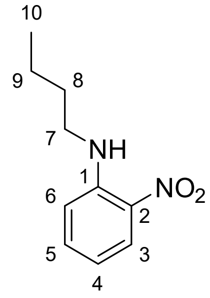

SI-1

Under inert conditions, 2-fluoronitrobenzene (3.73 mL, 5.00 g, 35.4 mmol, 1.00 equiv.) was dissolved in pyridine (35.4 mL, 1.00 M). *n*-Butylamine (3.50 mL, 2.59 g, 35.4 mmol, 1.00 equiv.) and potassium carbonate were added. The suspension was stirred at 80 °C for 16 h. After cooling to room temperature, CH_2Cl_2 (500 mL) was added and the solids were removed to obtain an orange solution. The solvent was removed *in vacuo* and co-evaporated with toluene was performed until the pyridine was fully removed (approx. 4×15 mL toluene) to afford SI-**1** as an orange solid (6.88 g, >99 %). No further purification was performed and the crude product was used for the subsequent step.

1.2.2. *N*^{1}-Butylbenzene-1,2-diamine (SI-2)

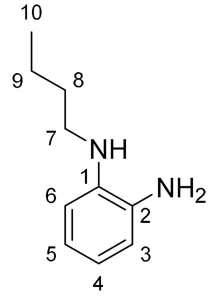

SI-2

Under inert conditions, aniline SI-**1** (6.88 g, 35.4 mmol, 1.00 equiv.) was dissolved in acetic acid (35.4 mL, 1.00 M) before adding palladium on charcoal (10 %, 1.13 g, 1.06 mmol, 0.03 equiv.). The orange solution was degassed by freeze-pump-thaw (3x) before adding a balloon filled with hydrogen. The solution was stirred under an atmosphere of hydrogen for

16 h until full consumption of the starting material. The catalyst was separated by Whatman® filtration into a separate flask under inert conditions affording a faint orange solution of diamine SI-**2** (5.82 g, 35.4 mmol, quantitative conversion was assumed), which was used without further purification for the next step.

1.2.3. 10-Butylbenzo[*g*]pteridine-2,4(3*H*,10*H*)-dione (SI-3)

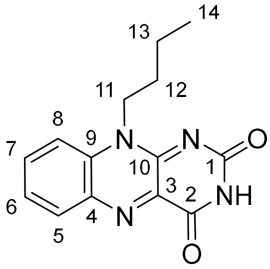

SI-3

Under inert conditions, to the orange solution containing diamine SI-**2** (5.82 g, 35.4 mmol, 1.00 equiv.) in acetic acid (35.4 mL, 1.00 M), boron oxide (9.87 g, 141 mmol, 4.00 equiv.) and alloxane monohydrate (14.2 g, 88.6 mmol, 2.50 equiv.) were added. At room temperature, the solution was stirred for 16 h. After completion of the reaction, the solvent was removed *in vacuo*. Water (100 mL) was added and the reaction flask subjected to sonification. The suspension was filtrated using a vacuum filter. The solid residue was washed with water multiple times to remove excess boron oxide and alloxane. After washing, the residue was dried *in vacuo* affording flavin SI-**3** as orange solid (3.54 g, 13.1 mmol, 37 %). No further purification was performed.

1.2.4. 3,10-Dibutylbenzo[*g*]pteridine-2,4(3*H*,10*H*)-dione (1)

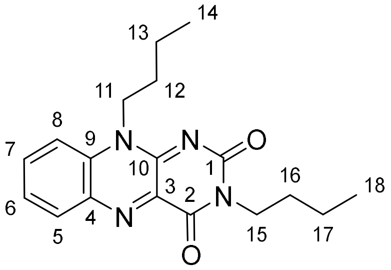

1

Flavin SI-**3** (1.00 g, 3.70 mmol, 1.00 equiv.) was dissolved in *N*,*N*-dimethyl formamide (anhydrous, 37.0 ml, 0.1 M). Potassium carbonate (4.09 g, 29.6 mmol, 8.00 equiv.) was added before dropwise addition of *n*-butyliodide (3.33 ml, 5.39 g, 29.6 mmol, 8.00 equiv.) (**caution:** keep an aqueous ammonia solution nearby to quench the reagent). At room temperature, the yellow solution was stirred for 16 h before adding ammonia (25 % aqueous solution) to quench the excess reagent. The suspension was partitioned between CH_2Cl_2 (200 mL) and brine (200 mL). The aqueous phase was extracted with CH_2Cl_2 (3x 100 mL). All combined organic phases were dried ($MgSO_4$), filtrated, and concentrated *in vacuo*. The crude product was purified *via* column chromatography (silica, CH_2Cl_2/acetone, 100/0 -> 97/3 -> 95/5) to afford alkylated flavin **1**.

Yellow solid (704 mg, 2.15 mmol, 58 %), **TLC:** R_f = 0.41 (CH_2Cl_2/acetone 95/5); **^{1}H NMR** (400 MHz, $CDCl_3$, 298 K): δ (ppm) = 8.32 – 8.25 (m, 1H, H^5), 8.05 – 7.77 (m, 1H, H^8), 7.77 – 7.55 (m, 2H, $H^{6,7}$), 4.81 – 4.64 (m, 2H, H^{11}), 4.17 – 4.01 (m, 2H, H^{15}), 1.88 – 1.77 (m, 2H, H^{12}), 1.75 – 1.64 (m, 2H, H^{16}), 1.61 – 1.50 (m, 2H, H^{13}), 1.47 – 1.35 (m, 2H, H^{17}), 1.01 (t, $^3J_{\text{H-}}$ = 7.3 Hz, 3H, H^{14}), 0.94 (t, $^3J_{\text{H-}}$ = 7.3 Hz, 3H, H^{18}); **^{13}C{^{1}H} NMR** (101 MHz, $CDCl_3$, 298 K): δ (ppm) = 159.6 ($C^{1/2}$), 155.7 ($C^{1/2}$), 148.9 (C^{10}), 137.3 (C^3), 136.0 (C^4), 135.6 (C^7), 133.5 (C^5), 132.7 (C^9), 126.4 (C^6), 115.2 (C^8), 44.8 (C^{11}), 42.0 (C^{15}), 30.0 (C^{16}), 29.2 (C^{12}), 20.3 ($C^{13/17}$), 20.3 ($C^{13/17}$), 13.9 ($C^{14/18}$), 13.9 ($C^{14/18}$); **HR-MS** (ESI$^+$): *m/z* = calc. for M = $[C_{18}H_{23}N_4O_2]^+$: 327.1816 ($[M+H]^+$), found: 327.1809; **IR:** (ATR) $\tilde{\nu}$ [cm^{-1}] = 3046, 2962, 2934, 2872, 1709, 1661, 1644 (C=O), 1611, 1586, 1549, 1524, 1512, 1492, 1463, 1424, 1408, 1371, 1337, 1280, 1246, 1217, 1187, 1147, 1109, 1072, 1028, 986, 963, 948, 923, 891, 880, 847, 821, 808, 782, 768, 759, 736, 715, 700.

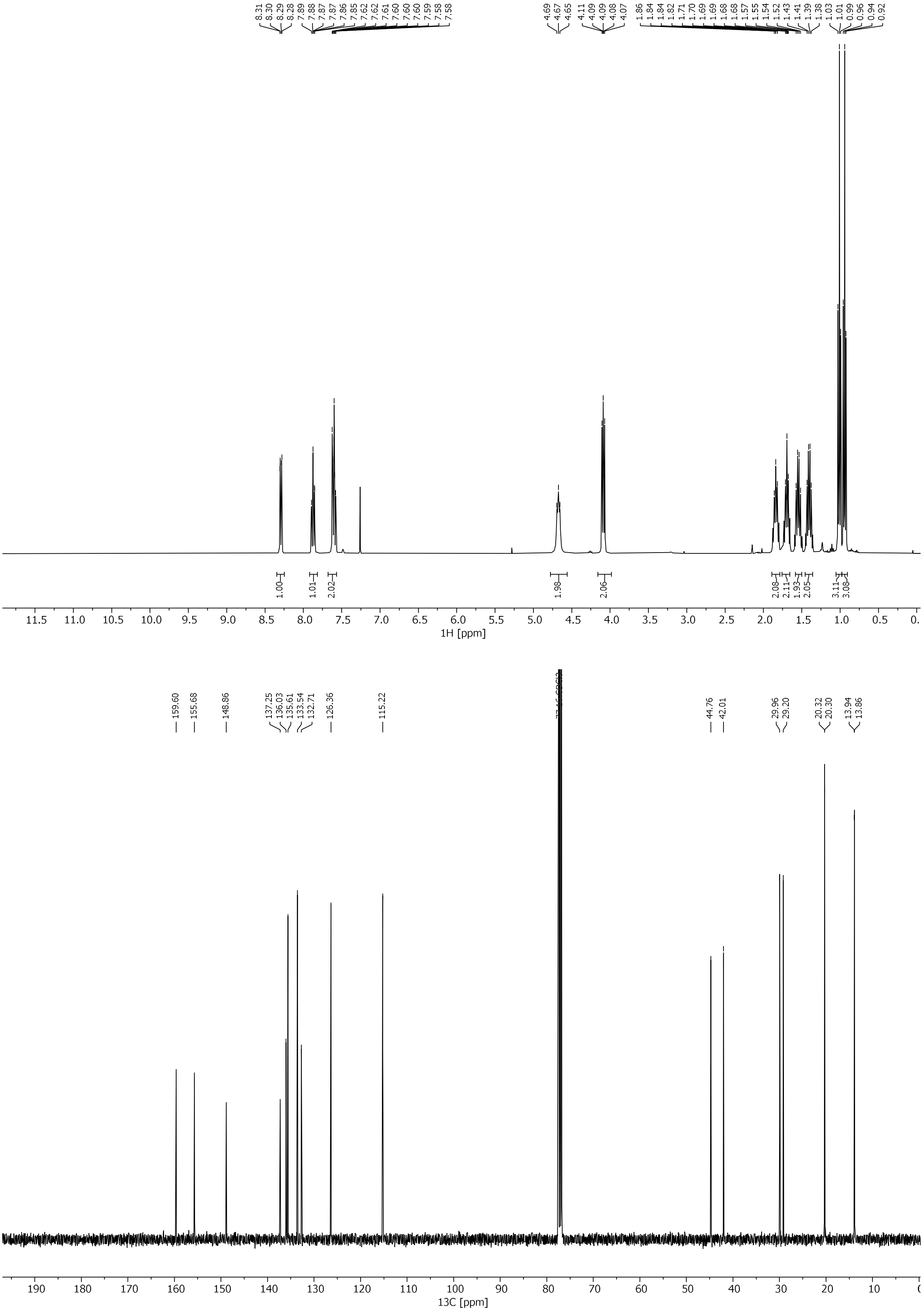

Figure S1 NMR Spectra of flavin **1** ($CDCl_3$, 400 MHz (^1H) and 101 MHz ($^{13}C\{^1H\}$), respectively).

1.3. Transient Absorption Experimental Details

1.3.1. 400 nm pump

The 400 nm excitation pump pulse is obtained via second harmonic generation (SHG) of the 800 nm fundamental pulse inside a 200 μm thin beta-barium borate crystal (BBO, Bluebean Optical Tech Ltd.). Before the BBO, the beam diameter was reduced by a Galilean telescope consisting of a plano-convex lens with 300 mm focal length and a plano-concave lens with 100 mm focal length. The polarization is controlled by a broadband UV (300-470 nm) $\lambda/2$ plate (B.Halle Nachfl. GmbH). The pump pulse with 80 nJ pulse energy is focused using a 250 mm focal length spherical mirror. The pump beam diameter at the sample position is determined to be ~ 150 μm by a beam profiler (CinCam CMOS-1201 CINOGY Tech. GmbH).

1.3.2. NOPA and 325 nm pump

The 325 nm UV-pump is obtained by frequency doubling the output of a tunable non-collinear optical parametric amplifier (NOPA). The NOPA was used to generate 12 nm bandwidth pulses centered at 650 nm, with a resulting pulse duration of 38 fs as determined by Second Harmonic Generation Frequency Resolved Optical Gating (SHG-FROG).

The spectral width is limited by chirping the NOPA pump with a pair of 5 mm fused silica windows post at Brewster angle, and white light with fused silica chirper blocks of 17.88 mm. To increase the SHG efficiency, the 650 nm pulse is focused into the BBO crystal (type I, 40° cut angle, 200 μm) by using a 100 mm focusing spherical mirror and recollimated by a 70 mm spherical focusing mirror. The residual 650 nm fundamental light is filtered out by using a 1 mm thick UG5 filter. The 325 nm UV pump beam is focused with an Al-coated 150 mm focal length spherical focusing mirror to the sample position with a spot size of ~ 150 μm. A ND filter was used to control the 650 nm NOPA output intensity before the prism compressor in an effort to keep UV pulse energies below 60 nJ at the sample position. A broadband (460–680 nm) $\lambda/2$ plate (B.Halle Nachfl. GmbH) is placed before the SHG-BBO to set the polarization. The polarization of the pump pulse is controlled by simultaneously change the orientations of BBO and $\lambda/2$ plate.

1.3.1. CaF_2 white light

White light for detection is generated by focusing 4 µJ of 800 nm light into a 5 mm thick CaF_2 crystal. To avoid damage, the crystal is continuously translated in a plane orthogonal to the beam direction. The focal length is 100 mm and the numerical aperture of the focused beam is chosen to yield a white light spectrum extending down to 370 nm. The white light pulse is collimated using a 100 mm focal length spherical mirror and the intensity of the 800 nm driving pulse is decreased using a heat absorbing filter.

The white light is split into a probe part and a reference part. The probe pulse is focused into the sample by using a 150 mm focal length spherical mirror and the spot size is ~ 30 µm. The probe spatially overlaps with the center of pump and is recollimated after the sample by using an achromatic lens with 75 mm focal length. The probe and reference laser pulses are detected using a home-built prism spectrometer in combination with a pair of high-speed CMOS linear array cameras (Glaz LineScan-I-Gen2, Synertronic Designs).

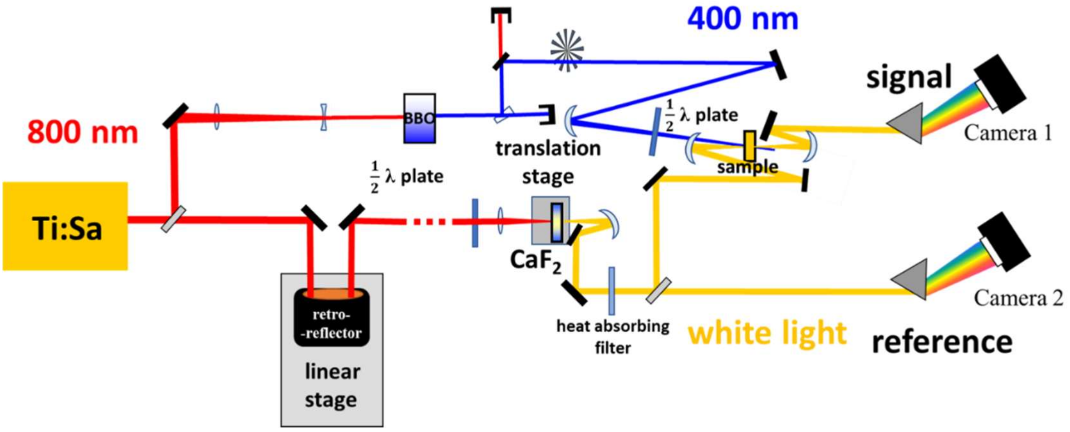

Figure S2 400 nm pumped transient spectroscopy set-up.

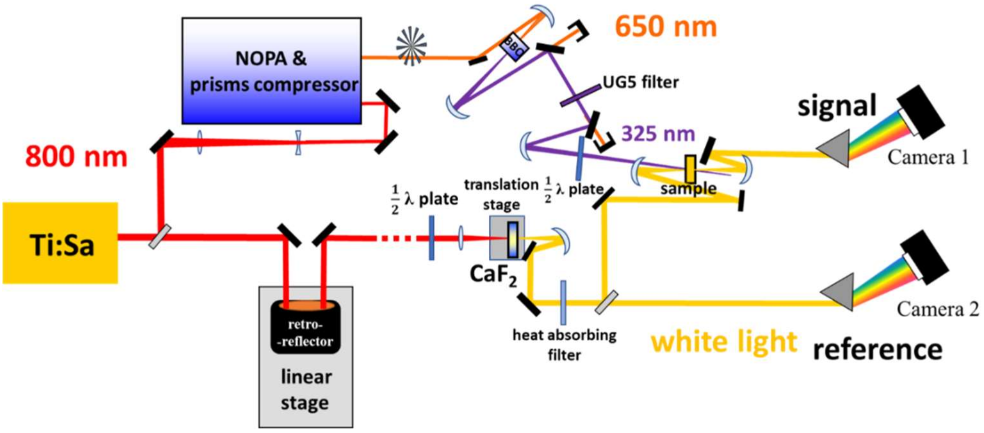

Figure S3 325 nm pumped transient spectroscopy set-up.

2. Transient Anisotropy Spectra Time Traces

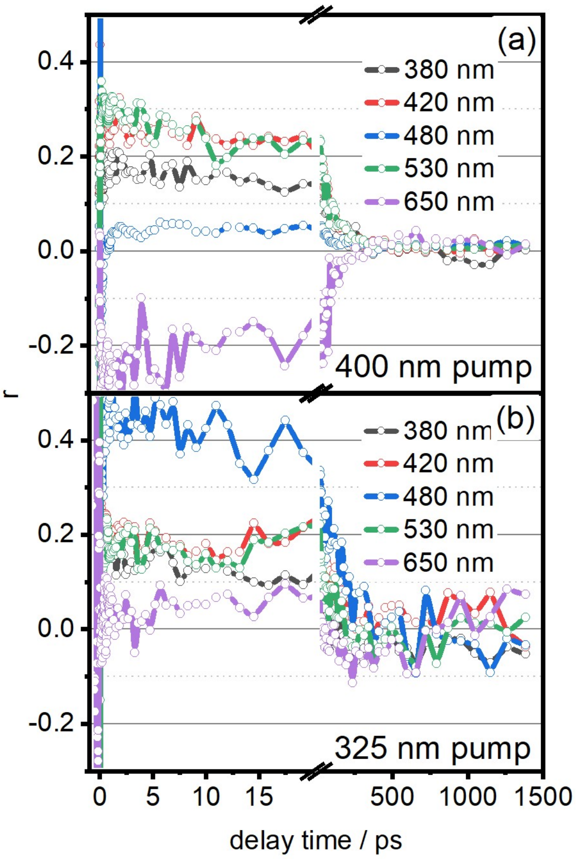

Figure S4 Time traces of transient absorption anisotropies at 380, 420, 480, 530 and 650 nm for (a) 400 nm and (b) 325 nm pumped measurements, the TAA traces indicate no significant rotational diffusion of the sample in 20 ps.

4. Evolution Associated Spectra

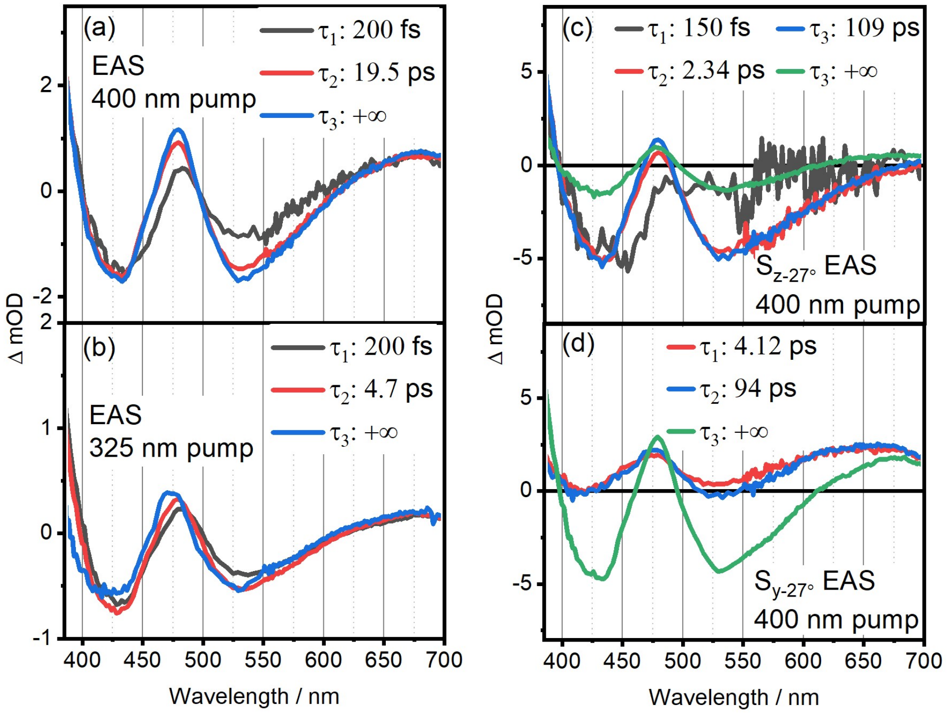

Figure S5 Evolution associated spectra (EAS) from GLA of MA-TA data for **1** with pump wavelength (a) 400 nm and (b) 325 nm, and EAS that for $S_{z-27^{\circ}}^{400\ nm}$ and $S_{y-27^{\circ}}^{400\ nm}$ are showing in (c) and (d).

We apply GTA to $S_{z-2\ ^{\circ}}^{400\ nm}$ and $S_{y-27^{\circ}}^{400\ nm}$, depicted in Figure S5 (c) and (d), respectively. Similar to TA-MA data, the $S_{z-27^{\circ}}^{400\ nm}$ dataset displays a <200 fs species dominated by GSB and SE components but this component is not observable in the $S_{y-27^{\circ}}^{400\ nm}$. However, both datasets contain the few ps species, the ~100 ps species, and long decay time species. The ~100 ps components are related to rotational diffusion and are exclusively found in the datasets based on PAS.

5. Red-ESA disentanglement

Details of Takaya et al.'s method to resolved the spectral components for two overlapping species.[2] By applying eq. S1 and eq. S2 two components with different initial anisotropy values can be isolated:

$$S_{MA}^{(1)}(\lambda,t)=\frac{r^{obs}(\lambda,t)\exp\left(\frac{t}{T_{rot}}\right)-r^{(2)}(\lambda,0)}{r^{(1)}(\lambda,0)-r^{(2)}(\lambda,0)}S_{MA}^{obs}(\lambda,t), \qquad \text{eq. S1}$$

$$S_{MA}^{(2)}(\lambda,t)=\frac{r^{(1)}(\lambda,0)-r^{obs}(\lambda,t)\exp\left(\frac{t}{T_{rot}}\right)}{r^{(1)}(\lambda,0)-r^{(2)}(\lambda,0)}S_{MA}^{obs}(\lambda,t), \qquad \text{eq. S2}$$

where $r^{obs}(\lambda,t)$ is the observed TAA and $S_{MA}^{obs}(\lambda,t)$ is the observed MA spectrum. $r^{(1)}(\lambda,0)$ and $r^{(2)}(\lambda,0)$ are the TAA value of the single transitions and $S_{MA}^{(1)}(\lambda,t)$ and $S_{MA}^{(2)}(\lambda,t)$ are their corresponding isolated MA spectra. T_{rot} is the lifetime of rotational diffusion, which is long compared to our time-window here, meaning that the term $exp\left(\frac{t}{T_{rot}}\right)$ approaches 1. We take TAA values at 550 nm and 700 nm as the TAA for single transitions, and by applying eq. S1 and eq. S2 we obtain the pure SE and pure red-ESA spectra between 550 and 700 nm, see Figure S6 **Fehler! Verweisquelle konnte nicht gefunden werden.** (b). By adding the pure spectra together, we retrieve the MA spectrum (green vs. blue line).

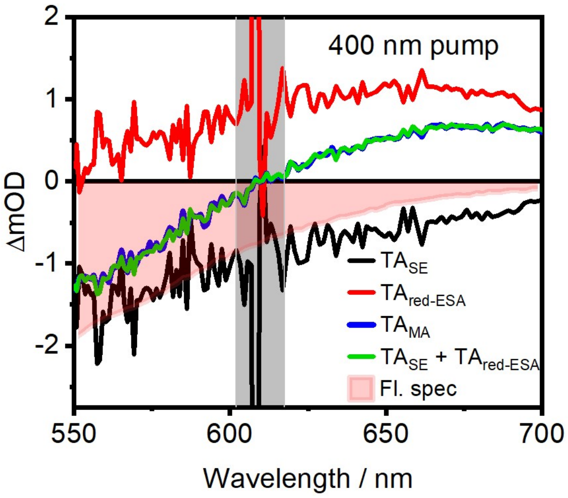

Figure S6 ESA spectra (red solid line) and pure SE signal (black) extracted from the total TA signal (blue) according to eq. S1 and eq. S2. The wavelength where the MA spectra cross zero are indicated by grey areas

6. PAS for $\beta = 0^{\circ}$ and $\beta = 40^{\circ}$

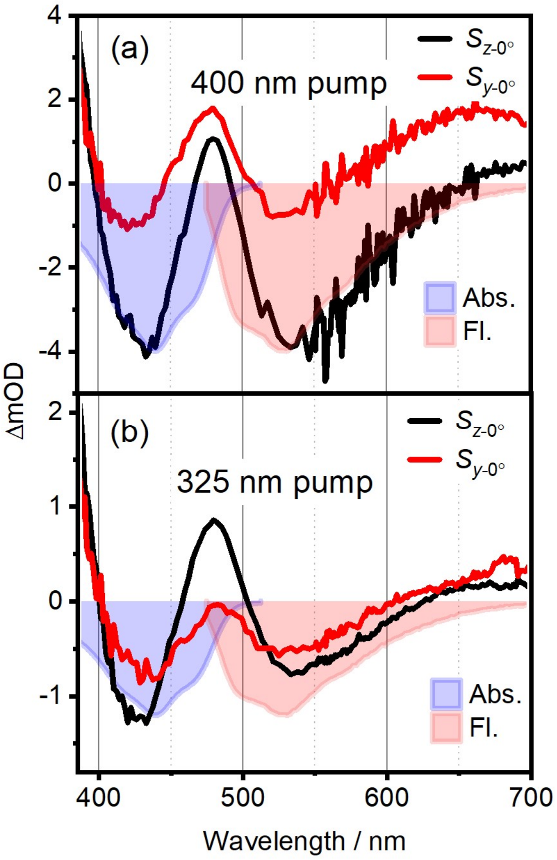

Figure S7 Polarization associated spectra calculation of (a) 400 nm and (b) 325 nm pumped measurements. S_z (black solid) and S_y (red solid) components of with 0° coordinate system rotation, compare with negatively plotted absorption and fluorescence spectra (blue filled and red filled)

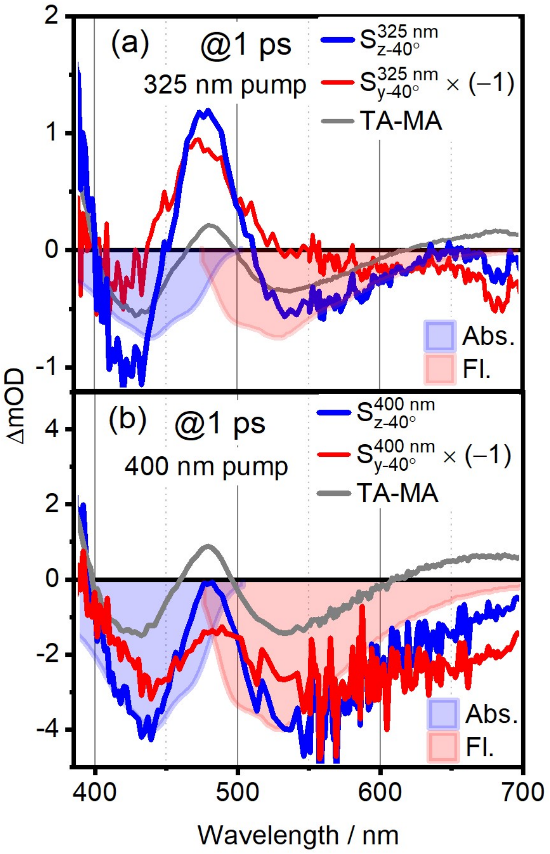

Figure S8 (a) Polarization associated spectra (PAS) for 325 nm excitation. The $S_{z-40°}^{325nm}$ component (blue) optimizes the stimulated emission component with respect to the magic angle TA-spectrum (dark gray). The corresponding $S_{y-40°}^{325\,nm}$ component (red) shows good overlap with the pure ESA spectrum (dotted) and over-emphasizes the red ESA transition peaking at 650. b) shows the PAS for 400 nm excitation and $\beta = 40°$.

7. Minimizing Red-ESA

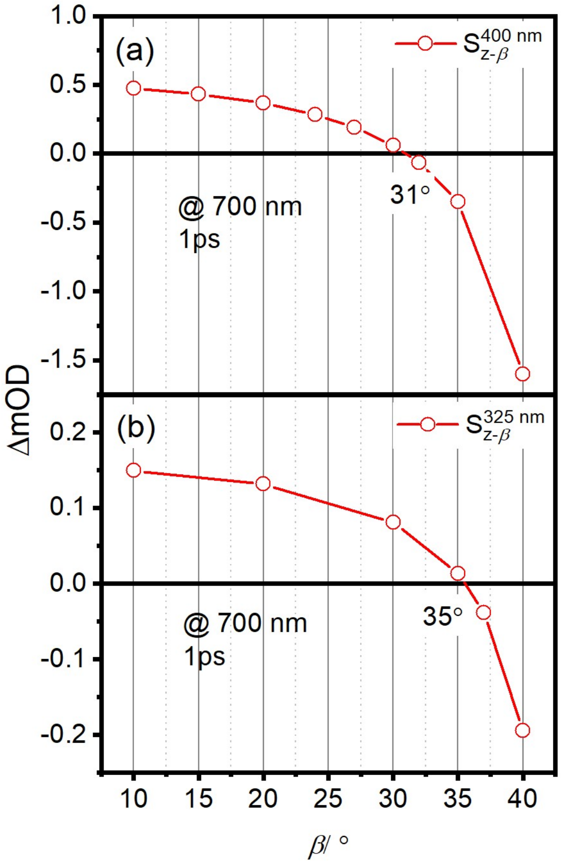

Figure S9 (a) 400 nm and (b) 325 nm pumped S_z signals at 700 nm with the changing of β.

8. Calculation of Palarized Spectra and Anisotropies

Hamm and Zanni[3] give an expression according to *Hochstrasser*[4] for the orientational prefactor of the pump-probe signal depending on the angle between the pumped and probed transition dipole moments and the pump and probe fields. Assuming the molecule has approached a thermal distribution in the S_1 at the time of the probe pulse, this prefactor can be evaluated for each combination of pumped transitions and probed transitions within the molecular ensemble. Here, a single pumped transition corresponds to a transition of one sample of the Wigner distribution in the S_0 minimum to a higher state. A single probed transition corresponds to either A) a transition of one sample of the Wigner distribution in the S_1 minimum to a higher state (excited state absorption) or B) a transition of one sample of the Wigner distribution in the S_1 minimum to a lower state (stimulated emission) or C) a transition of one sample of the Wigner distribution in the S_0 minimum to a higher state (ground state bleach). Rotations and translations of the molecules due to the relaxation in S_1 need to be (approximately) removed prior to the calculation of the spectra (for example by fulfilling the Eckart conditions using a quaternion algorithm).[5-7] Then, the polarized pump probe spectra can be calculated according to:

$$S_{\parallel}(\omega_{pump}, \omega_{probe}) \propto \sum_{i}^{\substack{pumped\\transitions}} \sum_{j}^{\substack{probed\\transitions}} (-1)^n g_i(\omega_{pump}) g_j(\omega_{probe}) |\mu_i|^2 |\mu_j|^2 (1 + \frac{2(\mu_i \cdot \mu_j)^2}{|\mu_i|^2 |\mu_j|^2}) \qquad \textit{eq. S3}$$

$$S_{\perp}(\omega_{pump}, \omega_{probe}) \propto \sum_{i}^{\substack{pumped\\transitions}} \sum_{j}^{\substack{probed\\transitions}} (-1)^n g_i(\omega_{pump}) g_j(\omega_{probe}) |\mu_i|^2 |\mu_j|^2 (2 - \frac{(\mu_i \cdot \mu_j)^2}{|\mu_i|^2 |\mu_j|^2}) \qquad \textit{eq. S4}$$

Here, μ_i is the transition dipole moment vector of the transition i and g_i is a lineshape function (in our case, a fixed-width Gaussian centered at the transition frequency for transition i). n is odd for ground state bleach or stimulated emission and even for excited state absorption if the typical sign convention for TA spectroscopy is used. From these spectra, anisotropies can be calculated according to eq. 2 in the main manuscript.

9. ORCA[8] Inputs

S_0 geometry optimization and frequency analysis:

```
! wb97x-d3 ma-def2-TZVP CPCM(DMF) AutoAux RIJCOSX OPT FREQ verytightscf
verytightopt

*xyzfile 0 1 geo.xyz
```

S_1 geometry optimization and frequency analysis:

```
! wb97x-d3 ma-def2-TZVP CPCM(dmf) AutoAux RIJCOSX OPT NUMFREQ verytightscf
verytightopt

%tddft
  nroots 10
  iroot 1
  tda true
  maxdim 5
end

*xyzfile 0 1 geo.xyz
```

Excitation Energies at S_0 Minimum:

```
! RI-SCS-wPBEPP86 CPCM(dmf) RIJCOSX verytightscf defgrid3
%MaxCore 90000

%basis
   basis "aug-cc-pVTZ"
   auxJ "aug-cc-pVTZ/JK"
   auxC "aug-cc-pVTZ/C"
end

%tddft
    lrcpcm true
    cpcmeq false
    iroot 1
    tda true
    triplets false
    nroots 20
    dotrans true
end

*xyzfile 0 1 optfreq0.xyz
```

Excitation Energies at S_1 Minimum:

```
! RI-SCS-wPBEPP86 CPCM(dmf) RIJCOSX verytightscf defgrid3
%MaxCore 90000

%basis
   basis "aug-cc-pVTZ"
   auxJ "aug-cc-pVTZ/JK"
```

```
   auxC "aug-cc-pVTZ/C"
end

%tddft
    lrcpcm true
    cpcmeq true
    iroot 1
    tda true
    triplets false
    nroots 20
    dotrans true
end

*xyzfile 0 1 optfreq1.xyz
```

Conical intersection S_3/S_2

```
! wb97x-d3 ma-def2-TZVP CPCM(dmf) AutoAux RIJCOSX CI-OPT NUMFREQ verytightscf

%tddft
  nroots 10
  iroot 2
  jroot 3
  tda true
  maxdim 5
end

*xyzfile 0 1 start2.xyz
```

Conical Intersection S_2/S_1

```
! wb97x-d3 ma-def2-TZVP CPCM(dmf) AutoAux RIJCOSX CI-OPT NUMFREQ verytightscf

%tddft
  nroots 10
  iroot 1
  jroot 2
  tda true
  maxdim 5
end

*xyzfile 0 1 start2.xyz
```

10. Coordinates of Optimized Structures of 3,10-Dimethylbenzo[*g*]pteridine-2,4(3*H*,10*H*)-dione

S_0 Minimum:

```
28
Coordinates from ORCA-job optfreq0
  C   4.23851478459039     -1.08381262468763      0.00058157339000
  C   4.36445075403855      0.31218200016134      0.00102551683880
  C   3.26157445558767      1.13400590829665      0.00077750923815
  C   1.98003541896443      0.56798952727958      0.00005888924302
  C   1.84664512363408     -0.83187151982743     -0.00020375181732
  C   2.99017436249219     -1.64763518901150     -0.00000001401433
  N   0.83671012831972      1.34424457242778     -0.00033940718913
  N   0.61751628670228     -1.42532553567634     -0.00051922468987
  C   -0.42577102918346     -0.67633268988263     -0.00056827477482
  C   -0.39090265675847      0.77109229635780     -0.00058709314992
  C   -1.76605914574389     -1.33412739895975     -0.00041178178854
  N   -1.46346867573980      1.51428624642725     -0.00093794425536
  C   -2.69670012188802      0.93443540481365     -0.00084449480897
  N   -2.82732810960915     -0.46919621573888      0.00037368307788
  O   -3.71570898948508      1.60315809369119     -0.00160052169061
  C   -4.18332985717295     -1.00691432271613      0.00187800142579
  H   5.12367863797869     -1.70672171245055      0.00074725362108
  H   5.35052446989323      0.76062181174973      0.00161089344574
  H   3.39434867531856      2.20582679156154      0.00120184154458
  H   2.84675969041802     -2.72106098318571     -0.00028348917836
  H   -4.71500788078144     -0.67226729076667     -0.88696034406074
  H   -4.71599100579992     -0.66299766071344      0.88649111048473
  H   -4.11722875563099     -2.08944157197428      0.00749234159472
  C   0.96212143793764      2.80096500127656     -0.00041654816073
  H   -0.03180526346773      3.22955881826940     -0.00195471828553
  H   1.50274570832851      3.11831312689894     -0.89098063771696
  H   1.50015199598675      3.11872921528045      0.89158898087409
  O   -1.88836784002982     -2.54157216590090     -0.00074863729737
```

S_1 Minimum:

```
28
Coordinates from ORCA-job optfreq1
  C   4.23851478459039     -1.08381262468763      0.00058157339000
  C   4.36445075403855      0.31218200016134      0.00102551683880
  C   3.26157445558767      1.13400590829665      0.00077750923815
  C   1.98003541896443      0.56798952727958      0.00005888924302
  C   1.84664512363408     -0.83187151982743     -0.00020375181732
  C   2.99017436249219     -1.64763518901150     -0.00000001401433
  N   0.83671012831972      1.34424457242778     -0.00033940718913
  N   0.61751628670228     -1.42532553567634     -0.00051922468987
  C   -0.42577102918346     -0.67633268988263     -0.00056827477482
  C   -0.39090265675847      0.77109229635780     -0.00058709314992
  C   -1.76605914574389     -1.33412739895975     -0.00041178178854
  N   -1.46346867573980      1.51428624642725     -0.00093794425536
  C   -2.69670012188802      0.93443540481365     -0.00084449480897
  N   -2.82732810960915     -0.46919621573888      0.00037368307788
  O   -3.71570898948508      1.60315809369119     -0.00160052169061
  C   -4.18332985717295     -1.00691432271613      0.00187800142579
  H   5.12367863797869     -1.70672171245055      0.00074725362108
  H   5.35052446989323      0.76062181174973      0.00161089344574
  H   3.39434867531856      2.20582679156154      0.00120184154458
  H   2.84675969041802     -2.72106098318571     -0.00028348917836
  H   -4.71500788078144     -0.67226729076667     -0.88696034406074
  H   -4.71599100579992     -0.66299766071344      0.88649111048473
  H   -4.11722875563099     -2.08944157197428      0.00749234159472
  C   0.96212143793764      2.80096500127656     -0.00041654816073
  H   -0.03180526346773      3.22955881826940     -0.00195471828553
  H   1.50274570832851      3.11831312689894     -0.89098063771696
  H   1.50015199598675      3.11872921528045      0.89158898087409
  O   -1.88836784002982     -2.54157216590090     -0.00074863729737
```

S_3/S_2 Conical Intersection

```
28
Coordinates from ORCA-job optfreq_coin32
  C   4.29425661956934     -1.07245811045370      0.01736912472934
  C   4.40913310564715      0.29230111706939      0.07377031700493
  C   3.24114678197731      1.10859761219701      0.05900173763550
  C   1.96465690932745      0.55638637392704     -0.01284559455018
  C   1.82577633538214     -0.84751042214504     -0.05662889960939
  C   3.02125456976781     -1.64316385220482     -0.04373478987359
  N   0.82868532844543      1.34146710810086     -0.03639228518863
  N   0.64906481276311     -1.46028499117089     -0.09036270306285
  C   -0.45433319398412     -0.66952517242481     -0.05228515215354
  C   -0.41474507300613      0.73858513741422     -0.01526732307550
  C   -1.75742402777369     -1.31067061087338     -0.03886704162943
  N   -1.47970648925671      1.51141992558395      0.03089634515704
  C   -2.71218792450388      0.95269386782956      0.04899343702584
  N   -2.83502221562247     -0.44285297902088      0.02024459647610
  O   -3.73698959365906      1.63031851253402      0.09177848897389
  C   -4.18223947543245     -0.99217638268569      0.04633469056959
  H   5.16838197037306     -1.70931752150208      0.02565441582693
  H   5.37700005857043      0.77247908069339      0.12902932496291
  H   3.37086247288016      2.18062326474964      0.11099026824767
  H   2.89595011803139     -2.71914114519348     -0.08296069962496
  H   -4.72796710861203     -0.69701423929859     -0.84971950992877
  H   -4.71644922970621     -0.62151578820991      0.91948454181732
  H   -4.10544075311393     -2.07321187827696      0.08899975928866
```

```
  C   0.94767520081201      2.79090067593374     -0.06774880238264
  H   -0.04467565027463      3.20842455790686     -0.18652237775283
  H   1.57372169780928      3.09081692799728     -0.90865707879818
  H   1.38467406823780      3.15806543733269      0.86301260892652
  O   -1.90677431464855     -2.52810550580942     -0.07709739901175
```

S_2/S_1 Conical Intersection

```
28
Coordinates from ORCA-job optfreq_coin21
  C   4.27991074680356     -1.06375940370183      0.01718803402552
  C   4.39755746703502      0.32554292123023      0.03401887368755
  C   3.27111806979848      1.12878451368743      0.02191415806176
  C   1.99933441922267      0.55961295817400     -0.00518597758850
  C   1.88348046505211     -0.86586681861157     -0.01329701324052
  C   3.03488155507028     -1.65777942031281     -0.00536131788043
  N   0.84017050194790      1.31950213453870     -0.02289480895502
  N   0.64545553114378     -1.37726724051773     -0.02543657716318
  C   -0.47808186662645     -0.69188473018736     -0.01204878774532
  C   -0.39914526271302      0.73676097639180     -0.00552484416589
  C   -1.78396904161621     -1.32407995177701     -0.00607630913656
  N   -1.47124443458215      1.47515212213440      0.01604639732554
  C   -2.72838663518017      0.93663120999243      0.03508708630297
  N   -2.85708983222803     -0.44688260995319      0.00657527679322
  O   -3.72257010659799      1.64565703999968      0.07408251763989
  C   -4.21102432191322     -0.98713325060308      0.00889227758895
  H   5.16798443410037     -1.68309681282262      0.02391974434338
  H   5.37628145912209      0.78718047359585      0.05724436131545
  H   3.38298137493886      2.20366008310632      0.03545604523739
  H   2.91825204194953     -2.73338766829034     -0.01526476173739
  H   -4.78050005530258     -0.54786863517970     -0.80761123108276
  H   -4.70580323640045     -0.75730537744331      0.95208399225045
  H   -4.14458478298816     -2.06227330579782     -0.11889014804996
  C   0.95378424004256      2.77290842982025     -0.05019326607771
  H   -0.04345533743455      3.19215965081560     -0.11368842033801
  H   1.53613399453171      3.07617162291252     -0.92010071453278
  H   1.44313966504219      3.12404588160678      0.85898426625489
  O   -1.92632605221816     -2.53905379280765     -0.01344885313294
```

11. Calculated (Transient-) Absorption Energies and Transition Dipoles at the Minima

S_0 Minimum:

```
-----------------------------------------------------------------------------
         ABSORPTION SPECTRUM VIA TRANSITION ELECTRIC DIPOLE MOMENTS
-----------------------------------------------------------------------------
State   Energy    Wavelength  fosc         T2        TX        TY        TZ
        (cm-1)      (nm)                 (au**2)    (au)      (au)      (au)
-----------------------------------------------------------------------------
   1   24949.6    400.8   0.500180264   6.59993  -2.52963  -0.44824  -0.00071
   2   30453.6    328.4   0.002719401   0.02940   0.00032   0.00021  -0.17146
   3   32603.4    306.7   0.172287153   1.73967   1.21262  -0.51887   0.00009
   4   33991.8    294.2   0.000054868   0.00053  -0.00057  -0.00007   0.02304
   5   37531.7    266.4   0.388345466   3.40640  -1.75621   0.56755  -0.00048
   6   39009.2    256.3   0.729034409   6.15257   2.09466  -1.32852   0.00046
   7   40311.7    248.1   0.000055871   0.00046  -0.00161  -0.00218   0.02119
   8   40975.5    244.0   0.042931185   0.34492   0.58688   0.02221   0.00029
   9   41007.5    243.9   0.000020130   0.00016  -0.00587   0.00196  -0.01111
  10   50018.2    199.9   0.001091577   0.00718   0.00064  -0.00028  -0.08476
  11   44022.6    227.2   0.106277500   0.79477  -0.63449  -0.62626  -0.00026
  12   50689.4    197.3   0.232255834   1.50843  -0.79607  -0.93525  -0.00033
  13   55090.0    181.5   0.005040349   0.03012  -0.00016  -0.00090  -0.17355
  14   51375.8    194.6   0.692333635   4.43642   2.10117  -0.14666   0.00104
  15   56176.9    178.0   0.025476159   0.14930  -0.00213   0.00053   0.38638
  16   56782.5    176.1   0.006874126   0.03985  -0.09408  -0.17608   0.00003
  17   56701.8    176.4   0.000013758   0.00008   0.00020  -0.00015   0.00893
  18   45893.8    217.9   0.000079936   0.00057  -0.00005   0.00027   0.02394
  19   57826.0    172.9   0.009123355   0.05194   0.00005   0.00047  -0.22790
  20   55209.2    181.1   0.108833044   0.64897  -0.17870   0.78552   0.00044


-----------------------------------------------------------------------------
    TRANSIENT ABSORPTION SPECTRUM VIA TRANSITION ELECTRIC DIPOLE MOMENTS
-----------------------------------------------------------------------------
State   Energy  Wavelength   fosc         T2        TX        TY        TZ
        (cm-1)    (nm)                  (au**2)    (au)      (au)      (au)
-----------------------------------------------------------------------------
   2    5504.0   1816.9   0.000020475   0.00122   0.00034   0.00061   0.03499
   3    7653.8   1306.5   0.006340807   0.27274  -0.40515  -0.32953  -0.00014
   4    9042.3   1105.9   0.000000822   0.00003   0.00090   0.00044  -0.00538
   5   12582.2    794.8   0.009010832   0.23577   0.47662   0.09276   0.00011
   6   14059.6    711.3   0.038770372   0.90782   0.85674  -0.41693   0.00008
   7   15362.1    651.0   0.000115292   0.00247  -0.00349  -0.00691   0.04910
   8   16025.9    624.0   0.048446519   0.99521   0.59171   0.80318   0.00058
   9   16057.9    622.7   0.000045046   0.00092  -0.00582  -0.00132   0.02980
  10   25068.7    398.9   0.005685801   0.07467  -0.00026   0.00039   0.27325
  11   19073.0    524.3   0.504370785   8.70575  -2.69995   1.18997  -0.00082
  12   25739.8    388.5   0.145905122   1.86612   1.17909  -0.68983   0.00036
  13   30140.5    331.8   0.001615335   0.01764   0.00087  -0.00011   0.13283
  14   26426.2    378.4   0.066953669   0.83409  -0.90777  -0.10024  -0.00034
  15   31227.4    320.2   0.000513310   0.00541   0.00042  -0.00012  -0.07356
  16   31833.0    314.1   0.010109780   0.10455  -0.00308   0.32333   0.00010
  17   31752.3    314.9   0.000458026   0.00475   0.00006   0.00004   0.06891
  18   20944.2    477.5   0.000305899   0.00481  -0.00007  -0.00055   0.06934
  19   32876.5    304.2   0.001887150   0.01890  -0.00082  -0.00037   0.13746
  20   30259.6    330.5   0.166807338   1.81479  -0.97542  -0.92916  -0.00021
```

S_1 Minimum:

```
-----------------------------------------------------------------------------
         ABSORPTION SPECTRUM VIA TRANSITION ELECTRIC DIPOLE MOMENTS
-----------------------------------------------------------------------------
State   Energy    Wavelength  fosc         T2        TX        TY        TZ
        (cm-1)      (nm)                 (au**2)    (au)      (au)      (au)
-----------------------------------------------------------------------------
   1   20000.4    500.0   0.540587228   8.89822  -2.92201  -0.60005  -0.00102
   2   28946.3    345.5   0.307790762   3.50056   1.66954  -0.84452   0.00183
   3   29769.4    335.9   0.003812264   0.04216   0.01752  -0.00755  -0.20444
   4   32033.9    312.2   0.000153990   0.00158  -0.00128   0.00047   0.03976
   5   35995.0    277.8   0.564187350   5.16009  -1.99789   1.08098  -0.00028
   6   35188.9    284.2   0.597887057   5.59356   1.97683  -1.29835   0.00091
   7   37889.0    263.9   0.000035199   0.00031  -0.00088   0.00045  -0.01746
   8   39425.8    253.6   0.006761414   0.05646   0.20652  -0.11751   0.00000
   9   48503.9    206.2   0.001846388   0.01253  -0.00043   0.00003   0.11195
  10   39932.7    250.4   0.000080162   0.00066   0.00328  -0.00061   0.02549
  11   42330.9    236.2   0.295297743   2.29656  -1.21365  -0.90753  -0.00056
  12   47376.4    211.1   0.348686341   2.42297   1.25748   0.91746   0.00092
  13   53540.4    186.8   0.009607262   0.05907  -0.00050  -0.00079  -0.24305
  14   51937.3    192.5   0.335139256   2.12433   1.41662  -0.34279   0.00129
  15   54776.8    182.6   0.022783270   0.13693  -0.00305   0.00047   0.37003
  16   54073.4    184.9   0.048954934   0.29805  -0.51386  -0.18437  -0.00044
  17   51749.3    193.2   0.170308478   1.08345  -0.39650   0.96241   0.00121
  18   52193.7    191.6   0.243810153   1.53783  -0.00847   1.24007   0.00064
  19   44859.8    222.9   0.000129268   0.00095  -0.00051   0.00225  -0.03071
  20   56620.6    176.6   0.007010349   0.04076  -0.00003  -0.00064  -0.20189
```

```
-----------------------------------------------------------------------------
    TRANSIENT ABSORPTION SPECTRUM VIA TRANSITION ELECTRIC DIPOLE MOMENTS
-----------------------------------------------------------------------------
State   Energy  Wavelength   fosc         T2         TX        TY        TZ
        (cm-1)    (nm)                  (au**2)     (au)      (au)      (au)
-----------------------------------------------------------------------------
   2    8945.9   1117.8   0.017932463   0.65992  -0.72188  -0.37256  -0.00072
   3    9769.0   1023.6   0.000068735   0.00232  -0.00636  -0.00258   0.04764
   4   12033.5    831.0   0.000006197   0.00017   0.00161   0.00046  -0.01291
   5   15994.6    625.2   0.008234638   0.16949   0.41076   0.02774  -0.00019
   6   15188.6    658.4   0.058215964   1.26183   1.07380  -0.32984   0.00026
   7   17888.6    559.0   0.000168988   0.00311   0.00061  -0.00313  -0.05568
   8   19425.4    514.8   0.062071193   1.05195  -0.09012   1.02168  -0.00044
   9   28503.5    350.8   0.005571161   0.06435   0.00088  -0.00091  -0.25366
  10   19932.3    501.7   0.000058597   0.00097   0.00557  -0.00001  -0.03061
  11   22330.5    447.8   0.444871535   6.55860  -2.43277   0.80015  -0.00089
  12   27376.0    365.3   0.213828544   2.57141  -1.38339   0.81095  -0.00056
  13   33540.0    298.2   0.001328237   0.01304   0.00063   0.00048   0.11418
  14   31936.9    313.1   0.085369054   0.88000  -0.93737   0.03669  -0.00039
  15   34776.5    287.6   0.000047347   0.00045   0.00221  -0.00029  -0.02105
  16   34073.0    293.5   0.092250758   0.89132   0.70654   0.62620   0.00027
  17   31748.9    315.0   0.143654101   1.48958  -0.89338  -0.83154  -0.00021
  18   32193.3    310.6   0.066280277   0.67779   0.76863   0.29496   0.00014
  19   24859.4    402.3   0.000373425   0.00495   0.00206   0.00099  -0.07029
  20   36620.2    273.1   0.000782748   0.00704  -0.00157  -0.00079   0.08387
```

References

(1) Fulmer, G. R.; Miller, A. J.; Sherden, N. H.; Gottlieb, H. E.; Nudelman, A.; Stoltz, B. M.; Bercaw, J. E.; Goldberg, K. I., NMR chemical shifts of trace impurities: common laboratory solvents, organics, and gases in deuterated solvents relevant to the organometallic chemist. *Organometallics* **2010,** *29* (9), 2176-2179.

(2) Takaya, T.; Hamaguchi, H.-o.; Iwata, K., Femtosecond time-resolved absorption anisotropy spectroscopy on 9, 9 ´ -bianthryl: Detection of partial intramolecular charge transfer in polar and nonpolar solvents. *J. Chem. Phys.* **2009,** *130* (1).

(3) Hamm, P.; Zanni, M., *Concepts and methods of 2D infrared spectroscopy*. Cambridge University Press: 2011.

(4) Hochstrasser, R. M., Two-dimensional IR-spectroscopy: polarization anisotropy effects. *Chem. Phys.* **2001,** *266* (2-3), 273-284.

(5) Dymarsky, A. Y.; Kudin, K. N., Computation of the pseudorotation matrix to satisfy the Eckart axis conditions. *J. Chem. Phys.* **2005,** *122* (12).

(6) Coutsias, E. A.; Seok, C.; Dill, K. A., Using quaternions to calculate RMSD. *J. Comput. Chem.* **2004,** *25* (15), 1849-1857.

(7) Kudin, K. N.; Dymarsky, A. Y., Eckart axis conditions and the minimization of the root-mean-square deviation: Two closely related problems. *J. Chem. Phys.* **2005,** *122* (22).

(8) Neese, F., Software update: The ORCA program system—Version 5.0. *WIREs Comput. Mol. Sci.* **2022,** *12* (5), e1606.